A single-nucleus transcriptomic atlas of the adult *Aedes aegypti* mosquito

Olivia V. Goldman[1,2,†,*], Alexandra E. DeFoe[1,3], Yanyan Qi[4,5], Yaoyu Jiao[6], Shih-Che Weng[7,#], Leah Houri-Zeevi[1,3], Priyanka Lakhiani[1], Takeshi Morita[1,3], Jacopo Razzauti[1,8], Adriana Rosas-Villegas[1], Yael N. Tsitohay[1], Madison M. Walker[1,3], Ben R. Hopkins[9], ***Aedes aegypti* Mosquito Cell Atlas Consortium**[^], Omar S. Akbari[7], Laura B. Duvall[10], Helen White-Cooper[11], Trevor R. Sorrells[6,12,13], Roshan Sharma[14,15], Hongjie Li[4,5,*], Leslie B. Vosshall[1,2,3,*], Nadav Shai[1,3,29*]

[1]Laboratory of Neurogenetics and Behavior, The Rockefeller University, New York, NY 10065, USA
[2]Kavli Neural Systems Institute, New York, NY 10065, USA
[3]Howard Hughes Medical Institute, New York, NY 10065, USA
[4]Huffington Center on Aging, Baylor College of Medicine, Houston, TX 77030, USA
[5]Department of Molecular and Human Genetics, Baylor College of Medicine, Houston, TX 77030, USA
[6]Department of Genetics, Yale School of Medicine, New Haven, CT 06510, USA
[7]School of Biological Sciences, Department of Cell and Developmental Biology, University of California, San Diego, La Jolla, CA 92093, USA
[8]Price Family Center for the Social Brain, The Rockefeller University, New York, NY 10065, USA
[9]Department of Evolution and Ecology, University of California Davis, Davis, CA 95616, USA
[10]Department of Biological Sciences, Columbia University, New York, NY 10027, USA
[11]School of Biosciences, Cardiff University, Museum Avenue, Cardiff, CF10 3AT, UK
[12]Wu Tsai Institute, Yale University, New Haven, CT 06510, USA
[13]Howard Hughes Medical Institute, New Haven, CT 06510, USA
[14]Program for Computational and Systems Biology, Sloan Kettering Institute, Memorial Sloan Kettering Cancer Center, New York, NY 10065, USA
[15]Single-cell Analytics Innovation Lab, Sloan Kettering Institute, Memorial Sloan Kettering Cancer Center, New York, NY 10065, USA

[†]Present address: Department of Molecular and Cell Biology, University of California, Berkeley, Berkeley, CA 94720, USA
[#]Present address: Department of Tropical Medicine and Parasitology, College of Medicine, National Taiwan University, Taipei, Taiwan

*Correspondence: ogoldman2@gmail.com (O.V.G.), Hongjie.Li@bcm.edu (H.L.), leslie@rockefeller.edu (L.B.V.), nshai@rockefeller.edu (N.S.).

Key words: *Aedes aegypti*; mosquito; snRNA-seq; cell atlas; sexual dimorphism

^*Aedes aegypti* Mosquito Cell Atlas Consortium (in alphabetical order): Joshua X. D. Ang[16], Igor Antoshechkin[17], Yu Cai[18,19], Fangying Chen[7], Yen-Chung Chen[20], Julien Devilliers[21], Linhan Dong[10], Roberto Feuda[21], Paolo Gabrieli[22], Artyom Kopp[9], Hyeogsun Kwon[23], Hsing-Han Li[7], Tzu-Chiao Lu[4,5], Thalita Lucio[24,25], João T. Marques[26], Marcus F. Oliveira[24,25], Roenick P. Olmo[26], Umberto Palatini[1,+], Zeaan M. Pithawala[27], Julien Pompon[28], Yan Reis[24,25], João Rodrigues[24,25], Ryan C. Smith[23]

[16]The Department of Biology, University of York, Wentworth Way, York, YO10 5DD, UK
[17]Division of Biology and Biological Engineering (BBE), California Institute of Technology, Pasadena, CA 91125, USA
[18]Temasek Life Sciences Laboratory, 1 Research Link, National University of Singapore, Singapore 117604
[19]Department of Biological Sciences, National University of Singapore, Singapore 117543
[20]Department of Biology, New York University, New York, NY 10003, USA
[21]Department of Genetics, Genomics and Cancer Sciences, University of Leicester, Leicester, LE1 7RH, UK
[22]Department of Biosciences, University of Milan, Milan, 20133, Italy
[23]Department of Plant Pathology, Entomology and Microbiology, Iowa State University, Ames, IA 50011, USA
[24]Institute of Medical Biochemistry Leopoldo de Meis, Universidade Federal do Rio de Janeiro, Rio de Janeiro, RJ, CEP 21941-590, Brazil
[25]Instituto Nacional de Ciência e Tecnologia em Entomologia Molecular (INCT-EM), Rio de Janeiro, Brazil
[26]Inserm U1257, CNRS UPR9022, Université de Strasbourg, 67084 Strasbourg, France
[27]Department of Epidemiology of Microbial Diseases, Yale School of Public Health, New Haven, CT 06510, USA
[28]MIVEGEC, Univ. Montpellier, IRD, CNRS, INRAe, Montpellier, France

[+]Present address: Department of Biology and Biotechnology, University of Pavia, Pavia 27100, Italy
[29]Lead contact

Summary

The female mosquito's remarkable ability to hunt humans and transmit pathogens relies on her unique biology. Here, we present the *Aedes aegypti* Mosquito Cell Atlas, a comprehensive single-nucleus RNA sequencing dataset of more than 367,000 nuclei from 19 dissected tissues of adult female and male *Aedes aegypti*, providing cellular-level resolution of mosquito biology. We identify novel cell types and expand our understanding of sensory neuron organization of chemoreceptors to all sensory tissues. Our analysis uncovers male-specific cells and sexually dimorphic gene expression in the antenna and brain. In female mosquitoes, we find that glial cells in the brain, rather

than neurons, undergo the most extensive transcriptional changes following blood feeding. Our findings provide insights into the cellular basis of mosquito behavior and sexual dimorphism. The *Aedes aegypti* Mosquito Cell Atlas aims to serve as a resource for the vector biology community, enabling systematic investigation of cell type-specific expression across all mosquito tissues.

Introduction

Mosquito-borne diseases affect hundreds of millions of people worldwide, with infection rates rising globally each year[1,2]. Furthermore, climate change-driven habitat expansion is predicted to put nearly 50% of the global population at risk for viral infection from *Aedes* mosquitoes by 2050[3]. *Aedes aegypti* is the primary vector for mosquito-borne viruses, including dengue, Zika, yellow fever, and chikungunya[4,5]. The most effective way to control mosquito-borne diseases remains the management of vector mosquito populations. However, despite advances in insecticidal and genetic control strategies[6], adaptations of both mosquitoes and pathogens can render interventions less effective. There is a need for deeper insights into mosquito cellular and molecular biology to innovate methods of mitigating the spread of mosquito-borne disease.

The profound sexual dimorphism of *Aedes aegypti* mosquitoes is fundamental to the public health threat they pose to humans. Mosquitoes are attracted to human cues, including exhaled carbon dioxide (CO_2), body heat, and skin odor[7–10]. Only females feed on blood, which provides the proteins and other nutrients that they require for reproduction. Humans are the preferred host for female *Aedes aegypti*, contributing to their effectiveness as a disease vector[11,12]. After consuming a blood meal, females undergo physiological and behavioral changes, including suppressed host seeking and generally reduced activity for 48-72 hours while they develop their eggs and find a suitable oviposition site guided by sensory attraction to freshwater[13–17]. While female mosquitoes have evolved specialized behavioral and reproductive mechanisms for host seeking, blood feeding, finding freshwater for egg laying, and egg development, males have a simpler behavioral repertoire focused on nectar feeding and mating.

Single-cell RNA sequencing (scRNA-seq) and atlasing have been instrumental in defining the molecular identity of known cell types and discovering new cell types. Cell atlases have been constructed for several whole organisms, including the roundworm *Caenorhabditis elegans*[18,19], the planarian *Schmidtea mediterranea*[20], the house mouse *Mus musculus*[21,22], the gray mouse lemur *Microcebus murinus*[23], and others. The Fly Cell Atlas represents a whole-organism cell atlas for *Drosophila melanogaster*[24] and it has been an important resource for understanding insect cell types and gene expression patterns.

Prior studies have used bulk RNA sequencing (RNA-seq) to profile diverse *Aedes aegypti* tissues[25–31]. Recently, scRNA-seq and single-nucleus RNA sequencing (snRNA-seq) have been used on various mosquito tissues. In *Aedes aegypti*, these studies have profiled the gut[32–35], olfactory organs[36,37], brain[38], fat body[35], and larval ventral nerve cord[39]. In *Anopheles gambiae*, single-cell approaches have been used to

study testes[40,41] and the immune system[42,43]. The *Culex tarsalis* gut has also been examined[44]. Additional immune system studies have compared hemocytes across both *Anopheles gambiae* and *Aedes aegypti*[42]. The major mosquito vector genera for human disease (*Aedes, Anopheles*, and *Culex*) diverged approximately 110-180 million years ago[45], representing substantial evolutionary distance important for interpreting comparisons of cellular and molecular findings across species.

While these studies have provided valuable insights into mosquito biology across species, most mosquito single-cell studies to date have focused on specific tissues or cell types, primarily in females. A global gene expression map with a larger number of tissues, spanning both sexes within a single species is needed to allow comprehensive investigation and produce unique insights into *Aedes aegypti* biology[24,46].

We sought to gain system-level insights into the molecular and cellular differences underlying the extraordinary sexual dimorphism of this species. To achieve this, we developed the *Aedes aegypti* Mosquito Cell Atlas, a large-scale snRNA-seq project characterizing every major tissue from the adult female and male *Aedes aegypti* mosquito. To construct this atlas, we profiled 367,096 nuclei from 19 tissues, providing cellular resolution of the entire mosquito transcriptome. For the female brain, we include multiple timepoints before and after blood feeding, associated with distinct phases of egg development and post-blood-feeding behavioral changes, to discover transcriptional changes correlated with behavioral shifts linked to reproductive state. We found specialized gene expression patterns and identified antimicrobial peptide-expressing cells in the female salivary glands. In the antennae, we discovered male-specific *ppk317*-expressing cells and sexually dimorphic olfactory sensory neurons. We observe that mosquito legs and proboscis house polymodal sensory neurons that co-express receptors for different sensory modalities and, similar to other sensory appendages, across gene families, as shown in the antenna in previous studies[36,37]. In the brain, we identified sexually dimorphic gene expression in Kenyon cells and extensive transcriptional changes in glial cells following blood feeding.

This atlas represents a valuable resource for the vector biology community, bridging the gap between model organism studies and mosquito-specific biology. We hope that the *Aedes aegypti* Mosquito Cell Atlas will spur interest from scientists working in other species who wish to gain comparative insights into its unique biology. While a century of work with *Drosophila melanogaster* flies has provided foundational knowledge of insects, creating the tools and datasets directly related to mosquitoes allows us to move away from homology-based research that seeks to align mosquito and fly biology. More broadly, these data offer new avenues for studying the molecular biology underlying the specific adaptations and specializations that make mosquitoes such effective and deadly pathogen vectors.

Results

snRNA-seq mapping of the entire adult female and male *Aedes aegypti* mosquito
Tissues for the *Aedes aegypti* Mosquito Cell Atlas were selected based on biological importance and dissection feasibility with the aim of mapping all female and male cell types from sugar-fed, aged-matched animals. In addition, we collected female brains at various times following a blood meal to profile gene expression changes across the reproductive cycle. Our approach used physical dissection to obtain tissue for snRNA-seq, rather than generating genetically-labeled strains and isolating cells by fluorescent marker expression. This somewhat limited our ability to finely subdivide the mosquito into the largest number of individual tissues and organs. For example, we did not obtain separate data from tissues such as the heart, male salivary gland, or hemocytes. This is a common limitation in dissection-based whole animal single-cell atlases. Collecting major body segments – head including head appendages, thorax including legs but not wings, and abdomen – allowed verification of gene expression signatures for individual tissues and data collection from cells and tissues not separately dissected. We chose 19 tissues related to five broad categories of mosquito biology: (I) major body segments, (II) sensation and host seeking, (III) viral infection, (IV) reproduction, and (V) central nervous system (Figure 1A). Because isolating intact cells from cuticular tissues such as antennae and maxillary palps is challenging in both mosquitoes and flies[24,36], we chose snRNA-seq rather than scRNA-seq to standardize data collection across all tissues[47] and for its demonstrated consistency representing *in vivo* compositions of cell types[48].

Female mosquito egg development requires a blood meal. Blood-fed animals suppress their host seeking and biting behavior for several days after the blood meal until the eggs are laid[13–17]. Previous mosquito RNA-seq studies identified hundreds of gene expression changes associated with blood feeding in many tissues, including the brain[26,28,49–52]. To assess how transcripts in the brain change after a blood meal with single-cell resolution, we sequenced female brains obtained from animals 3, 12, 24, and 48 hours post-blood feeding (Figure 1A). We selected these timepoints to represent the various stages of egg maturation and suppression of attraction to humans.

We dissected 44 samples, including 17 sugar-fed female tissues, 15 sugar-fed male tissues, and 4 samples of brains from blood-fed females at the timepoints indicated above. Male and female animals were co-housed prior to dissection and females were presumably mated. Sugar-fed females were never blood-fed. Nuclei were extracted and collected using fluorescence-activated cell sorting (FACS), and single-nucleus transcriptomes were generated using 10x Genomics technology and Illumina sequencing unless otherwise stated (Figure 1B). Because data collection methods were identical, we included snRNA-seq data from female antenna and maxillary palp samples previously published in Herre, Goldman et al.[36] and re-analyzed them in parallel with the data collected in this manuscript. Data from all samples were aligned to the *Aedes aegypti* L5 genome[53] and individually assessed for quality control and filtered appropriately (Figure S1). We retained a total of 367,096 nuclei comprising 197,607

sugar-fed female nuclei, 138,760 sugar-fed male nuclei, and 30,729 blood-fed female nuclei from a total of 9,651 mosquitoes. These nuclei were captured across 47 samples (10x Genomics libraries), 44 dissected for this study and 3 samples from our previous study[36] (Figure 1B and Table S1). Across all nuclei from all tissues, average mitochondrial gene percentage was 0.13%, median total UMI per nucleus was 3,424, and median genes per nucleus was 1,296 (Figure S2). We combined male and female data of the same tissue to compare cell composition and gene expression between the sexes (Table S2). We then combined the data from all male and female sugar-fed tissues to create a complete mosquito cell atlas (Figures 1C-1D).

The hallmark of a cell atlas is the ability to annotate distinct cell types. In non-model organisms, the lack of knowledge of expected cell types or established gene markers makes annotation challenging. We developed two complementary strategies to address these challenges. First, we relied on experts in mosquito biology and entomology to annotate data using published work and previously validated *Aedes aegypti* gene markers wherever possible. Second, we took an unbiased approach and computationally identified gene markers using standard differential gene expression tools in scRNA-seq data analysis[54,55]. In cases when marker genes were not characterized, we relied on orthology information from genes studied in *Drosophila melanogaster*, assessed using Ensembl Metazoa BioMart database[56], BLAST (nucleotide or protein)[57], or VectorBase[58]. Many of our annotations use marker genes that may imply function based on *Drosophila melanogaster* literature (list of gene identifiers and ortholog names used can be found in Table S3). *Aedes aegypti* and *Drosophila melanogaster* are separated by 260 million years of evolution[59–61], with distinct behaviors, life cycles, and physiology. Relying on *Drosophila melanogaster* homology to interpret *Aedes aegypti* genes can be problematic. We caution that in most cases, the orthologous gene function between *Drosophila melanogaster* and *Aedes aegypti* has not been confirmed. For annotation of cell types, we sought to use multiple orthologous genes and/or genes predicted to encode a protein directly related to the function of the cells. However, to avoid mischaracterizing a cell type, we often used gene names to annotate cell types in our data. This was done to avoid the pitfall of presuming *Drosophila melanogaster* cell type orthology from gene orthology.

We first annotated tissues individually, which offered a higher resolution of cell types (Figures 2, 3, 7, S3-S13, S18, and S21-S22, see Table S4 and Zenodo Supplemental Data for gene thresholds and scripts used for annotation). To understand the global relationship of the tissue cell types, we integrated data across sexes and dissected tissues (Figures 1E and 1D). Cells from tissues across samples merged as expected (e.g., follicular cells identified from female abdomen and female ovary samples merged) (Figures S2D-S2F). Using combinations of marker genes, we discerned 66 distinct cell types ("Level 2" annotations) (Figures 1F and S3C) and assigned them to one of 14 major cell type categories ("Level 1" annotations) (Figures 1E, S3B, and S3C). Examples of marker genes expressed in major cell types include *Syt1* (*AAEL000704*) in neurons, *repo* (*AAEL027131*) in glia, *FAS1* (*AAEL001194*) in fat tissue, *FAS2* (*AAEL008160*) in oenocytes, *titin* (*AAEL002565*) for muscle, *Ppn* (*AAEL019468*) for hemocytes, *nub* (*AAEL017445*) for enterocytes, and *Delta* (*AAEL025606*) for

enteroblasts/intestinal stem cells. *grh* and *snu* serve as gene markers for epithelial-like cells. *grh* is an orthologue of a *Drosophila melanogaster* transcription factor that is not exclusive to epithelial cells, but serves as an epithelial cell marker[24,62,63]. Similarly, *Drosophila melanogaster snu* encodes an ABC transporter involved in cuticle development[64] and also serves as a non-exclusive epithelial cell marker[65]. In the absence of functional validation that *snu* and *grh* are epithelial markers in *Aedes aegypti*, we took a cautious approach and retained the gene names for annotations rather than assigning definitive epithelial cell type labels. Reproductive tissues and salivary glands cell types were recognizable due to being primarily composed of cells of those specific tissue dissections, and as expected also contained representative cells from abdomen and thorax dissections, respectively (Figures 1D). To facilitate community use of processed data and annotations, these have been made available on the UCSC Cell Browser[66] (http://mosquito.cells.ucsc.edu).

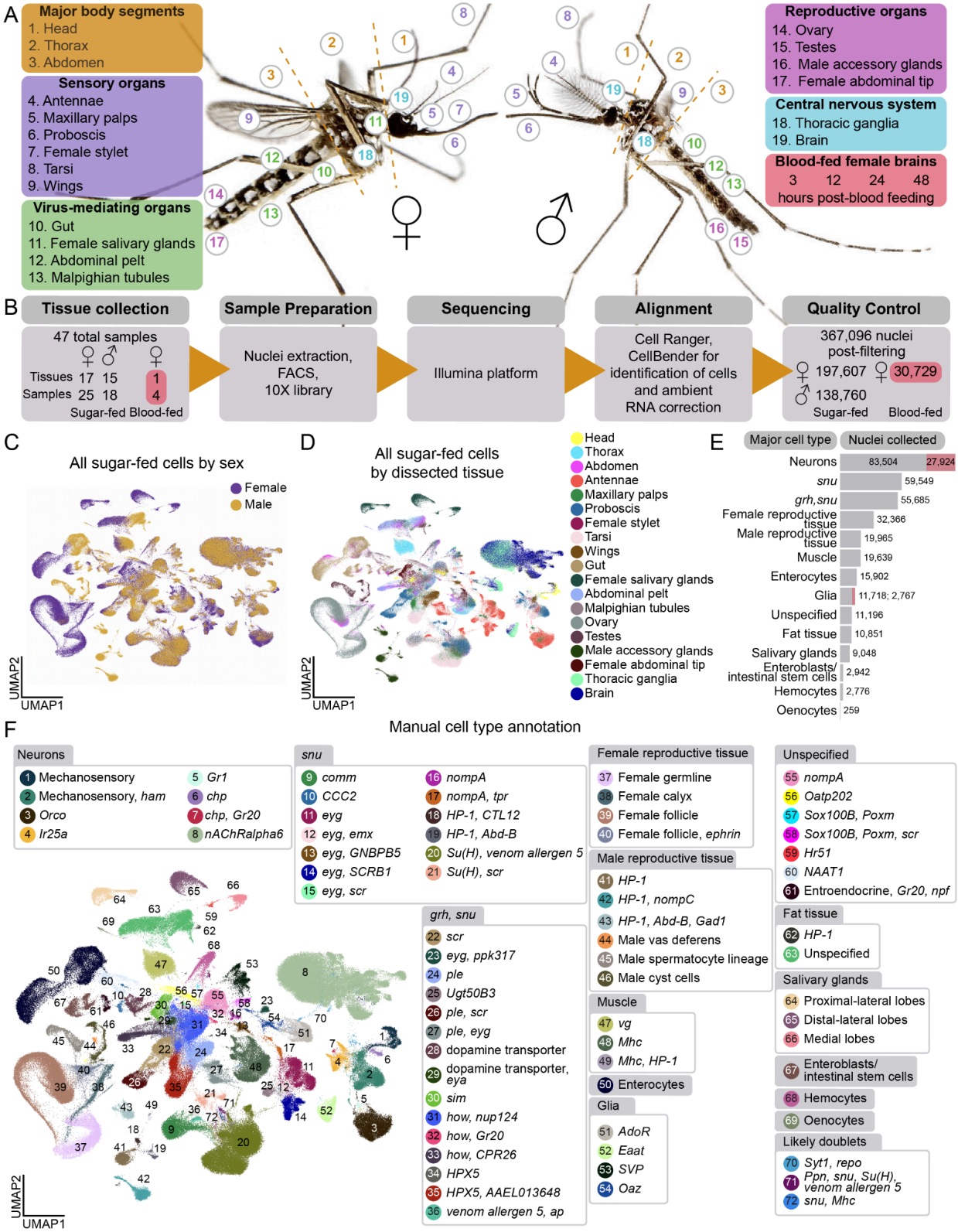
A
Major body segments
1. Head
2. Thorax
3. Abdomen
Sensory organs
4. Antennae
5. Maxillary palps
6. Proboscis
7. Female stylet
8. Tarsi
9. Wings
Virus-mediating organs
10. Gut
11. Female salivary glands
12. Abdominal pelt
13. Malpighian tubules
Reproductive organs
14. Ovary
15. Testes
16. Male accessory glands
17. Female abdominal tip
Central nervous system
18. Thoracic ganglia
19. Brain
Blood-fed female brains
3 12 24 48
hours post-blood feeding
B
Tissue collection
47 total samples
Tissues 17 15 1
Samples 25 18 4
Sugar-fed Blood-fed
Sample Preparation
Nuclei extraction, FACS, 10X library
Sequencing
Illumina platform
Alignment
Cell Ranger, CellBender for identification of cells and ambient RNA correction
Quality Control
367,096 nuclei post-filtering
197,607 30,729
138,760
Sugar-fed Blood-fed
C
All sugar-fed cells by sex
Female
Male
UMAP2
UMAP1
D
All sugar-fed cells by dissected tissue
Head
Thorax
Abdomen
Antennae
Maxillary palps
Proboscis
Female stylet
Tarsi
Wings
Gut
Female salivary glands
Abdominal pelt
Malpighian tubules
Ovary
Testes
Male accessory glands
Female abdominal tip
Thoracic ganglia
Brain
UMAP2
UMAP1
E
Major cell type
Nuclei collected
Neurons 83,504 27,924
snu 59,549
grh,snu 55,685
Female reproductive tissue 32,366
Male reproductive tissue 19,965
Muscle 19,639
Enterocytes 15,902
Glia 11,718; 2,767
Unspecified 11,196
Fat tissue 10,851
Salivary glands 9,048
Enteroblasts/ intestinal stem cells 2,942
Hemocytes 2,776
Oenocytes 259
F
Manual cell type annotation
Neurons
1 Mechanosensory
2 Mechanosensory, ham
3 Orco
4 Ir25a
5 Gr1
6 chp
7 chp, Gr20
8 nAChRalpha6
snu
9 comm
10 CCC2
11 eyg
12 eyg, emx
13 eyg, GNBPB5
14 eyg, SCRB1
15 eyg, scr
16 nompA
17 nompA, tpr
18 HP-1, CTL12
19 HP-1, Abd-B
20 Su(H), venom allergen 5
21 Su(H), scr
grh, snu
22 scr
23 eyg, ppk317
24 ple
25 Ugt50B3
26 ple, scr
27 ple, eyg
28 dopamine transporter
29 dopamine transporter, eya
30 sim
31 how, nup124
32 how, Gr20
33 how, CPR26
34 HPX5
35 HPX5, AAEL013648
36 venom allergen 5, ap
Female reproductive tissue
37 Female germline
38 Female calyx
39 Female follicle
40 Female follicle, ephrin
Male reproductive tissue
41 HP-1
42 HP-1, nompC
43 HP-1, Abd-B, Gad1
44 Male vas deferens
45 Male spermatocyte lineage
46 Male cyst cells
Muscle
47 vg
48 Mhc
49 Mhc, HP-1
50 Enterocytes
Glia
51 AdoR
52 Eaat
53 SVP
54 Oaz
Unspecified
55 nompA
56 Oatp202
57 Sox100B, Poxm
58 Sox100B, Poxm, scr
59 Hr51
60 NAAT1
61 Entroendocrine, Gr20, npf
Fat tissue
62 HP-1
63 Unspecified
Salivary glands
64 Proximal-lateral lobes
65 Distal-lateral lobes
66 Medial lobes
67 Enteroblasts/ intestinal stem cells
68 Hemocytes
69 Oenocytes
Likely doublets
70 Syt1, repo
71 Ppn, snu, Su(H), venom allergen 5
72 snu, Mhc
UMAP2
UMAP1

Figure 1. *Aedes aegypti* Mosquito Cell Atlas tissues and data.
(A) Photos of *Aedes aegypti* female (left) and male (right). Numbers indicate location of collected tissues (listed in legend boxes). Photos by Alex Wild.
(B) Schematic of *Aedes aegypti* Mosquito Cell Atlas workflow. A total of 47 samples were processed, representing 17 distinct female tissues and 15 distinct male tissues from *Aedes aegypti* mosquitoes. A sample represents an individual library prepared with 10x Genomics commercial kits. Sample counts shown for each sex. A total of 9,651 animals were used in this study. Tissues underwent nuclei extraction followed by fluorescence-activated cell sorting (FACS), single-nucleus RNA libraries preparation with 10x Genomics commercial kits, then sequenced using the Illumina platform unless stated otherwise. Raw sequencing data was aligned with Cell Ranger[67]. Cells were identified and ambient RNA removed using CellBender[68]. Samples were individually processed for cell quality control filtering, yielding 367,096 high-quality nuclei (nuclei counts shown for each sex and for blood feeding conditions).
(C-D) Uniform manifold approximation and projection (UMAP) for dimension reduction of 330,364 nuclei from all mated, sugar-fed tissues from both sexes colored by sex (C) and colored by dissected tissue (D). Nuclei from blood-fed mosquitoes not included. For batch processing consistency with all other samples, testes sample underwent ambient RNA removal and cell identification with CellBender (and is missing spermatids).
(E) Number of mated, sugar-fed nuclei (grey) and mated, blood-fed nuclei (red) collected across all samples for each major cell type, sorted by abundance.
(F) UMAP of nuclei from all mated, sugar-fed tissues, colored and numbered by manual annotation of 66 distinct cell types ("Level 2") as listed in legend at the right of the figure panel. Major cell type categories ("Level 1" annotations) are represented by shaded grey headers and depicted in Figure S3B. For a complete look up table of gene symbols to gene IDs used in this manuscript, see Table S3. For annotation thresholds see Table S4.

Annotation of male testes and identification of spermatids

To validate the quality of our snRNA-seq data and our annotation approach, we first turned to the male testes. Mosquito testes have been studied extensively as a potential target for mosquito population control and that has well-characterized cell types and marker genes. We dissected testes from 212 male mosquitoes for a total of 12,074 nuclei after quality-control filtering (Figure 2A). Following pre-processing, we identified 14 distinct cell types (Figure 2B, see Table S4 and Zenodo Supplemental Data for gene thresholds and scripts used for annotation).

We first identified the germline lineage based on the expression, in early stages, of *vas* (*AAEL004978*), which is homologous to the *Drosophila melanogaster* germline marker and known for its conserved role in germ cell development across species[69] (Figure 2B), and expression of *beta2-tubulin* (*AAEL019894*) in spermatocytes. Initially, spermatids were absent from our analysis, due to their characteristically low transcriptional activity[24,70,71] (Figure S14A-S14D). After modifying our filtering criteria, we identified a distinct spermatid cluster characterized by the presence of *S-Lap* (*AAEL000108*), *DBF4* (*AAEL008779*)[72], and *Orco* (*AAEL005776*)[73] (Figures 2B and S14E-S14G). Similarly, we observed clusters representative of the various stages of cyst cell development including early to late cyst cells, as well as the testes epithelium (Figure 2B). We also observed the expression of the taste receptor *Gr39* during the cyst cell developmental trajectory, underscoring the largely uncharacterized presence of chemoreceptors in non-sensory tissues in *Aedes aegypti* and other insects (Figure S14H)[74–78].

Next, we used RNA fluorescence *in situ* hybridization to correlate mRNA expression patterns in testes with our snRNA-seq data. Consistent with our snRNA-seq, *vas* (*AAEL004978*) RNA *in situ* hybridization showed expression in early germline cells, from germline stem cells to early spermatocytes (Figure 2C). The expression of testis-specific *beta2-tubulin* (*AAEL019894*) was mainly detected in primary spermatocytes (Figure 2D), consistent with a previous study in *Aedes aegypti*[79]. Weaker *beta2-tubulin* RNA *in situ* hybridization signal can be seen in spermatids, as the transcripts remain in the cytoplasm of early elongation spermatids before being degraded as the spermatids mature[80].

eya is a well-characterized cyst cell marker in *Drosophila melanogaster*[81]. According to our snRNA-seq data, the *Aedes aegypti* homolog of *eya (AAEL019952)* is also expressed in cyst cells, particularly at the mid-stages of spermatogenesis (Figure 2E). RNA *in situ* hybridization of *eya (AAEL019952)* confirms this localization. We also observed regional differences in the testicular epithelium. *ana* (*AAEL007208*) was detected in the testes epithelium, particularly towards the posterior of the testis, and in late cyst cells (Figure 2F). *AAEL001918* was also detected in the terminal epithelium and was enriched in the most posterior region (Figure 2G). These findings are consistent with the snRNA-seq data and also suggest the existence of a transcriptomically-distinct terminal subpopulation of the testes epithelium.

Coordinated results between our RNA *in situ* hybridization experiments and snRNA-seq data supported our cell annotation approach, which we then applied to all other tissues in this project.

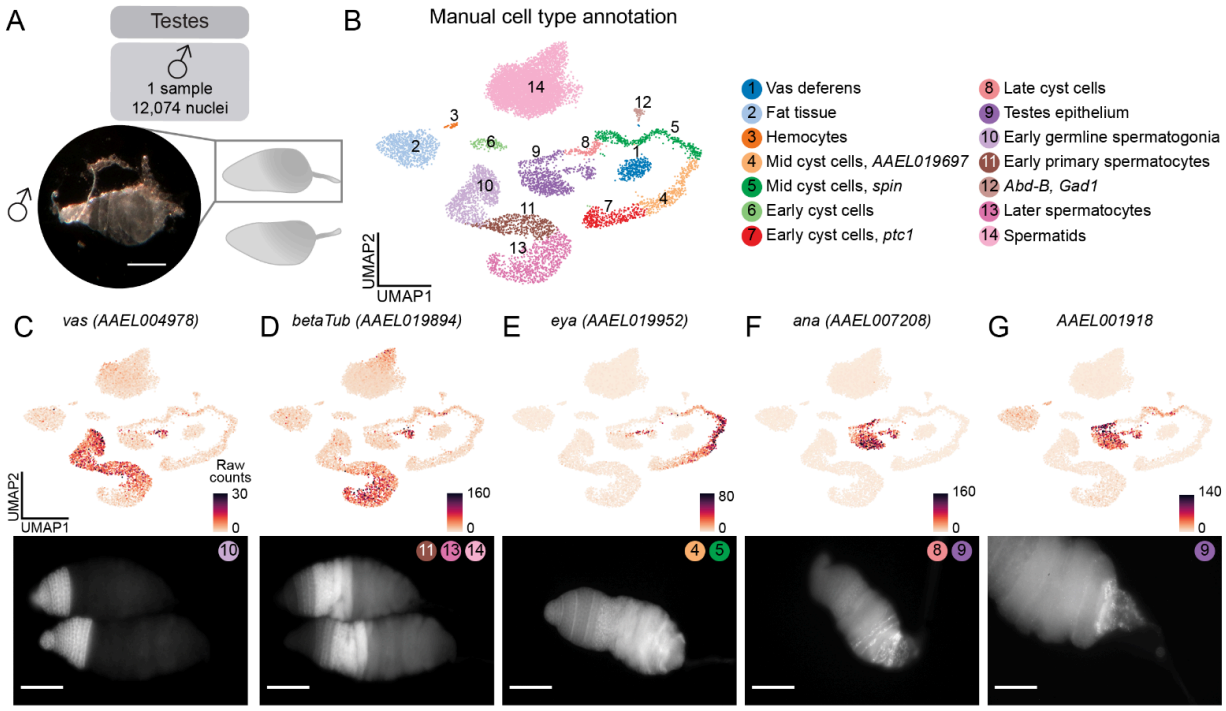

Figure 2. Localization and validation of testes RNA transcripts.
(A) Representative photo of a mated, sugar-fed testis dissection with anatomical diagram of testes pair. One sample (10x Genomics library) yielded 12,074 nuclei from 212 animals, post-quality control filtering. Scale bar: 500 µm.
(B) UMAP of mated, sugar-fed testes nuclei, colored and numbered by manual cell type annotation as listed in legend at the right of the figure panel. For a complete look up table of gene symbols to gene IDs used in this manuscript, see Table S3. For annotation thresholds see Table S4.
(C-G) UMAP of raw counts of unique molecular identifiers (UMI) of a subset of genes used to annotate testes data (normalized gene expression are shown in Figures S14I-S14M), as well as corresponding validation using RNA *in situ* hybridization with probes against the indicated genes (below). Genes include *vas* (*AAEL004978*) (C), *betaTub* (*AAEL019894*) (D), *eya (AAEL019952*) (E), *ana (AAEL007208)* (F), and *AAEL001918* (G). Raw counts shown to correlate expression patterns to *in situ* images due to known total count differences in cell types. Corresponding cell type(s) (number and color from B) are shown at top right of each RNA *in situ* hybridization image. Scale bar: 100 µm for C-F; 50 µm for G.

Enhanced spatial mapping of infection-related genes

Mosquito salivary glands are critical for pathogen transmission because female mosquitoes inject saliva beneath the skin during blood feeding. Secretory salivary components influence the host immune response and reduce pain sensitivity to allow the mosquito to feed to repletion before being detected by the host[82–85]. These same salivary components also facilitate pathogen transmission[85–97]. The paired salivary glands are divided into three lobes, with the proximal-lateral and distal-lateral lobes

flanking one medial lobe (Figure 3A). A basal lamina surrounds each lobe, and a single layer of epithelial or saliva-secretory cells (acinar cells) is found within the lamina. These cells are arranged around a central salivary duct that has an apical cavity for saliva storage[98–100].

We dissected the paired salivary glands from 495 female mosquitoes and obtained data from 10,898 nuclei after quality-control filtering (Figure 3A). Recent single-cell transcriptomics, proteomics, and genomics studies have profiled salivary glands from blood-feeding insects leading to a comprehensive list of salivary gland marker genes[86,101–108], which we used to manually annotate the salivary gland tissue cell types in our data (Table S4, Zenodo Supplemental Data). All known salivary gland lobes and expected cell types were recovered in our dataset (Figure 3B).

Previous work has used RNA *in situ* hybridization and immunofluorescence to localize expression of a number of salivary proteins to specific subsets of cells[100,109–111]. We found that a majority of genes related to saliva proteins localized to the three lobes (Figure 3D). We cross-referenced these to published *in situ* hybridization data[100], validating our annotations, and demonstrating our ability to effectively classify the saliva-secretory cells within each of the three major saliva-producing regions. Next, we used our data to identify the putative localization of all secreted proteins identified by mass spectrometry from previous studies of *Aedes aegypti* salivary glands[101,112,113] (Table S4). Using gene expression as a proxy, we successfully assigned the localization of 24 secreted proteins whose cell type and tissue localization was not previously reported (Figure 3D).

Antimicrobial peptide genes are involved in mosquito innate immunity and host response to pathogens[96] and are relevant to mosquito population and disease control. In *Drosophila melanogaster*, fat body cells synthesize antimicrobial peptides for secretion into hemolymph[114]. We found antimicrobial peptide genes, including cecropins (*CECN*) and defensins (*DEFA, DEFC, DEFD*), in the fat tissue collected as part of our dissections of salivary gland and the abdominal pelt, as well as in other cell types throughout the mosquito, including enterocytes and intestinal stem cells (Figures 3C and S15).

Notably, gut enterocytes and fat tissue in the abdominal pelt showed appreciable sexual dimorphism. For gut enterocytes, both *nhe3* and *NAAT1* cell populations exhibited sex-specific expression (for *nhe3* enterocytes, 236 genes significantly upregulated in females, and 103 in males; for *NAAT1*, 65 and 80 for females and males, respectively) (Figures 1C, S9D, S9E, S16A, S16B and Table S13). Similarly, female and male abdominal pelt fat tissue also demonstrated large transcriptional differences (77 genes significantly upregulated in females and 84 in males) (Figures 1C, S10D, S10E, S16C and Table S13).

These comprehensive data provide a better understanding of the expression patterns of salivary-secreted protein genes and antimicrobial peptides. Transcriptomic access to

these critical cells that mediate the spread of disease may stimulate new avenues of investigation into viral transmission and vector effectiveness.

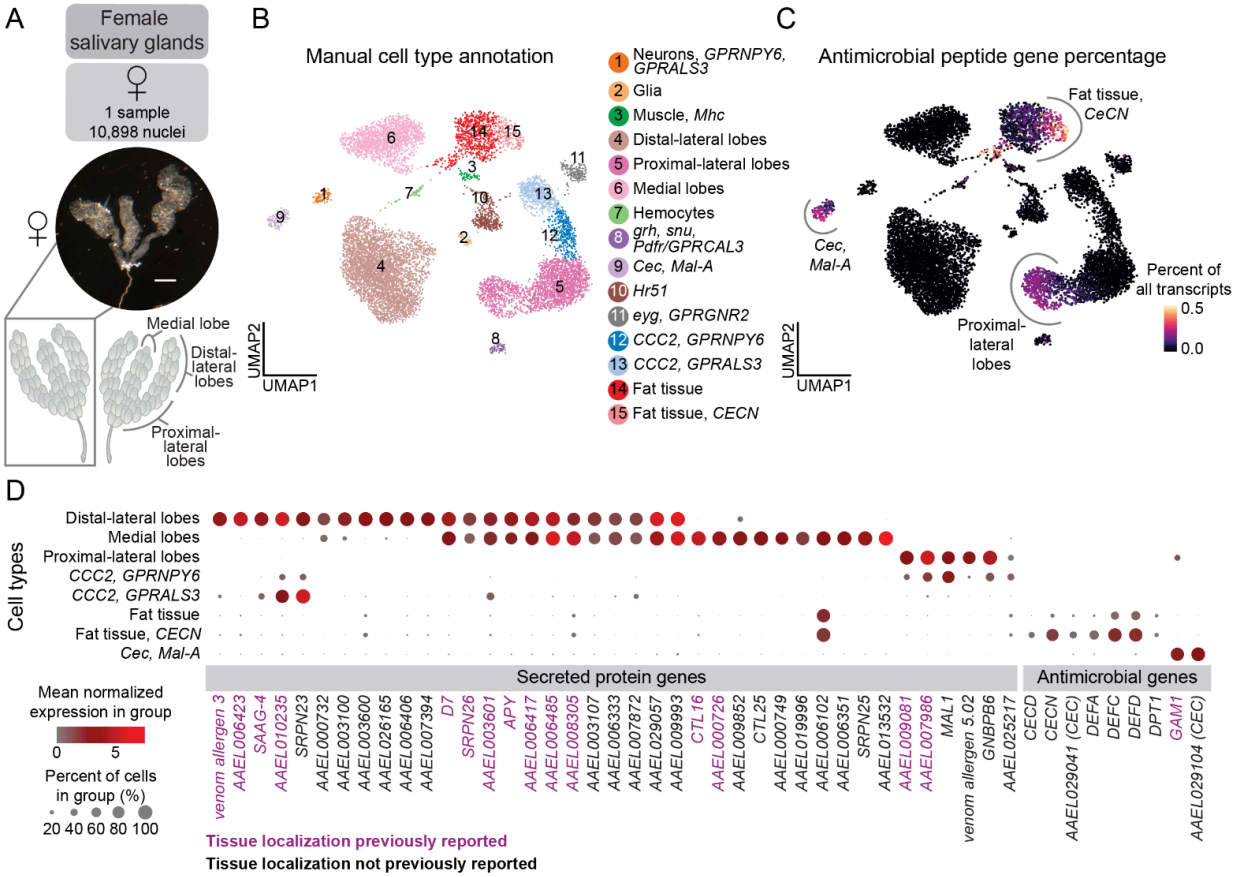

Figure 3. Localization and validation of female salivary gland RNA transcripts.
(A) Representative photo of a mated, sugar-fed female salivary gland dissection with anatomical diagram of salivary gland pair. One sample (10x Genomics library) yielded 10,898 nuclei from 495 animals, post-quality control filtering. Scale bar: 500 µm.
(B) UMAP of female mated, sugar-fed salivary gland nuclei, colored and numbered by manual cell type annotation as listed in legend at the right of the figure panel. For a complete look up table of gene symbols to gene IDs used in this manuscript, see Table S3. For gene annotation thresholds see Table S4.
(C) Female mated, sugar-fed salivary gland UMAP, colored by expression of antimicrobial peptides set: *CECD* (*AAEL029046*), *CECN* (*AAEL029047*), putative cecropins (*AAEL029041* and *AAEL029104*), *DEFA* (*AAEL003841*), *DEFC* (*AAEL003832*), *DEFD* (*AAEL003857*), *DPT1* (*AAEL004833*), *GAM1*(*AAEL004522*). Expression of gene set shown as a fraction of total transcripts in each cell (each end of color bar trimmed 0.1% for visibility). Relevant cell types labeled.
(D) Dot plot illustrating mean normalized expression of salivary gland secreted protein genes and antimicrobial genes by cell type. Localization of genes colored in purple has been validated by previous work[100]. Normalized expression is ln([(raw count/total cell counts)x median total counts across cells]+1). For more information on salivary gland protein genes, see Table S4.

***ppk317* labels a previously unknown male-specific cell type in the antenna**
Female mosquitoes are exquisitely sensitive to the smell of human hosts and use chemosensory neurons in their antennae to detect human body odor[7,115–119]. While the cellular, molecular, and neuronal composition of the female antenna has been extensively investigated[36,37,120–125], the biology of the male antenna is largely unexplored. Although male mosquitoes seek out humans to mate with females[126], it is not known if they are attracted to human odor cues or if they use the same cues as females[127]. *Aedes aegypti* antennae are strikingly sexually dimorphic (Figure 4A), and the cellular and genetic basis of these structural and behavioral dimorphisms is unknown.

To understand differences in cellular composition, we sequenced one male and two female antenna samples and integrated them with our previously published female antenna samples[36] for a total of 24,046 female nuclei and 8,016 male nuclei (Figure 4A-4B). Visualization of the data on a common uniform manifold approximation and projection (UMAP) coordinate revealed shared and sex-specific subpopulations (Figures 4B, S17A, and S17D). While the presence of separated and shared subpopulations between the sexes indicates differences that are likely biological, we cannot rule out complete absence of technical or batch effect given differences in sample processing (Figure S17C). Because batch correction methods aggressively merge the samples, thereby eliminating any biological differences[128], we sought to take a more cautious approach in identifying specific markers or cell types to investigate cellular differences between underlying antenna sexual dimorphism. (Figure S17C-S17D).

We focused on a non-neuronal cluster of male-specific cells marked by *ppk317 (AAEL000873)*, an ion channel of unknown function belonging to the *pickpocket* (PPK) channel (DEG/ENaC) gene family (Figures 4B-4C and S17D)[129–131]. Bulk RNA-seq studies have demonstrated that *ppk317* is exclusively expressed in the male antenna[26] (Figure 4D). Investigating our integrated snRNA-seq dataset of all 330,364 nuclei collected from female and male sugar-fed mosquitoes, showed that *ppk317* is only present in nuclei from the male antenna and head (Figures 4E and S17H-S17I). We find that *ppk317* expression is highly unique to a single male-specific cell type in the antennae.

Male-specific *ppk317* cells are likely epithelial-related, based on their expression of *grh*, an orthologue of a *Drosophila melanogaster* epithelial cell marker[24,62]. To ask to which degree male *ppk317* cells differ from other antenna cell types, we carried out diffusion component analysis, gene-expression correlations, and partition-based graph abstraction to quantify transcriptomic distances between and within cell clusters. We quantitatively demonstrate a strong difference between the male *ppk317* cluster and other cell types, including other *grh*+ and *grh*+*, snu*+ cells (Figures S17E-S17G, S17J, and Zenodo Supplemental Data). *ppk317* cells were also strongly self-correlated based on their gene expression, indicating relative homogeneity within the cell type (Figures S17G and S17J). To confirm that *ppk317* is only expressed in male antennae, we performed RNA *in situ* hybridization on male and female antennae*. ppk317* showed strong and selective expression in the joints of the male antennae (Figures 4F-4H) and

was not detected at all in female antennae (Figures 4I-4K and S18A). The function of this unique male-specific *ppk317* cell type is unknown and requires future investigation.

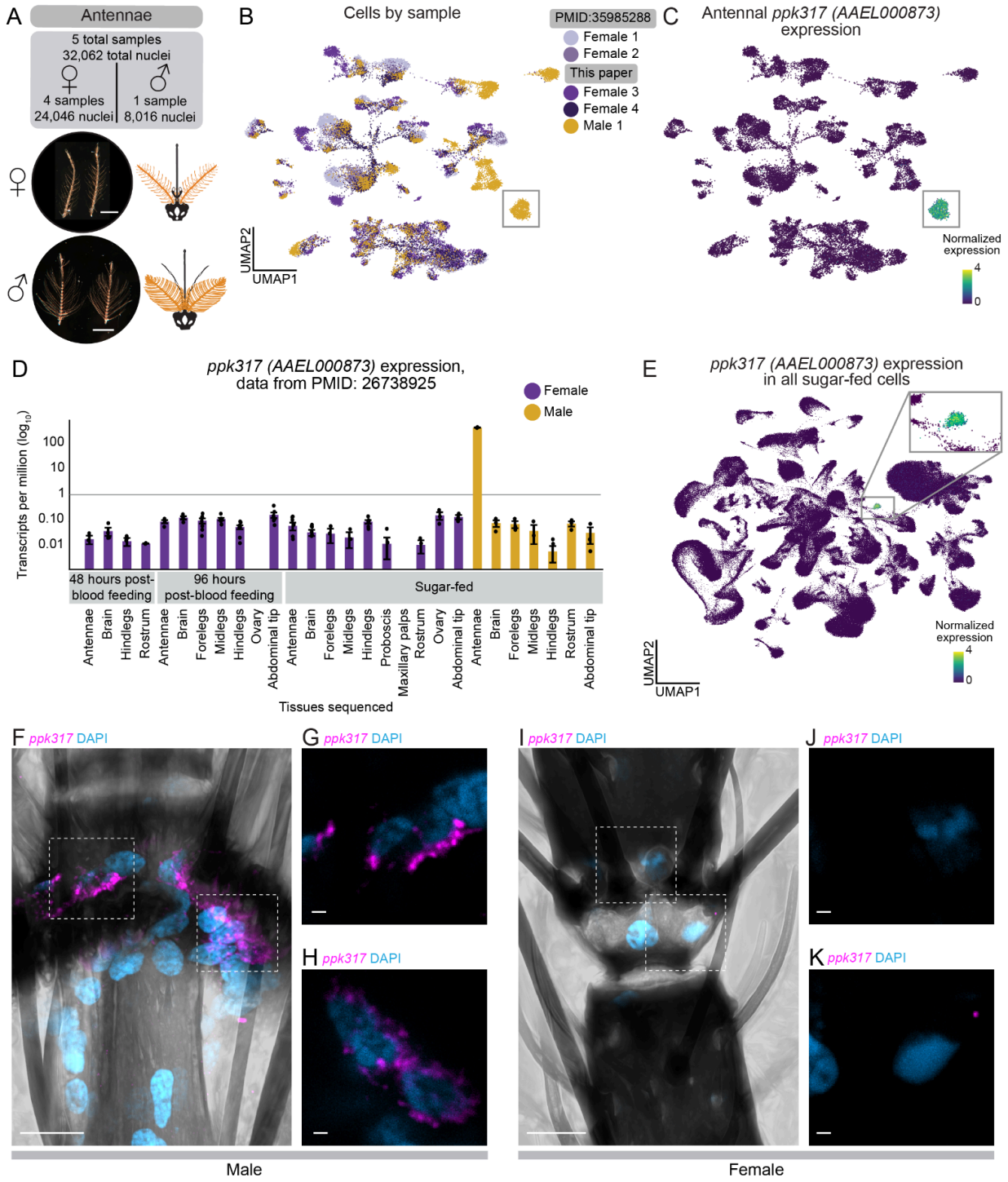

Figure 4. Identification of male-specific *ppk317* cell type in the *Aedes aegypti* antenna. (A) Representative photo of mated, sugar-fed female (top) and male (bottom) antenna dissections with anatomical diagrams (in orange). Five samples (10x Genomics libraries)

yielded 32,062 nuclei from 2100-2700 animals post-quality control filtering. Photo of dissected mated, sugar-fed female (middle) and male (bottom) antenna with anatomical diagram (in orange, bottom-left), and collected sample information (top). Scale bar: 500 µm.
(B) UMAP of mated, sugar-fed antenna nuclei, colored by sample (female samples = 4, male samples = 1). Putative male-specific cluster highlighted in grey box.
(C) UMAP of *ppk317* (*AAEL000873*) gene expression (normalized) in all antenna nuclei. Cluster with high expression highlighted in grey box. Normalized expression is ln([(raw count/total cell counts)x median total counts across cells]+1).
(D) *ppk317 (AAEL000873)* expression [transcripts per million ($\log_{10}$)] in the indicated tissues. Female tissues were 48 and 96 hours post-blood feeding or fed on sugar (purple). Male tissues are sugar-fed (yellow). Both sexes were mated and females were not offered an egg-laying substrate prior to tissue collection. Data from previously published RNA-seq data[26].
(E) UMAP of *ppk317 (AAEL000873)* normalized expression in all mated, sugar-fed nuclei. Cluster with high expression highlighted in grey box, enlarged in inset.
(F) Maximum-intensity projection of whole-mount, mated and sugar-fed male antenna with RNA *in situ* hybridization showing *ppk317* probe (magenta) and nuclear staining (DAPI). Scale bar: 10 µm.
(G-H) Enlarged view of a single Z plane (Z = 0.24 µm) of white highlighted boxes from (F) left box **(G)** and right box (H). Scale bar: 1 µm.
(I) Maximum-intensity projection of whole-mount, mated and sugar-fed female antenna with RNA *in situ* hybridization showing *ppk317* probe (magenta) and nuclear staining (DAPI). Scale bar: 10 µm.
(J-K) Enlarged view of a maximum-intensity projection of white highlighted boxes from (I) left box (J) and right box (K). Scale bar: 1 µm.

A precise sexual dimorphism in a single antennal chemosensory cell type
Understanding the complexity of the mosquito olfactory system is crucial to deciphering how mosquitoes excel at locating human hosts. Insects detect chemosensory cues with heteromultimeric ligand-gated ion channels encoded by three large multigene families, the odorant receptors (ORs), ionotropic receptors (IRs), and gustatory receptors (GRs). These receptors assemble into complexes composed of broadly expressed co-receptors and more selectively expressed ligand-specific subunits. Recent work using snRNA-seq and other methods showed that female *Aedes aegypti* olfactory sensory neurons co-express both co-receptors and ligand specific receptors both within and between major receptor families[36,37]. Using data from our cell atlas, we investigated if the organization of the *Aedes aegypti* male antenna resembles that of females and if receptor co-expression occurs.

We began by isolating neurons among the total population of 32,062 male and female antenna nuclei (Figures 4A-4B) based on expression of *Syt1* (*AAEL000704*), *brp* (*AAEL018153*), *nSyb* (*AAEL024921*) and *CadN* (*AAEL000597*) (Figure 5A). Mechanosensory neurons were 9% of total neurons based on the expression of the *Drosophila melanogaster* orthologue of mechanosensory receptor *nompC* (*AAEL019818*) (Figures S19A-S19B). These were filtered out to focus on non-mechanosensory neurons. After additional quality control filtering steps, we obtained 7,950 *nompC*-negative neurons, comprising 7,003 neurons from females and 947 neurons from males (Figures 5A and S19C-S19I).

We reclustered the *nompC*-negative neurons and manually annotated them using chemoreceptors uniquely expressed within a cell type (Figure 5B). As previously reported[36,37], *Aedes aegypti* olfactory sensory neuron cell types can express multiple ligand-specific chemoreceptors. Some ligand-specific chemoreceptors are also co-expressed in more than one olfactory sensory neuron cell type, as part of different sets of ligand-specific chemoreceptors. Generally, our annotated cell types demonstrated unique combinations of putative transcription factor genes, supporting our annotation's classification of transcriptomically distinct cell types (Figure S20A). The two new female antennal samples replicated our previous finding of co-expression of *Orco* and *Ir25a*[36] (Figures 5C-5D and S19L). Our data also replicate prior findings that female *Ir41l*-expressing olfactory sensory neurons co-express *Orco*, *Ir25a*, and *Ir76b*, along with additional ligand-specific receptors including *Or80, Or81*, *Or82*, and *Ir41m*[36,37] (Figure S19L). We additionally find that *Ir41l* olfactory sensory neurons also express *ppk205* (Figure 5C-5D).

In total, we annotated over 54 olfactory sensory neuron cell types with distinct expression patterns (Figure S20 and Zenodo Supplemental Data). In our annotations, we found at least 6 examples of chemoreceptor genes co-expressed within a cluster but not within the same cells. While this indicates mutual exclusivity of the genes, we cannot rule out the possibility that it could be due to dropouts in single-cell sequencing, particularly because receptor genes can be expressed at relatively low levels, although this is unlikely given the data's large number of cells and high sequencing depth. Furthermore, these cells occupy the same phenotype space and are not discernible as distinct clusters computationally, suggesting that these olfactory sensory cell types may be distinct, but transcriptomically similar (for instance, *Ir41b* and *Ir41*e in Figures 5C-5D, S20B, and Zenodo Supplemental Data). These findings are similar to the ~60 olfactory sensory neuron cell types recently identified in the female antenna in another study[37].

We then investigated the differences between male and female mosquito olfactory sensory neurons. Despite the sexually dimorphic olfactory behaviors displayed by male and female mosquitoes[12,127,132,133], there were limited transcriptional differences between male and female olfactory sensory neurons. This is reflected in our finding that all annotated cell types contained both male and female cells, although in different proportions (Figures S19I-S19J). We then calculated differentially expressed genes between male and female cells within each sensory neuron cell type using MAST[55] (Figure S19M and Table S5). Across the sensory neuron cell types, the ADP/ATP carrier protein *SLC25A5* (*AAEL004855*) was the most frequent differentially-expressed gene between female and male chemosensory cells, followed by a putative Mg^{2+}/Na^{+} transporter (*AAEL009150*), the male-determining factor *Nix* (*AAEL022912*), a putative serine/threonine kinase (*AAEL004217*), and the odorant binding protein *OBP35* (*AAEL002606*) (Table S5). The significance of this sex-specific differential expression is unknown, with the exception of *Nix*, which is required for male sex determination.

Out of 403 putative sensory genes queried, including ORs, IRs, GRs, PPKs, transient receptor potential (TRP) ion channels, opsins, and mechanosensory receptors, only four were significantly differentially expressed between corresponding male and female

sensory neuron cell types: *Or82*, *Ir25a*, *Ir76b*, and *Or2* (Figures S19N-S19Q, Table S5, for full queried gene list see Table S4). Surprised to find so few differentially-expressed sensory genes, we wanted to ensure that our results were not driven by outliers and effects of data normalization. We looked at the raw counts (unique molecular identifiers) of all of the sensory genes in the olfactory sensory neuron population (Figure S20C). We found comparable gene transcript counts for each sample and across sexes, validating that we were not overlooking large differences between male and female sensory gene expression.

Careful analysis of these chemoreceptor expression profiles revealed a precise and unexpected sexual dimorphism in a single population of olfactory sensory neurons. We discovered that while male and female *Ir41l* olfactory sensory neurons have the same chemoreceptor expression profile and co-express the same ensemble of OR and IR family co-receptors and ligand-specific receptors, male *Ir41l* olfactory sensory neurons do not express *Or82* (Figures 5C-5D and S19N). This sexually dimorphic expression of *Or82* is limited to *Ir41l* olfactory sensory neurons because both male and female *Or3* olfactory sensory neurons express *Or82* (Figures 5C-5D). To confirm that *Or82* is female-specific in *Ir41l* cells and absent from male *Ir41l* cells, we performed multiplex fluorescent RNA *in situ* hybridization on antennae with *Or82* and *Ir41l* probes. As our snRNA-seq data predicted (Figures 5C-5D), *Or82* is expressed and co-localizes with *Ir41l* in females but does not co-localize with *Ir41l* in males (Figure 5E). We detect *Or82* in male antennae (Figure 5D), and find that *Or82* is co-localized with *Or47* and *Or3* in both female and male antennae (Figure 5F) as predicted by our snRNA-seq data. The ligand profile of *Or82* is unknown and it is not known what consequence, if any, the lack of *Or82* in male *Ir41l* olfactory sensory neurons has for dimorphic olfactory behaviors of male and female mosquitoes. This work underscores the striking similarity in chemoreceptor expression between male and female olfactory sensory neurons, with one notable exception.

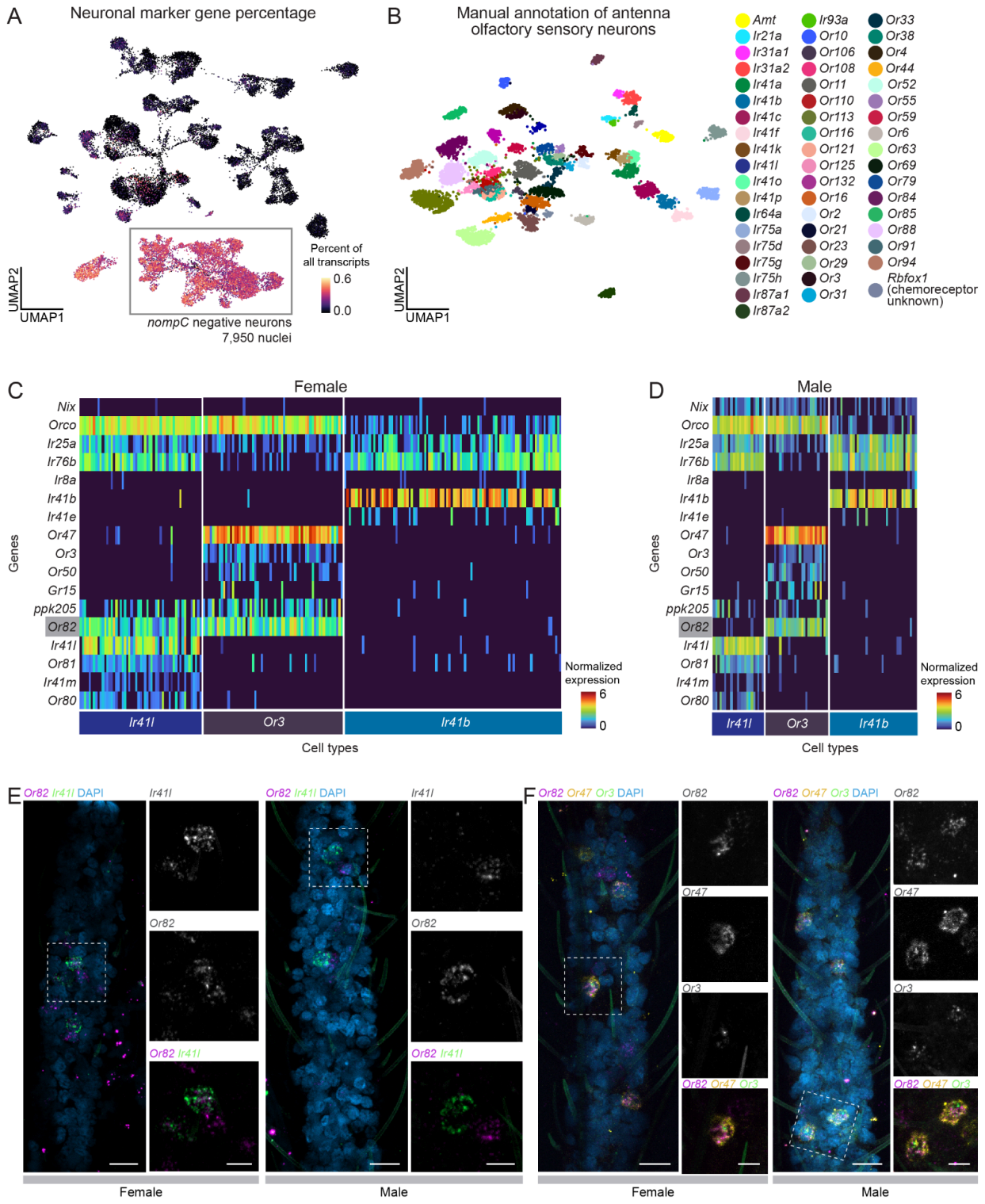
A
Neuronal marker gene percentage
UMAP2
UMAP1
nompC negative neurons
7,950 nuclei
Percent of all transcripts
0.6
0.0
B
Manual annotation of antenna olfactory sensory neurons
UMAP2
UMAP1
Amt
Ir21a
Ir31a1
Ir31a2
Ir41a
Ir41b
Ir41c
Ir41f
Ir41k
Ir41l
Ir41o
Ir41p
Ir64a
Ir75a
Ir75d
Ir75g
Ir75h
Ir87a1
Ir87a2
Ir93a
Or10
Or106
Or108
Or11
Or110
Or113
Or116
Or121
Or125
Or132
Or16
Or2
Or21
Or23
Or29
Or3
Or31
Or33
Or38
Or4
Or44
Or52
Or55
Or59
Or6
Or63
Or69
Or79
Or84
Or85
Or88
Or91
Or94
Rbfox1 (chemoreceptor unknown)
C
Female
Genes
Nix
Orco
Ir25a
Ir76b
Ir8a
Ir41b
Ir41e
Or47
Or3
Or50
Gr15
ppk205
Or82
Ir41l
Or81
Ir41m
Or80
Ir41l
Or3
Ir41b
Cell types
Normalized expression
6
0
D
Male
Genes
Nix
Orco
Ir25a
Ir76b
Ir8a
Ir41b
Ir41e
Or47
Or3
Or50
Gr15
ppk205
Or82
Ir41l
Or81
Ir41m
Or80
Ir41l
Or3
Ir41b
Cell types
Normalized expression
6
0
E
Or82 Ir41l DAPI
Ir41l
Or82
Or82 Ir41l
Female
Male
F
Or82 Or47 Or3 DAPI
Or82
Or47
Or3
Or82 Or47 Or3
Female
Male

Figure 5. Precise sexually-dimorphic expression of *Or82* in a single antennal chemosensory cell type.
(A) Normalized expression UMAP of antenna neuronal genes set: *Syt1* (*AAEL000704*), *brp* (*AAEL018153*), *nSyb* (*AAEL024921*) and *CadN* (*AAEL000597*). Expression of gene set shown as a fraction of total transcripts in each cell. *nompC* (*AAEL019818*)-negative cells highlighted by grey box (for *nompC* gene percentage, see Figure S19B). Normalized expression is ln([(raw count/total cell counts)x median total counts across cells]+1).
(B) UMAP of antenna *nompC*-negative (olfactory sensory) neurons after filtering, colored by manual cell type annotation as listed in legend at the right of the figure panel. For filtering steps and parameters, see Figure S19, Table S2, and Zenodo Supplemental Data. For a complete look up table of gene symbols to gene IDs used in this manuscript, see Table S3. For annotation thresholds see Table S4.
(C-D) Heatmap of cells from female (C) and male (D) samples from annotated clusters *Ir41l, Or3*, and *Ir41b*. Selected genes are indicated in rows and cells indicated in columns. Cell types indicated below heatmap. Heatmap colors represent normalized expression.
(E) Maximum-intensity projection of whole-mount mated, sugar-fed female and male antennae with RNA *in situ* hybridization of *Or82* (magenta), *Ir41l* (green), and DAPI nuclear staining (blue). Scale bar: 10 µm. Right side of each large image: enlarged view of highlighted white box on left, with the indicated probes. Scale bar: 5 µm.
(F) Maximum-intensity projection of whole-mount mated, sugar-fed female and male antennae with RNA *in situ* hybridization of *Or82* probe (magenta), *Or47* (yellow), *Or3* (green) and DAPI nuclear staining (blue). Scale bar: 10 µm. Right side of each large image: enlarged view of highlighted white box on the corresponding left side, with the indicated probes. Scale bar: 5 µm.

Molecular signature of polymodal sensory detection in leg sensory neurons
Aedes aegypti legs enable mosquitoes to evaluate human skin before blood feeding[134], detect pheromones during mating[135–137], and identify suitable egg-laying sites in freshwater[131,138]. They can detect multiple stimuli including osmolality[131], bitter substances[139,140], sugars[141], and amino acids[142]. Mosquitoes have three pairs of legs: forelegs, midlegs, and hindlegs. We collected snRNA-seq data from the most distal segment of the leg, the tarsi, which contains most of the leg's neuronal cell bodies, including mechanosensory and chemosensory neurons[10,143,144] from 332 and 298 female and male mosquito legs, respectively, yielding a total of 29,323 tarsal nuclei (Figure 6A). We identified 1,060 *nompC*-negative neurons, excluding putative mechanosensory neurons (Figures 6B and S21C). Clustering *nompC*-negative sensory neurons revealed cell types with mostly distinct receptor gene profiles (Figures 6C-6D and Zenodo Supplemental Data).

Subpopulations of tarsal sensory neurons showed co-expression of different receptor families. *ppk204* cells express the IR co-receptors (*Ir25a* and *Ir76b*) and ligand-specific genes. Co-expression of IRs and PPKs has also been observed in *Drosophila melanogaster* tarsi snRNA-seq data[145]. *Ir124* cells express several other IR ligand-specific genes as well as *Gr76. Or47* cells co-express *ppk202*, *Gr36*, *Gr76*, *Ir113*, and *Ir114*. Intriguingly, although antennal *Or47*-expressing cells co-express *Orco* as expected (Figures 5C-5D and S20B), tarsal *Or47* cells do not co-express *Orco*, raising the question of whether *Or47* functions in tarsi without what is assumed to be its obligate co-receptor (Figure 6D). We note that GR-expressing cell types also have some expression of the IR co-receptors *Ir25a* and *Ir76b*, although at lower normalized

expression values and more sparsely than cell types that express ligand-specific IRs (Figure 6D). In the proboscis, we observed co-expression of *Orco* and *Or47*, with IR co-receptors and a diversity of ligand-specific IRs (Figure S23C and Zenodo Supplemental Data). These data show that mosquito neurons in the tarsi, as well as the proboscis (Figure S23), can co-express chemosensory receptors across gene families.

Remarkably, tarsal taste neurons also co-express receptors known to operate in distinct sensory modalities including taste, heat, and osmolality, suggesting that some tarsal sensory neurons are polymodal. The low-salt detector *ppk301* enables *Aedes aegypti* females to detect freshwater, helping them avoid laying eggs in toxic high-salt environments[131]. We found that *ppk301* co-expresses with the sweet taste receptors *Gr7* and *Gr9* (Figure 6D). Interestingly, although *ppk301* co-expresses with *Gr7* in the tarsi (Figure 6D), these genes are expressed in separate cell types in the proboscis (Figure S23C), suggesting that mosquitoes may employ receptors combinatorially in different appendages for different sensory coding functions.

Both *Gr7* and *ppk205* cells co-express *TrpA1* (*AAEL001268*), which functions in noxious heat detection[146] (Figure 6D). This co-expression suggests that *Gr7/TrpA1* neurons may detect both sweet taste and heat. *Ir140* is required for heat-related sensory compensation in *Orco* mutant mosquitoes[10] and we found *Ir140* in a cluster with a number of IRs, in addition to *Gr76* (Figure S26E). *ppk304* and *ppk102*, putative orthologues of *Drosophila melanogaster ppk29* and *ppk23* that are required for pheromone detection in the fly[147] are co-expressed in the mosquito (Figures S26F-S26G). Although there were comparatively sparser in chemoreceptor gene expression in other tissues, we found a *Gr39* cell type in the wing and a cell type expressing both *Gr20* and *Gr60* in the abdominal tip (Zenodo Supplemental Data).

We investigated the tarsi, proboscis, and maxillary palp sensory neurons for possible sites of sexual dimorphism (Figures S25A-S25B and S26B-C). The proboscis *Ir7e* cell type was only present in female samples and the tarsal *ppk205/Gr30* cells only in male, although this is based on a small sample of 19 and 12 cells, respectively (Figure S26D). Other cell types were present in different proportions within, but not specific to, male or female samples. We looked for gene expression differences among each cluster, and found no sensory-related genes to be differentially-expressed (Figure S26C and Table S6). This further emphasizes the striking similarity between male and female sensory neurons across sensory organs. Co-expression of receptors sensitive to different sensory modalities has important implications for mosquito behavior. However, many of these genes remain uncharacterized, and future studies will need to examine the functional consequences of the distribution of these receptors within cell types.

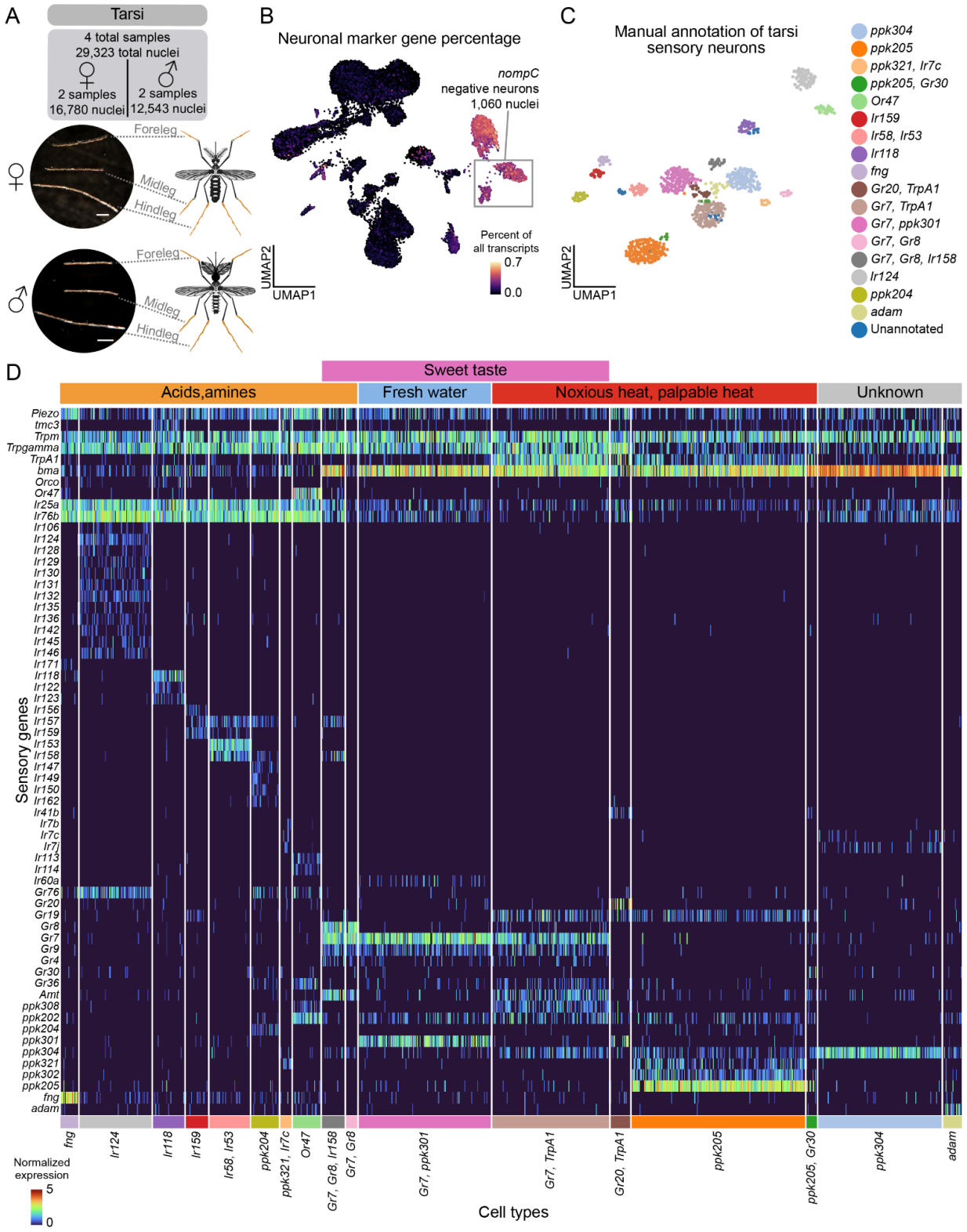
A
Tarsi
4 total samples
29,323 total nuclei
♀
2 samples
16,780 nuclei
♂
2 samples
12,543 nuclei
Foreleg
Midleg
Hindleg
B
Neuronal marker gene percentage
nompC
negative neurons
1,060 nuclei
Percent of
all transcripts
0.7
0.0
UMAP2
UMAP1
C
Manual annotation of tarsi
sensory neurons
ppk304
ppk205
ppk321, Ir7c
ppk205, Gr30
Or47
Ir159
Ir58, Ir53
Ir118
fng
Gr20, TrpA1
Gr7, TrpA1
Gr7, ppk301
Gr7, Gr8
Gr7, Gr8, Ir158
Ir124
ppk204
adam
Unannotated
D
Sweet taste
Acids,amines
Fresh water
Noxious heat, palpable heat
Unknown
Sensory genes
Normalized
expression
5
0
Cell types

Figure 6. Tarsi sensory neurons are polymodal.
(A) Representative photo of mated, sugar-fed female (top) and male (bottom) tarsi dissection with anatomical diagram (in orange; labeling the foreleg, midleg and hindleg). Data was collected from the three most distal segments of the tarsi. Four samples (10x Genomics libraries) yielded 29,323 nuclei from 630 animals, post-quality control filtering. Scale bar: 500 µm
(B) Normalized expression of tarsi neuronal genes set: *Syt1* (*AAEL000704*), *brp* (*AAEL018153*), *nSyb* (*AAEL024921*) and *CadN* (*AAEL000597*). Expression of gene set shown as a fraction of total transcripts in each cell. *nompC* (*AAEL019818*)-negative cells highlighted by grey box. Normalized expression is ln([(raw count/total cell counts)x median total counts across cells]+1). For *nompC* gene percentage, see Figure S24A.
(C) UMAP of tarsi chemosensory (*nompC*-negative) neurons after filtering, colored by manual cell type annotation as listed in legend at the right of the figure panel. For filtering steps, see Table S2 and Zenodo Supplemental Data. For a complete look up table of gene symbols to gene IDs used in this manuscript, see Table S3. For annotation thresholds see Table S4.
(D) Heatmap of cells from all annotated clusters. Sensory genes are indicated in rows and cells indicated in columns. Cell types indicated below heatmap and respective sensory function indicated above. Heatmap colors represent normalized expression.

Sensory neurons express a cell type-specific neuropeptide receptor code
Neuropeptides serve as critical modulators of behavior and physiology in mosquitoes, modifying neural circuit function and behavioral states. In *Aedes aegypti*, over 100 predicted neuropeptides regulate diverse processes, including host seeking, blood feeding, and reproduction[17,148,149]. To ask whether sensory neurons express genes related to neuropeptide and their receptors, we queried 122 genes from these gene families. By analyzing the percentage of cells in each sensory cell type that expresses these genes, we found that while some receptors are broadly expressed in most sensory cell types (e.g. *SIFaR1*, *InR*, *GPRNPY7*, *NPYLR3),* other receptors demonstrated a degree of specificity in their expression patterns that corresponded to the chemosensory receptor expression profiles (Figures S25 and S26A). This receptor code was observed in all sensory tissues analyzed in this study and suggests that neuropeptide signaling could modulate sensory neurons in a cell type-specific manner.

Sexually dimorphic Kenyon cells and glia in the brain
Investigation of the mosquito central nervous system is crucial for better understanding of their unique and sexually dimorphic behaviors[150,151]. We collected samples from the brain (21,820 female and 16,349 male nuclei) and thoracic ganglia of the ventral nerve cord (9,306 female and 8,304 male nuclei) (Figures 7A and S8). After blood feeding, female mosquitoes exhibit unique behaviors, including decreased activity and host-seeking suppression[13–15,17,52,152]. To better understand how this may be regulated by the cells in the brain, we also collected female brain samples 3, 12, 24, and 48 hours after blood feeding (Figure 7A). This yielded a total of 68,898 brain nuclei post-quality control filtering (Figures 7A, 7B, and S27A).

The *Aedes aegypti* brain is estimated to have ~250,000 cells, of which ~220,000 are neurons[153]. In our brain data, 92% of nuclei were neurons and 8% were glia, based on the normalized expression of the markers *nSyb*, and *repo*, respectively (Figures 7C-7D). Because there is no prior literature characterizing subtypes of neurons and glia in the

Aedes aegypti brain, we manually identified cell populations based on marker genes (Figures 7E, S27B, and S28A). We note that many markers are based on ortholog information from *Drosophila melanogaster* and will require further validation.

To understand the depth of our sampling of neuronal cell types in our data, we looked for the central clock cells, a group of fewer than 15 cells in the brain of an adult mosquito[154,155]. We identified a small cluster, marked exclusively by the neuropeptide Pigment-Dispersing Factor (*Pdf*) (*AAEL001754*) and by a set of other circadian rhythm regulatory genes (Figures S28C-S28D), validating our ability to identify rare cell types.

To assist in our annotations, we compared our clustered mosquito brain data to annotated data from *Drosophila melanogaster* head[24] using SAMap, an algorithm that iteratively matches gene homologs and cell types using graph-based data integration[156]. Analyzed separately, neurons and glia each matched with an alignment score of 0.64, compared to a score of 0.47 when we combined fly glia and mosquito neurons as a control (Figures S28E-S28G). Many clusters had high mapping scores to one or a few annotated cell types in the fly cell atlas (Figures S28H-S28J, Table S7, and Table S8). However, because of the considerable evolutionary distance and similarities between neuron types within species, mapping scores between cell types should be regarded with caution, and the lack of a strong mapping score cannot be interpreted as a lack of a corresponding cell type. We identified mosquito Kenyon cells in the mushroom body, a conserved invertebrate brain structure involved in learning and memory[157], both through high SAMap mapping scores and expression of orthologs of *Drosophila melanogaster* Kenyon Cell gene markers (Figures 7F, S28J, S28L-S28P, and Table S7)[24,158].

Using our annotated brain data, we investigated differences within each cell type between male and female brains. We calculated differentially expressed genes between males and females using MAST[55] (Figure 7G, Table S9). Among cell types that had greater than 10 cells in each male and female condition and more than two differentially expressed genes, 28 of 72 were neuronal cell types, and 3 of 5 were glial. Among the frequently differentially expressed genes within each cell type are four genes involved in sex determination and sex-specific neuronal function: *Nix* (*AAEL022912*) and *myo-sex (AAEL021838)* were upregulated in male cell types, and *fru* (*AAEL024283*) and *dsx* (*AAEL009114*) were upregulated in female cell types (Table S7). Curiously, we observed that the presence of *nompC (AAEL019818)*-positive neurons (Table S7) was exclusive to male samples (Figures 7E, S27A, and S28B). Otherwise, we did not observe major differences in the abundance of cell type annotations across sexes (Figure S27A).

Among the Kenyon cells, the cluster expressing *GPRCAL1* (*AAEL010043*) and *Imp1* (*AAEL006876*) (Figures 7H-7I) showed the most sexually-dimorphic gene expression of all brain cell types (Figure 7G). In this Kenyon cell subtype, one of the most upregulated genes in males included *GPRNPY6* (*AAEL017005*), a neuropeptide Y receptor and a highly upregulated female genes included the signaling receptor *Pka-R1* (*AAEL019956*) (Figures 7J and 7L). Glial cells marked by *SVP (AAEL002765*) also exhibited a high number of differentially expressed genes (Figures 7J and 7K). This is consistent with

recent brain snRNA-seq data from *Drosophila* species showing that glial cell types display more divergent gene expression profiles than neuronal cell types[159].

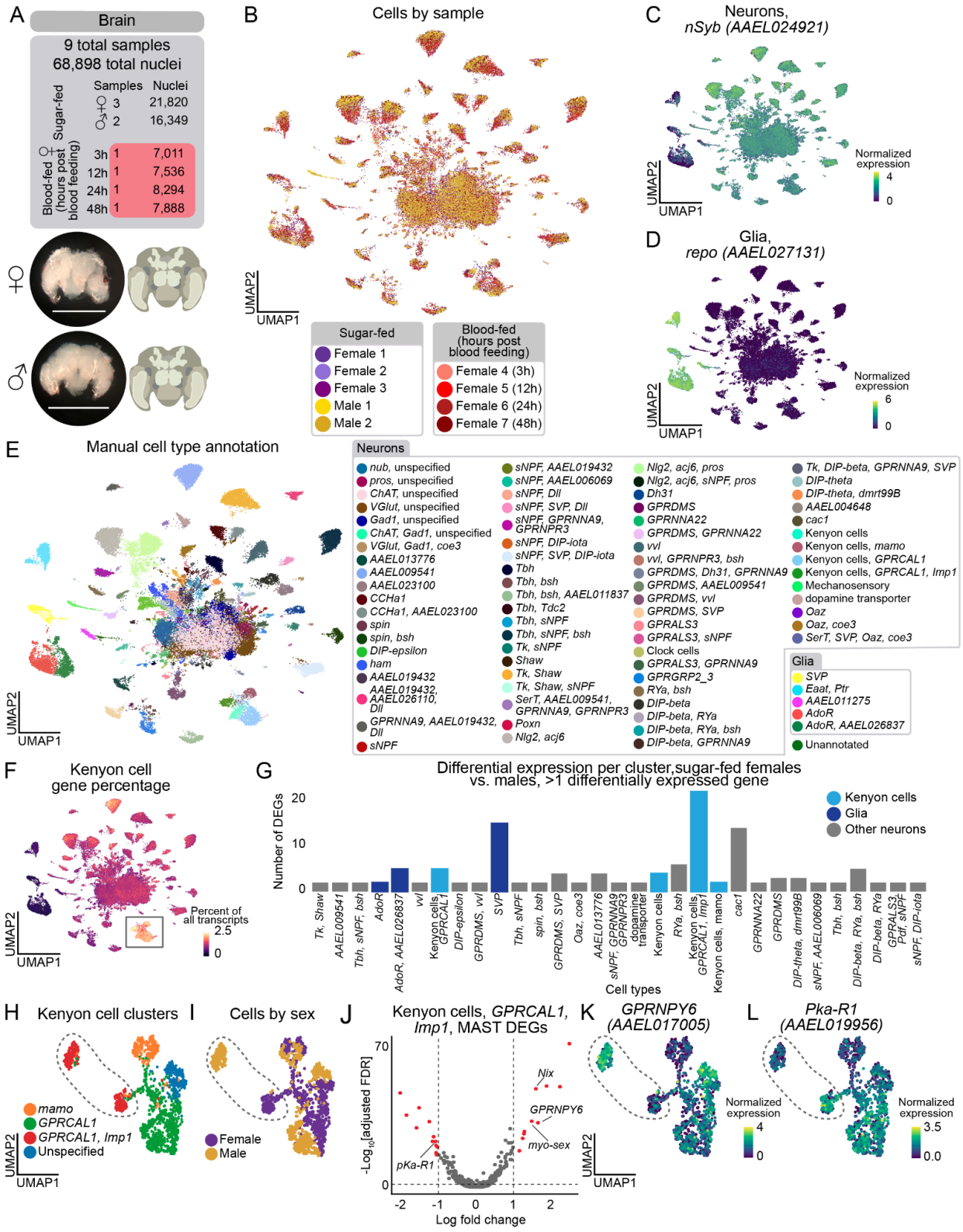

Figure 7. Brain annotation identifies sexually dimorphic Kenyon cells and glia
(A) Representative photo of mated, sugar-fed female (top) and male (bottom) brain dissection with anatomical diagram. Data was collected from sugar-fed and blood-fed female brains 3, 12, 24, and 48 hours after blood feeding. Five samples (10x Genomics libraries) yielded 68,898 nuclei from 182 animals, post-quality control filtering. Scale bar: 500 µm
(B) UMAP of brain nuclei, colored by sample (female samples = 7, male samples = 2).
(C-D) Normalized gene expression UMAP of neuronal marker, *nSyb (AAEL024921)* (C) and glial marker *repo (AAEL027131)* (D) in all brain nuclei. Normalized expression is ln([(raw count/total cell counts)x median total counts across cells]+1).
(E) UMAP of nuclei from all samples, colored and numbered by manual annotation using marker genes, as listed in legend at the right side of figure panel. Major cell type annotations represented in shaded gray headers. For a complete look up table of gene symbols to gene IDs used in this manuscript, see Table S3. For annotation thresholds see Table S4.
(F) UMAP of gene percentage for a set of 30 putative Kenyon cell gene markers (Table S4). Relative expression of gene set shown as a fraction of total transcripts in each cell. Annotated Kenyon cells highlighted by grey box.
(G) Bar plot of number of differentially expressed genes between females and males in each sugar-fed brain cell type. Clusters included contain at least 2 differentially expressed genes with a |log fold change| > 1 and false discovery rate < 0.05, determined by MAST on normalized expression. Clusters colored by cell identity: Kenyon cells (light blue), glia (dark blue), and other neurons (grey). For more information on DEGs, see Table S9.
(H-I) UMAP of reclustered Kenyon cells from all sugar-fed brains, cells colored by manual cell type annotation (H), and by sex (I). Dotted area marks sexually differential expressed Kenyon cells cluster.
(J) Volcano plot of differentially expressed genes (DEGs) in male and female cells in the "*GPRCAL1, Imp1*" Kenyon cluster using MAST analysis. All significant genes (indicated in red) a |log fold change| > 1 and false discovery rate < 0.05, determined by MAST on normalized expression. Male biased genes on right, as indicated by *Nix* (*AAEL022912*) and *myo-sex (AAEL021838)*, female biased genes on left. *pKa-R1* and *GPRNPY6* are labeled.
(K-L) Normalized gene expression UMAP of *GPRNPY6 (AAEL017005)* (K) and *pKa-R1 (AAEL019956)* (L) in reclustered Kenyon cell nuclei from all sugar-fed brains.

Glial cells display dramatic transcriptional changes in the female brain after blood feeding

The ingestion of blood sets off a sequence of dramatic physiological and behavioral events in the female mosquito. To understand these changes from the vantage point of neurobiology with single-cell resolution, we collected female brains at 3, 12, 24, and 48 hours after blood feeding (Figure 8A). For each timepoint post-blood feeding, we calculated differentially expressed genes compared to sugar-fed females using MAST[55] (Figure 8B, Table S10, and Zenodo Supplemental Data). We examined changes in gene expression for each cell type in the female brain across these timepoints. We did not observe any notable changes in cell type abundance across cell types across the four timepoints after blood feeding (Figure S27A).

Contrary to our expectation that neurons would show a strong response to blood feeding, glial cell types had dramatically more transcriptomic changes across blood-feeding timepoints than neurons (Figure 8B). For example, the glial cell type marked by *SVP* (*AAEL002765*) showed the most dramatic transcriptomic shifts with blood feeding compared to any cell type in the brain. *SVP* glia undergo rapid blood

feeding-induced changes in gene expression, with the number of significantly differentially-expressed genes peaking at 3 hours post-blood feeding, and progressively returning closer to the non blood-fed state at later timepoints (Figure 8B). There were 79 significantly differentially expressed genes at 3 hours, 38 at 12 hours, 32 at 24 hours, and 17 at 48 hours. Gene expression shifted from upregulation at 3 hours with 72% of differentially expressed genes upregulated to roughly equal numbers of upregulated and downregulated genes at the three other timepoints (Figure 8C and Table S10).

Neurons in general showed more muted responses to blood feeding, although 38 of 47 neuronal cell types with greater than 10 cells at each timepoint expressed at least two significantly differentially expressed genes. The neuronal cell types marked by "*Nlg2*, *acj6*, *pros*", "*Ngl2*, *acj6*", "*AAEL019432, AAEL026110, Dll"*, dopamine-related genes, "*RYa, bsh"* displayed the highest number of significantly differentially expressed gene(Figure 8B and Table S10). Nevertheless, the differential changes in glia cells were more dramatic than in neurons; for example, the neuron cell type marked by *Nlg2*, *acj6* had fewer differentially expressed genes than any of the glial cell types. The number of differentially expressed genes across timepoints was 7 at 3 hours, 8 at 12 hours, 3 at 24 hours, and no differentially expressed genes at 48 hours (Figure 8D and Table S10).

Next, we investigated the expression dynamics of individual genes at cell type resolution across timepoints. *E75* (*AAEL007397*), *EcR* (*AAEL019431*), and *HR3* (*AAEL009588*) are nuclear steroid hormone receptors that play vital physiological roles in ecdysone signaling. Ecdysone signaling has many functions in insects, including for regulating female reproduction in mosquitoes after blood feeding[160]. All three of these genes are widely expressed in glia and neurons in the non blood-fed female brain (Figures S29A-S29D). Both *E75* and *EcR* show significant upregulation in all glial cell types and several neuronal cell types in at least one timepoint after blood feeding. Their expression is highly upregulated from 3 to 24 hours post-blood feeding, which peaked at 24 hours and then to very low levels by 48 hours post-blood feeding across all cell types (Figures 8E and S29E). Cell type resolution reveals that *E75* and *EcR* upregulation in the brain in the first 24 hours after blood feeding occurs in predominantly glia rather than neurons, suggesting that the post-blood feeding physiological role for *E75* and *EcR* is primarily glia-related (Figures 8E and S29E). *HR3* expression was low across all cell types at 3 hours and 12 hours and then sharply increased at the 24-hour timepoint in both neuronal and glial cell types, suggesting a different mode of function than *E75* and *EcR* (Figure 8F).

Our analyses revealed additional examples of brain cell type-specific gene expression changes post-blood feeding (Figures S29F-S29J). *IA-2* (*AAEL005692*) insulin-like peptide showed upregulation in a small subset of neurons at 12 hours and 24 hours post-blood feeding and then was downregulated in many more subpopulations of neurons and glia at 48 hours (Figure S29F).

fru (*AAEL024283*) and *dsx* (*AAEL009114*) encode transcription factors that regulate sex-specific behaviors and sexual dimorphism in insects. Compared to sugar-fed expression levels, *dsx* was downregulated at 3 hours, 12 hours, and 24 hour timepoints

almost exclusively in glia, and then returned to near-baseline levels by 48 hours (Figure S29G). Conversely, the transcription factor *fru* showed more modest changes in various cell types, although was significantly downregulated in *SVP* glia at 48 hours (Figure S29H). Cell type-specific *fru* regulation has also been observed in *Drosophila melanogaster*, where the male isoform of *fru* masculinizes brain circuitry through unique regulatory patterns of effector genes in different neuronal cell types[161–164]. Whether the downregulation of *Aedes aegypti fru* predominantly in *SVP* glia during blood feeding could play a similar role in the behavioral states of the female mosquito is unknown.

Lastly, the clock genes *ITP* and *PER* showed upregulation specifically in glia (Figures S29I-S29J). Together these data point to potential regulators for gene expression changes both globally and in specific cell types across blood-feeding timepoints in the brain.

Our data confirm that gene expression changes in the female mosquito brain are correlated with blood-feeding state[26]. We found that while these changes occur in some neuronal cell types, the largest transcriptomic changes in the female brain post-blood meal were in glial cell types. The functional implications of these glial transcriptomic patterns during blood feeding and how they might impact mosquito metabolism, physiology, and behavior require further study.

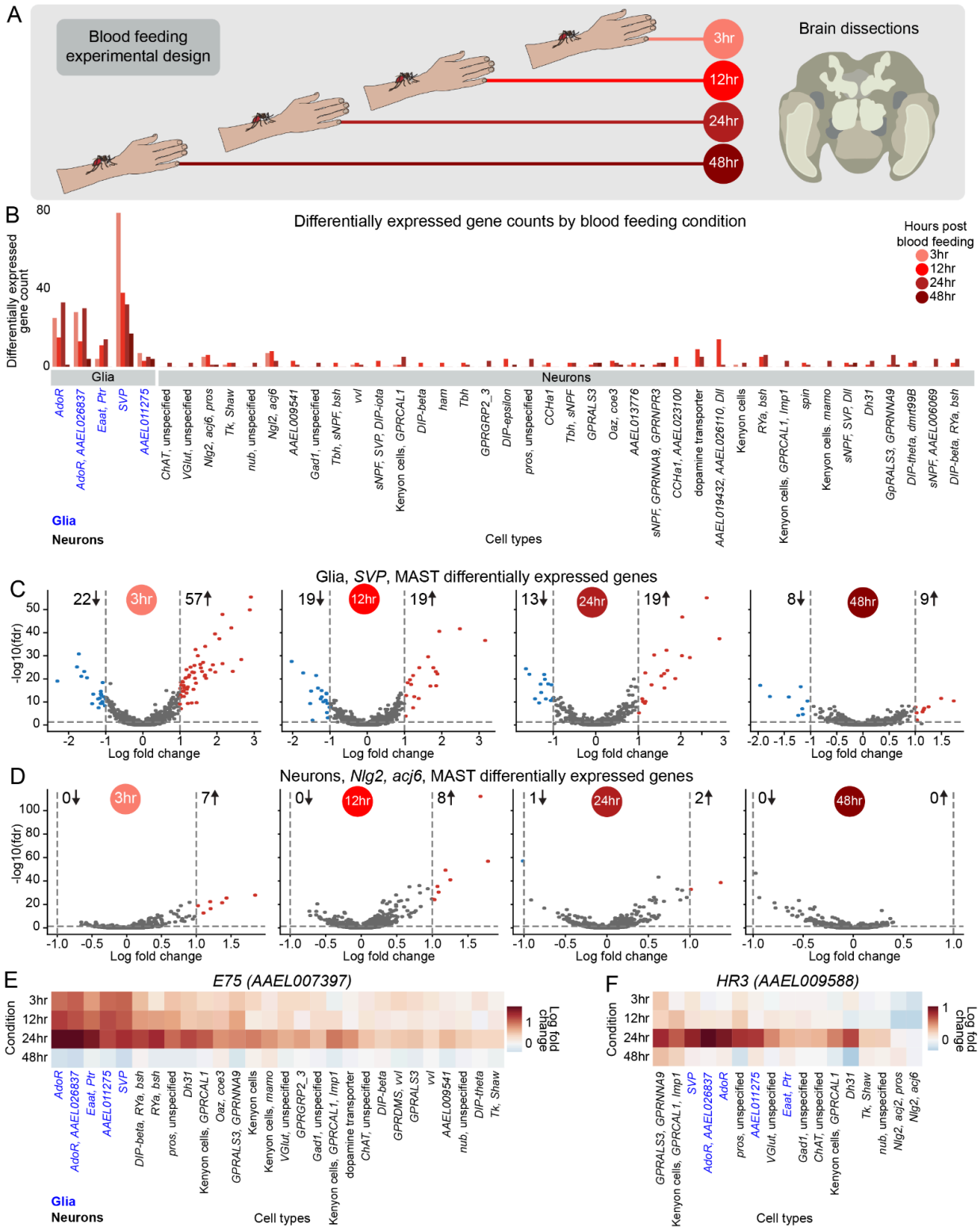
A
Blood feeding experimental design
3hr
12hr
24hr
48hr
Brain dissections
B
Differentially expressed gene counts by blood feeding condition
Differentially expressed gene count
Hours post blood feeding
3hr
12hr
24hr
48hr
Glia
Neurons
Cell types
C
Glia, SVP, MAST differentially expressed genes
22↓
57↑
19↓
19↑
13↓
19↑
8↓
9↑
-log10(fdr)
Log fold change
D
Neurons, Nlg2, acj6, MAST differentially expressed genes
0↓
7↑
0↓
8↑
1↓
2↑
0↓
0↑
E
E75 (AAEL007397)
Condition
Log fold change
F
HR3 (AAEL009588)

Figure 8. Glia show extensive transcriptional changes after blood feeding
(A) Blood feeding experimental design.
(B) Bar plot of number of differentially expressed genes between blood feeding conditions and sugar-fed female brain, per cell type. Bars colored by blood feeding condition. Glia and neuron cell types listed below bars. Genes thresholded on |log fold change| > 1 and false discovery rate (fdr) < 0.05 (determined by MAST on normalized expression, which is ln([(raw count/total cell counts)x median total counts across cells]+1)). For more information on DEGs, see Table S10.
(C-D) Volcano plots of differentially expressed genes between blood feeding conditions in the glial, "*SVP"* cell type (C) and the neuronal *, "Ngl2, acj6"* cell type (D). All significant genes (indicated in red) a |log fold change| > 1 and false discovery rate < 0.05, determined by MAST on normalized expression. Number of downregulated (blue) and upregulated (red) genes at each timepoint is indicated by the down/up arrows.
(E-F) Heatmaps of log fold change of *E75 (AAEL007397)* (E) and *HR3 (AAEL009588)* (F) across blood feeding conditions compared to sugar-fed female brain by cell type. Cell types are sorted by the total log fold change across all timepoints and colored as glia (blue) or neurons (black). Cell types included have over 10 cells in each timepoint, and at least one timepoint where change from sugar-fed condition had a false discovery rate < 0.05.

Discussion

A cell atlas of the adult male and female *Aedes aegypti* mosquito

We present the first comprehensive snRNA-seq cell atlas of adult male and female *Aedes aegypti*, which we expect will serve as a vital resource to the mosquito research community and scientists interested in comparative genomics. This analysis of 367,096 nuclei from 19 tissues provides insights into mosquito cellular diversity and function with a focus on sexual dimorphism across tissues. Using both unbiased approaches and orthology with *Drosophila melanogaster* genes, we identified specific cell type gene markers and annotated individual tissues sampled from the entire mosquito. All data and annotations are available through the UCSC Cell Browser (http://mosquito.cells.ucsc.edu)[66] to allow future exploration of the gene expression and cell types of this deadly disease vector. The *Aedes aegypti* Mosquito Cell Atlas will aid the identification of specialized cell types and their molecular signatures as potential targets for vector control, particularly in disrupting host-seeking behavior or pathogen transmission, and the investigation of sexually-dimorphic and blood feeding-related mosquito physiology and behavior. For example, in the testes we identified cell type-specific markers throughout spermatogenesis that may provide new targets for male sterility approaches for population suppression or be used for developing more effective gene drive strains[165,166]. In the salivary gland, we mapped 24 previously unlocalized secreted proteins via their cell type-specific distribution, which could inform transgenic expression of antiviral effector molecules. Our identification of specialized fat tissue cells expressing antimicrobial peptides provides an opportunity to investigate cells with direct influence on vector competence and mosquito immunity in fighting off viral infection. Beyond potential translational uses of the cell atlas, we anticipate that it will enable further development of molecular tools, including cell type-specific drivers. Finally, we anticipate that these data will be useful for cross-species comparisons[167].

Sexual dimorphic organization of receptors in the antenna
Our analysis revealed several unexpected examples of sexual dimorphism in the *Aedes aegypti* antenna. First, we found previously unknown male-specific *ppk317*-expressing epithelial cells in antennal joints. No counterpart to the *ppk317* cell type in females was identified in our data. We note that this could be due to this cell type not existing in the female, or a related cell type existing in the female but not expressing the *ppk317* gene. Among the *Aedes aegypti* PPK gene family, only *ppk301* has been functionally characterized[131]. However, studies in *Drosophila melanogaster* show that PPKs can have diverse functions. For instance, *ppk4* and *ppk11* are important for larval liquid clearance[129,168], and *ppk23*, *ppk25*, and *ppk29* play a role in male courtship and pheromone detection[147,169–171]. Although the function of *Aedes aegypti ppk317* and these male antennal cells is unknown, the closest homologues in *Drosophila melanogaster* are the *ppk1, rpk*, and *ppk26* gene group[131], which have been implicated in mechanical nociception in multi-dendritic neurons[130,172]. Future genetic and functional work is needed to understand the role of this male-specific PPK gene, and whether this novel cell type in males might be important for male antenna function or behavior.

Second, although there was unexpectedly little sexual dimorphism in chemosensory neurons in the antenna, we did identify a specific cell type marked by *Ir41l* where a single receptor, *Or82*, is absent in male cells and present in female cells. This sexual dimorphism was precise because *Or82* was expressed in both male and female cells marked by *Or3*. This cell type-specific transcriptional regulation suggests active mechanisms both controlling the expression of OR genes and downstream sexually dimorphic sensory processing. In turn, this could allow for the precise tuning of sensory responses across sexes, while maintaining overlapping olfactory responses and behaviors. Such organization might represent an efficient evolutionary solution for developing sexually dimorphic behaviors while preserving essential sensory functions common to both sexes. Investigating the transcriptional regulation of *Or82* could reveal mechanisms controlling sexual dimorphism in sensory systems. The ligand specificity of *Or82* is unknown and it will be interesting to learn if female-specific expression of *Or82* in *Ir41l* neurons is important for an aspect of female-specific sensory behavior.

Widespread receptor co-expression in *Aedes aegypti* sensory appendages
Mosquito sensory neurons challenge canonical principles of chemosensory organization through extensive co-expression of receptors. Our data extend recent findings of co-receptor and ligand-specific receptor co-expression in antennal and maxillary palp neurons[36,37] to other major sensory appendages such as the proboscis and tarsi, suggesting a fundamental organizational principle across mosquito sensory systems. We observe multiple patterns of receptor co-expression. First, neurons frequently co-express multiple ligand-specific receptors from the same family, as demonstrated by *Or82*, *Or3*, and *Or47* co-expression in single antennal cells. Second, we find many examples of cell types that co-express receptors from multiple families (ORs, IRs, GRs, PPKs, TRPs) throughout sensory tissues. This is exemplified by *Or82* expression in *Ir41l* cells, which we validated through RNA *in situ* hybridization. These data suggest that there is coordinated receptor co-expression across gene families.

This complex organization may represent an evolutionary adaptation enabling efficient processing of environmental cues. While co-expression in antennae and maxillary palps has been hypothesized to enhance host detection[36], its presence in proboscis and tarsi suggests a broader strategy. By co-expressing different receptor families, mosquito sensory neurons can process diverse chemical cues simultaneously to enable specificity of behavioral responses in different contexts. Alternatively, co-expression could enable redundant detection that enhances signal reliability. The polymodal nature of some sensory neuron cell types may be particularly advantageous for *Aedes aegypti* as a human specialist, allowing robust host detection despite variations in human odor profiles and continuous environmental changes. Critical questions remain about the molecular mechanisms underlying this organization: Does expression across receptor families lead to co-expression of functional receptor complexes? How do they interact? How is this information integrated by higher-order neurons? Understanding these mechanisms could reveal new approaches for vector control targeting multiple receptor systems simultaneously.

Beyond chemoreceptor gene distribution, we discovered coordinated and specific expression patterns of neuropeptide receptors across sensory neurons cell types. Some receptors show broad expression, while others display restricted patterns correlating with the chemoreceptor expression profiles. This organization could enable modulation based on internal state, like host seeking, post-blood-feeding behavior, and oviposition. Future work should examine how neuropeptide signaling modifies sensory neuron function and whether specific receptor combinations enable flexible adjustment of sensory processing based on global physiological states.

Sexual dimorphism and glial plasticity in the mosquito brain

Our analysis reveals new cell types for the study of sexual dimorphism in the mosquito brain. Kenyon cells, associated with learning and memory[157], in particular those marked with *GPRCAL1* and *Imp1*, show striking sex-related differential gene expression. This includes male-specific expression of neuropeptide Y receptor (*GPRNPY6*) and female-specific expression of protein kinase A receptor (*Pka-R1*), suggesting sex-specific neuromodulation of these circuits. Neuroanatomical evidence supports this sexual dimorphism, with some male Kenyon cells showing larger size despite overall smaller male brains[173]. Given that mushroom bodies process innate behaviors and internal states[174], these sexually dimorphic Kenyon cells may contribute to sex-specific behaviors in mosquitoes such as host seeking or male courtship.

Glial cells emerge as key cell types in both sexual dimorphism and blood-feeding response. Recent comparative work in drosophilids (*Drosophila melanogaster*, *Drosophila simulans*, and *Drosophila sechellia*), showed that glia exhibit the highest expression divergence in the central brain[159]. In *Aedes aegypti*, glia also exhibit higher transcriptomic divergence between males and females than neurons. This points to a fundamental role of glia in the insect brain, where their transcriptional plasticity may provide a permissive substrate for evolutionary and sexually dimorphic plasticity, allowing for the emergence of novel properties without disrupting the more conserved functions of neuronal circuits.

We also show that glial cells, more than neurons, undergo extensive transcriptional changes following blood feeding. The significance of glia in sexual dimorphism and behavioral state transitions suggests a broader glial function than previously recognized[175,176]. Glia may function as master regulators of the mosquito brain, or acutely responsive to sex or state-related cues. Several factors may explain their extensive response.

First, as regulators of blood-brain barrier permeability, glia are ideally positioned to detect blood-derived signals and trigger an immune response if needed[177]. The perineurial glia of the blood-brain barrier demonstrate transcriptomic divergence between *Drosophila sechellia*, which feeds on the low-carbohydrate noni fruit, and *Drosophila melanogaster*, which feeds on yeast on rotting fruit, suggesting that glial transcriptional changes could be related to divergent requirements for sugar uptake in the brain[159].

Second, glia can broadly influence neural circuit function by releasing neuroactive molecules and controlling the extracellular environment[178,179].

Third, given the critical role of glia in neuronal metabolic support[180] and the extensive metabolic demands of blood meal processing[28,181,182], their transcriptional response may reflect adaptation to meet new metabolic needs.

Fourth, the temporal dynamics of glial gene expression, particularly in nuclear steroid hormone receptors like *HR3* and *E75*, suggest a transcriptional cascade that could maintain prolonged suppression of host-seeking behavior after blood feeding.

Understanding how specific glial populations influence neuronal function and behavior through these pathways could reveal novel aspects of glia-neuron interactions and their role in regulating mosquito behavior.

Limitations of the Study

While our cell atlas provides many insights into mosquito cellular diversity, several limitations should be considered. Although snRNA-seq enables unified profiling of all mosquito tissues, nuclear transcriptomes may not fully reflect cytoplasmic mRNA levels and provide no insights into protein expression[183]. This is particularly relevant for chemoreceptor co-expression studies, where post-transcriptional regulation could affect final receptor composition[184]. In addition, other detected transcripts could be untranslated, as seen in the recent work looking at ORs in the clonal raider ant *Ooceraea biroi*[185].

All cell dissociation protocols may introduce bias towards some cell types above others. In mammals, snRNA-seq does not as efficiently capture immune cell types[186,187]. For attached cell types, however, cell lysis and nuclei extraction is typically less biased compared to single cell dissociation methods[47]. Recent work using the same protocol in *Drosophila melanogaster* demonstrated in multiple tissues that collected nuclei ratios accurately reflected *in vivo* cell compositions when compared to histological analysis[48].

Nevertheless, some degree of cell type sampling bias may still exist, and should be taken into account when interpreting these data.

Annotation of the *Aedes aegypti* genome is imperfect. Overlapping gene annotations may lead to multimapping of transcripts during genome alignment and would cause transcripts to be discarded. *Or111* and *AAEL019786* are not visible in the processed data files for this reason. Therefore cautious interpretation of low or undetectable genes is important.

Our annotation relies heavily on *Drosophila melanogaster* orthology despite 260 million years of evolutionary separation[59,60], potentially causing us to miss mosquito-specific adaptations. While we achieved high coverage across tissues with the profiling of 367,096 nuclei, some rare cell types may remain undetected, particularly those comprising few cells per tissue. Furthermore, although we characterized 19 mosquito tissues, most were not discussed in depth in this paper, leaving substantial data for future exploration by the mosquito biology community.

In the antenna, proboscis and tarsi, we observed extensive sensory receptor co-expression. Our validation of sensory gene expression was limited to a few specific cell types. Determining whether those receptors form functional complexes, and characterizing other multi-receptor cell types, will require electrophysiological, genetic, proteomic and behavioral studies. In addition, while we identified sexually dimorphic transcript expression patterns in the antenna and brain, determining whether these differences are causally linked to behavioral dimorphism will require further study.

Conclusion

The *Aedes aegypti* Mosquito Cell Atlas represents a foundational resource for understanding the cellular and molecular basis of male and female *Aedes aegypti* biology. All data, annotations, and analysis tools are freely available through the UCSC Cell Browser at http://mosquito.cells.ucsc.edu[66], enabling researchers worldwide to explore these datasets interactively. We anticipate that this resource will provide immediate value to the vector biology community, accelerate research into mosquito biology, facilitate comparative studies across insect species, and ultimately contribute to the development of innovative strategies for controlling mosquito-borne diseases that threaten global public health.

Resource availability

Lead contact

Requests for resources and reagents should be directed to the lead contact, Nadav Shai (nshai@rockefeller.edu).

Materials availability

This study did not generate new unique reagents.

Data and code availability

Supplementary Figures S1-S29 and Tables S1-S13 accompany the paper. Processed data are available for user-friendly visualization, querying and download through UCSC Cell Browser (https://mosquito.cells.ucsc.edu). Raw snRNA-seq data have been deposited and can be downloaded from NCBI (BioProject: PRJNA1223381). Raw snRNA-seq data from female antenna and maxillary palp samples previously published in Herre, Goldman et al.[36] and re-analyzed in this study can be downloaded from NCBI (BioProject: PRJNA794050). Additional raw and processed data, plots, analysis and custom scripts are available at Zenodo Supplemental Data (https://doi.org/10.5281/zenodo.14890012).

Any additional information required to reanalyze the data reported in this paper is available from the lead contact upon request.

Acknowledgments

We thank members of the Vosshall Lab for comments on the manuscript; Libby Mejia and Melissa Dallesandro for expert mosquito rearing; Colin Berry for providing mosquito larvae for the testes RNA *in situ* hybridization experiment; Connie Zhao, Helen Duan, and Bin Zhang at the Rockefeller Genomics Core; Alison North, Priyam Banerjee, Maria Belen Harreguy Alfonso, Christina Pyrgaki, and Tao Tong at the Rockefeller Bio-Imaging Resource Center (RRID: SCR_017791) for their support and assistance with imaging; Jason Banfelder, Balakanagaram Jayaraman, and Rebecca Bennett at the Rockefeller University High Performance Computing for their expert technical support; Brittney Wick and Maximilian Haeussler for their assistance uploading the data to the UCSC Cell Browser; Bushra Bibi and Vivian Niewiadonski at Novogene for operational help with sequencing; Begüm Aydin, Pyonghwa Kim, Andras Sziraki, and Andrea Terceros for helpful technical discussions; Cori Bargmann, Dana Pe'er, Vanessa Ruta, and Sarah Teichmann for insightful guidance and feedback.

This work was supported by National Science Foundation Graduate Research Fellowship (No. 1946429), Kavli Neural Systems Institute Graduate Fellowship, and the Schmidt Science Fellowship (O.V.G.), L.H.-Z. is a Junior Fellow of the Simons Society of Fellows and was supported by EMBO Long-Term Fellowship (ALTF 1103-2019). J.R awarded the Boehringer Ingelheim Fonds (BIF) PhD Fellowship. Human Frontier Science Program Organization LT000123/2020-L (B.R.H.). NIH awards R01AI151004, RO1AI148300, RO1AI175152, and EPA STAR award RD84020401 (O.S.A). This publication was developed under Assistance Agreement No. RD84020401 awarded by the U.S. Environmental Protection Agency to O.S.A., It has not been formally reviewed by EPA. The views expressed in this document are solely those of the authors and do not necessarily reflect those of the Agency. EPA does not endorse any products or commercial services mentioned in this publication. L.B.D. is supported by R35 GM137888 NIH-NIGMS, Beckman Young Investigator Award, Pew Biomedical Scholar Award, and Klingenstein-Simons Fellowship Award in Neuroscience. H.W.-C. is supported by BBSRC BB/L004445/1. T.R.S. is supported by DP2AI177891 and is a Freeman Hrabowski Scholar of the Howard Hughes Medical Institute. R.S. is employed by SAIL, MSKCC and is supported in part by The Alan and Sandra Gerry Metastasis

and Tumor Ecosystems Center (GMTEC). H.L. is a CPRIT Scholar in Cancer Research (RR200063) and supported by NIH (U01AG086143), the Longevity Impetus Grant, the Welch Foundation, the Ted Nash Long Life Foundation and the Hevolution/AFAR Foundation. This research was supported by the Stavros Niarchos Foundation (SNF) as part of its grant to the SNF Institute for Global Infectious Disease Research at The Rockefeller University. L.B.V. is supported by the Howard Hughes Medical Institute. N.S. was supported by an EMBO Long-Term Fellowship (ALTF 286-2019).

Consortium member support: J.X.D.A. by EPSRC (EP/X025535/1). Y.C. by Temasek Life Sciences Laboratory. J.D. by PhD scholarship from the College of Life Science (University of Leicester). T.L., Y.R., J.R., and M.F.O. by CNPq (308629/2021-3) and Coordenação de Aperfeiçoamento de Pessoal de Nível Superior-Brasil (CAPES)-Finance Code 001. Y.-C.C. by New York University MacCracken Fellowship, NYSTEM institutional training grant (Contract #C322560GG), and Scholarship to Study Abroad from the Ministry of Education, Taiwan. U.P. is supported by EMBO Long-Term Fellowship (ALTF 664-2022), Human Frontier Science Program (LT 0012-2023L), and Stavros Niarchos Foundation (SNF) Institute for Global Infectious Disease Research. J.P. by ANR-20-CE15-006. A.K. by NIH R35GM122592. R.F. by Royal Society University Research Fellowship URF\R\221011. R.C.S by NIH R21AI166857.

Author contributions

O.V.G., H.L., L.B.V. and N.S. together conceived the study.
O.V.G., A.E.D., L.H.-Z., P.L., T.M., J.R., A.R.-V., T.R.S., Y.N.T., M.M.W. and N.S. dissected all the tissues.
Y.Q. performed the nuclei extraction, FACS, and 10x library preparation for all the snRNA-seq experiments with the supervision of H.L.
U.P. assembled the annotation file.
O.V.G. aligned data to the genome and performed quality control filtering with the supervision of R.S.
O.V.G. analyzed all the data with the supervision of R.S.
Y.J. carried out the differential expression analysis in Figures S4-12,S18, S21-22, and S24. with the supervision of T.R.S
H.W.-C. carried out the experiment in Figure 2C.
S.-C.W. performed the analysis for Figure 3D with the supervision of O.S.A
L.D. and L.B.D. provided gene lists for circadian- and neuropeptide-related genes.
A.E.D. carried out experiments in Figures 4F-K, 5E-F, and S18A with the supervision of N.S.
O.V.G., A.E.D. and N.S. annotated the data with expert input from B.R.H., L.B.D., H.W-C., T.R.S. and all members of the Mosquito Cell Atlas Consortium.
Z.M.P. and T.R.S. performed the SAMap analysis.
H.L. and L.B.V. provided funding resources for this project.
O.V.G., A.E.D., L.B.V. and N.S. together designed the figures and wrote the paper with input from all authors.

Declaration of Interests

O.S.A. is a founder of Agragene, Inc. and Synvect, Inc., with equity interest. The terms of this arrangement have been reviewed and approved by the University of California, San Diego in accordance with its conflict of interest policies.

Open access statement

This article is subject to HHMI's Open Access to Publications policy. HHMI lab heads have previously granted a nonexclusive CC BY 4.0 license to the public and a sublicensable license to HHMI in their research articles. Pursuant to those licenses, the author-accepted manuscript of this article can be made freely available under a CC BY 4.0 license immediately upon publication.

STAR★Methods

Key resources table

REAGENT or RESOURCE	SOURCE	IDENTIFIER
Chemicals, peptides, and recombinant proteins		
Schneider's Medium	Gibco	Cat#21720024
Hoechst-33342	Invitrogen	Cat#H3570
Hoechst-33342	ThermoFisher	Cat#H3570
Chitinase	Sigma-Aldrich	Cat#C6137
Chymotrypsin	Sigma-Aldrich	Cat#CHY5S
Slowfade Diamond	Thermo Fisher	Cat#S36972
Triton X-100, 10%	Sigma-Aldrich	Cat#93443
Triton X-100, 10%	VWR	Cat#97063-996
HEPES, 1M	Sigma-Aldrich	Cat#H0887
DAPI	Sigma-Aldrich	Cat#D9542
USB Dithiothreitol (DTT), 100 mM	Thermo Fisher Scientific	Cat#707265ML
$MgCl_2$	MilliporeSigma	Cat#63069
Low TE Buffer (10 mM Tris-HCl pH 8.0, 0.1 mM EDTA)	Thermo Fisher Scientific	Cat#12090-015
Buffer EB	QIAGEN	Cat#19086

50x Protease Inhibitor Cocktail	Promega	Cat#G6521
RNasin Plus Ribonuclease Inhibitor	Promega	Cat#N2615
Falcon 5 mL Round Bottom Polystyrene Test Tube, with Cell Strainer Snap Cap	Corning	Cat#352235
FLOWMI 40 mM Cell Strainers	Bel-Art	Cat#H13680-0040
Kimble Pellet Pestle	Grainger	Cat#6HAY5
Kimble Pellet Pestle Motor	Grainger	Cat#6HAZ6
Wheaton Dounce Tissue Grinder (1 mL)	DWK Life Sciences	Cat#357538
Beckman Coulter SPRIselect	Beckman Coulter	Cat#B23318
C-Chip Disposable Hemacytometers by SKC, Inc	Fisher Scientific	Cat#22-600-100
PBS, pH 7.4, 10X	Fisher Scientific	Cat#70011044
Water Molecular Biology Grade, 500ML	Fisher Scientific	Cat#AAJ71786AP
UltraPure Bovine Serum Albumin (BSA, 50 mg/ml)	Thermo Fisher Scientific	Cat#AM2616
Tween 20	Bio-Rad	Cat#1662404
KCl, 1M, 100ml	VWR	Cat#AAJ63739-AE
Tris Buffer, 1M, pH8.0, 100ML	MilliporeSigma	Cat#648314-100ML
Critical commercial assays		
Chromium Next GEM Single Cell 3' GEM, Library & Gel Bead Kit v3.1	10x Genomics	Cat#1000269
Chromium Next GEM Chip G Single Cell Kit	10x Genomics	Cat#1000127
Single Index Kit TT Set A, 96 rxn	10x Genomics	Cat#1000215
High Sensitivity D5000 Reagents	Agilent Technologies	Cat#5067–5593
HCR RNA *in situ* hybridization probes, amplifiers, buffers	Molecular Instruments	see Table S11
Deposited data		

Aedes aegypti mosquito cell atlas snRNA-sequencing data	This study	BioProject: PRJNA1223381
Female *Aedes aegypti* antenna and maxillary palp snRNA-sequencing data	Herre et al.[36]	BioProject: PRJNA794050
Drosophila melanogaster head snRNA-sequencing data, processed	Hongjie Li et al.[24]	EMBL-EBI Biostudies: E-MTAB-10519
Processed data	This study; Uploaded on UCSC Cell Browser	https://mosquito.cells.ucsc.edu
Additional raw and processed data, plots, analysis and custom scripts	This paper; Zenodo Supplemental Data	https://doi.org/10.5281/zenodo.14890012
Aedes aegypti LVP_AGWG AaegL5.3 genome (including mitochondrial chromosome)	Matthews et al.[53], Sayers et al.[188]	NCBI RefSeq assembly: GCF_002204515.2
VectorBase, LVP_AGWG AaegL5.3 Genome Annotations (Release 58)	Giraldo-Calderón et al.[58]	
Manual chemoreceptor annotation	Matthews et al.[53]	Supplementary Data 18 (Chemoreceptor Annotation.gff3)
the “all translation” file from the FB2023_02 version of the FlyBase genome	Öztürk-Çolak et al.[189]	https://ftp.flybase.net/releases/FB2023_02/dmel_r6.51/fasta/
Experimental models: Organisms/strains		
Aedes aegypti wild-type strain: Liverpool	Leslie Vosshall lab, Laboratory of Neurogenetics and Behavior, The Rockefeller University, New York, NY, USA	N/A
Aedes aegypti wild-type strain: Liverpool (for testes RNA *in situ* hybridization)	Colin Berry Lab, School of Biosciences, Cardiff University, Cardiff, UK.	N/A
Oligonucleotides		
RNA *in situ* hybridization probes	This paper	Table S11
Software and algorithms		
AGAT: Another Gff Analysis Toolkit (Version v1.4.1)	Dainat et al.[190]	https://zenodo.org/records/13799920
GFFutils (Version 0.13)	Dale, R. (2011). gffutils python module	https://daler.github.io/gffutils/

GffRead (Version 0.12.7)	Pertea and Pertea.[191]	https://github.com/gpertea/gffread
Cell Ranger (version 7.1.0)	Zheng et al.[67]	https://support.10xgenomics.com/single-cell-gene-expression/software/pipelines/latest/what-is-cell-ranger
CellBender	Fleming et al.[68]	https://github.com/broadinstitute/CellBender
SCANPY (Version 1.9.6)	Wolf et al.[54]	https://github.com/theislab/scanpy
Python (Version 3.8)	Python Software Foundation[192]	https://www.python.org/
Jupyter Notebooks	Kluyver et al.[193]	https://jupyter.org/
NumPy (Version 1.24.4)	Harris et al.[194]	https://numpy.org/
pandas (Version 1.3.1)	The pandas development team[195]	https://pandas.pydata.org/
Matplotlib (Version 1.3.1)	Hunter[196]	https://matplotlib.org/
Scrublet (Version 0.2.3)	Wolock et al.[197]	https://github.com/AllonKleinLab/scrublet
PhenoGraph (Version 1.5.7)	Levine et al.[198]	https://github.com/jacoblevine/PhenoGraph
SciPy (Version 1.10.1)	Virtanen et al.[199]	https://scipy.org/
seaborn (Version 0.12.2)	Waskom et al.[200]	https://seaborn.pydata.org/
Ensembl Metazoa BioMart, release 56	Cunningham et al.[56]	https://feb2023-metazoa.ensembl.org/index.html
BLAST	Altschul et al.[57]	https://blast.ncbi.nlm.nih.gov/Blast.cgi
VectorBase (orthology tool)	Giraldo-Calderón et al.[58]	https://vectorbase.org/vectorbase/app
MAST (Version 1.26.0)	Final et al.[55]	https://github.com/RGLab/MAST
anndata (Version 0.9.2)	Virshup et al.[201]	https://github.com/scverse/anndata
batchelor (Version 1.16.0)	Haghverdi et al.[202]	https://www.bioconductor.org/packages/release/bioc/html/batchelor.html
SAMap (Version 1.0.15)	Tarashansky et al.[156]	https://github.com/atarashansky/

		SAMap
UCSC Cell Browser	Speir et al.[66]	https://www.cells.ucsc.edu/
Fiji	Schindelin et al.[203]	https://imagej.net/software/fiji/
Zen Blue (Version 3.5)	Zeiss	N/A
Olympus cellSens	Olympus	N/A

Experimental model and study participant details

Human and animal ethics statement

Blood feeding procedures and behavioral experiments with live hosts were approved and monitored by The Rockefeller University Institutional Animal Care and Use Committee (IACUC protocol 23040 (PRV 20068)) and Institutional Review Board (IRB protocol LV-0652), respectively. Human participants gave their written informed consent to participate in this study.

Mosquito rearing and maintenance

Aedes aegypti wild-type (Liverpool) mosquitoes were reared in an environmental chamber maintained at 26°C ± 2°C with 70-80% humidity with a photoperiod of 14 h light: 10 h dark as previously described[133]. Embryos were hatched in 1 L hatching broth: one tablet of powdered Tetramin (TetraMin Tropical Tablets 16110M) in 1 L of deionized water, then autoclaved. Larvae were reared in deionized water (3 L total) and fed 3 crushed Tetramin tablets on the first day post hatching and 2 tablets daily thereafter. To maintain low rearing density, approximately 400 larvae were kept in 3 L deionized water from L3-L4 stage. Adult mosquitoes were supplied with unlimited access to 10% sucrose solution (w/v in deionized water), delivered in a glass bottle (Fisher Scientific FB02911944) with a cotton dental wick (Richmond Dental 201205), and were kept in 30 cm^3 BugDorm-1 Insect Rearing Cages (BugDorm DP1000). Animals were dissected on day 7 of adulthood (14 days post hatching). All animals were co-housed to allow mating prior to dissection.

Method details

Photographs of mosquito tissues

7-14 day-old mosquitoes were cold-anesthetized and kept on ice. The indicated tissues were freshly dissected using using Dumont #5 Forceps (Fine Science Tools 11295-10/11295-20 or Roboz Surgical RS-4955) ice in 1 X PBS (Thermo Fisher Scientific AM9625). Only brains were pre-fixed in 4% paraformaldehyde (Electron Microscopy Sciences 15710-S) in 1X PBS, 0.25% Triton X-100 prior to dissection for 3 h at 4°C. Tissues were placed on a stage micrometer (Fine Science Tools 29025-01) and photographed using an iPhone X (Apple) through the iDu Optics LabCam adapter (iDu Optics) attached to the eyepiece of a Nikon SMZ1500 stereo zoom microscope (Nikon). A scale bar of 500 μM was added to the images using the stage micrometers scale (Fine Science Tools 29025-01).

Tissue collection
Adult wild-type (Liverpool) mosquitoes aged 7 days were aspirated using oral aspirator (John W. Hock Company 612) into a 16 ounce container (Webstaurant KH16A-J8000) and were sealed using double 0.8 mm polyester mosquito netting (ahh.biz F03A-PONO-MOSQ-M008-WT) then anesthetized on ice for 10 minutes. Mosquitoes were then placed in a 40 µm cell strainer (Falcon 352340) in a 100 mm Petri dish (Corning 430293) and soaked in ice-cold molecular-grade 100% ethanol (Sigma-Aldrich E7023 or Fisher Scientific BP2818500) for 5-10 seconds. The animals were rinsed in ice-cold Schneider's Medium (Gibco 21720024) and placed in a clean Petri dish with approximately 20 mL ice-cold Schneider's Medium on a reusable ice pack (GenTap, Cooler Shock. Amazon.com 854850006121). Tissues of interest were dissected using Dumont #5 Forceps (Fine Science Tools 11295-10/11295-20 or Roboz Surgical RS-4955) on a 100 mm Petri dish (Corning 430293) lined with or without SYLGARD 184 silicone (World Precision Instruments SYLG184). Tissues were placed directly into a DNA LoBind 1.5 mL tube (Eppendorf 022431021) pre-wet with 100 µL Schneider's Medium on wet ice or in a 70 µm cell strainer (pluriSelect 43–10070-70) and DNA LoBind 1.5 mL tube (Eppendorf 022431021) pre-wetted with 100 µL Schneider's Medium on ice by inverting the cell strainer over the Eppendorf tube using Dumont #5 Forceps (Fine Science Tools 11295-10/11295-20 or Roboz Surgical RS-4955) and pipetting 300 µL ice-cold Schneider's Medium onto the strainer to expel the tissue. Each sample was collected in 90 minutes or less. The Eppendorf tube was wrapped in parafilm (Bemis Company Inc. PM996), flash-frozen in liquid nitrogen and stored at -70°C. All tissues were dissected in the Vosshall Laboratory at Rockefeller University. With the exception of two antenna samples, all samples were shipped to Baylor College of Medicine on dry ice for nuclei extraction. For individual sample information, including number of mosquitoes, dissection tube IDs, see Table S1 . Further information on individual dissection tube IDs that were pooled together for samples, including start time of 90 minute dissection session is available in Table S12.

Human arm feeding for blood-fed brain samples
Approximately 30 4-7 day old female mated adults were aspirated into a 30 cm^3 BugDorm-1 Insect Rearing cage (BugDorm DP1000) and allowed to feed on a human arm for 20-30 minutes. One human subject was used for all blood feeding. Fed females were placed in an environmental chamber maintained at 26°C ± 2°C with 70-80% humidity with unlimited access to 10% sucrose solution until they reached 7 days of adulthood and were dissected. Brain dissections and collections were performed as described above.

Single-nucleus suspension
Single-nucleus suspensions were prepared as described previously[204]. Thawed samples were spun down using the bench-top centrifuge, removing the Schneider's medium as much as possible. Samples of like tissues were combined into one tube using a pipette with wide-bore tips and then centrifuged. Specific large tissues (abdomen, thorax and abdominal pelt) were ground using a pestle motor (Kimble 6HAZ6) for 30 seconds on ice after thawing (Table S1).

Samples were resuspended in 900 µL of fresh homogenization buffer (250 mM sucrose, 10 mM Tris PH 8.0, 25 mM KCl, 5 mM $MgCl_2$, 0.1% Triton-x 100, 0.5% RNasin Plus, protease inhibitor, 0.1 mM DTT in 10 mL nuclease-free water) and transferred into a 1 mL Dounce (Wheaton 357538). Sample tubes were rinsed in 100 µL of homogenization buffer and transferred into the same dounce. Dounce sets were autoclaved at 200ºC for more than 2 hours before each use.

Nuclei were released by 20 strokes of loose dounce pestle and 40 strokes of tight dounce pestle. 1000 µL of the samples were filtered into a 5 mL tube through 35 µM cell strainer cap (Corning 352235) and then filtered using Flowmi (40 µM; BelArt H136800040) into a 1.5 mL Eppendorf tube. After 10 minutes of centrifuging at 1000g at 4ºC the pellet was resuspended using 500 µL of 1xPBS/0.5% BSA with RNase inhibitor (9.5 mL 1x PBS, 0.5 mL 10% BSA, 50 µl RNasin Plus). Mechanical nucleus extraction is typically estimated to recover approximately 10% of the total nuclei from tissue samples, as previously documented[205].

Fluorescence-activated cell sorting (FACS)
Samples that underwent FACS were filtered using a 40 µm Flowmi into a new 5 mL FACS tube (Corning 352052) and kept on ice. 10 µL of the sample was moved into a new 5 mL FACS tube with 190 µL PBS as unstained control for FACS. Nuclei were stained with Hoechst-33342 (Invitrogen H3570) on wet ice (1:1000; >5 min). Hoechst-positive nuclei were collected using the BD FACSAria III Cell Sorter (BD Biosciences). 80k–150k individual nuclei were collected into one 1.5 mL RNAse-free Eppendorf tube with 300-500 µL 1x PBS with 0.5% BSA as the receiving buffer (with RNase inhibitor). Next, nuclei were centrifuged for 10 min at 1000 g at 4°C, and resuspended using 30 µL of 1x PBS with 0.5% BSA (with RNase inhibitor). FACS files, including gating strategy, are available in Zenodo Supplemental Data (file names for each sample listed in Table S1).

Nuclei counting
2 µL of the nucleus suspension was used to calculate the concentration on a hemocytometer (Fisher Scientific 22-600-100). Because we have found capture efficiency to be typically around 50-65% (Table S1), 20,000 nuclei per sample were loaded on the Chromium 10x Controller (10x Genomics) to recover approximately 10,000 cells after sequencing. Excess nuclei were discarded. The nuclei capture protocol used (10x Genomics) has a limit of approximately 10,000 nuclei per sample. We note that the number of nuclei recovered is not a reflection of the nuclei yield from the original tissue amount. For most samples, we collected more tissue and extracted more nuclei than necessary to ensure availability at this step was not a limitation towards the final number of nuclei we recovered.

For specific tissues with limited nuclei (male and female malpighian tubules, male wings and female stylet), we maximized nuclei yield by using all Hoechst-positive nuclei from single-nucleus suspensions were collected with FACS, and the counting step was

skipped. Nuclei suspension concentration for loading was estimated via FACS (Table S1).

Library preparation and sequencing

10x Genomics sequencing libraries were prepared following the standard protocol from Chromium Next GEM Single Cell 3' GEM, Library & Gel Bead Kit v3.1 (10x Genomics 1000269) with the following settings. All PCR reactions were performed using C1000 Touch Thermal cycler with 96-Deep Well Reaction Module (BioRad 1851197). Cycle numbers were used as recommended in 10x protocol for cDNA amplification and sample index PCR. As per 10x protocol, 1:10 dilutions of amplified cDNA were evaluated using a Qubit fluorometer (Thermo Fisher). Final libraries were evaluated using TapeStation (Agilent). The final libraries were sent to Novogene Corporation Inc. (Sacramento, California, USA) for Illumina NovaSeq PE150 S4 lane sequencing with the dual index configuration Read 1 28 cycles, Index 1 (i7) 10 cycles, Index 2 (i5) 10 cycles and Read 2 91 cycles. Given our target of 10,000 cells per sample, we aimed for a sequencing depth of approximately 80,000 reads per nucleus (Table S1).

Antenna samples prepared without FACS

All samples were prepared with the above protocol, with the exception of two female antenna samples (see Table S1 and Figure S17C). These samples were not FACS-sorted prior to library creation. Methods of data collection for these samples is published in Herre, Goldman et al. 2022 ("Rockefeller" sample)[36]. The concentration of nuclei was determined by counting cells on a Luna FX7 automated cell counter (Logos Biosystems L70001) prior to library creation. Libraries were created using the standard protocol from Chromium Next GEM Single Cell 3' GEM, Library & Gel Bead Kit v3.1 (10x Genomics 1000269). Images from automated cell counting are available in Zenodo Supplemental Data.

Testes RNA *in situ* hybridization and imaging

Hybridization chain reaction RNA fluorescence *in situ* hybridization (RNA *in situ* hybridization) was conducted in whole male testes to detect RNA, using an adaptation of published protocols[206,207]. 1-3 days old adult male *Aedes aegypti* wild-type (Liverpool), were anesthetized at 4°C for 10 minutes. Testes were dissected from male mosquitoes in ice-cold PBST (1X PBS, 0.1% Tween-20) with 0.5% formaldehyde using Dumont biology tweezers (Agar Scientific T5291). The terminal abdomen was removed by grasping the upper abdomen and genitalia with separate pairs of forceps. Testes and male genital tract were cleaned of excess fat tissue. Dissected testes were fixed in 4% paraformaldehyde (made from 40% stock: 0.368 g paraformaldehyde, 1 mL RNase-free water, 7 µL 2N KOH, heated until dissolved and filtered through 0.3 µm filter) in PBST for 30 minutes at room temperature. Samples were washed twice in PBST for 5-10 minutes each, then dehydrated in 100% methanol and stored at -20°C in 100% methanol for up to 2 weeks. Prior to hybridization, samples were rehydrated by rinsing once in 70% ethanol and stored overnight at 4°C in 70% ethanol. The next day, samples were transferred to 0.2 mL PCR tubes (Azenta Life Sciences PCR1174) and rinsed twice with PBST. Samples were then pre-hybridized in 30% probe hybridization buffer (30% formamide, 5X SSC, 0.1% Tween 20, 50 µg/mL heparin, 5X Denhardt's solution,

and 10% dextran sulfate) at 37°C for 30 minutes. Probe solution was prepared by adding 0.4 µL of 100 µM probe stock to 100 µL hybridization buffer (Full list of probe sequences can be found in Table S11). Both samples and probe solution were heated to 80°C for 5 minutes before combining. Hybridization was performed overnight at 37°C in dry bath. Following hybridization, samples were washed four times for 20 minutes each in pre-warmed probe wash buffer (30% formamide, 5X SSC, 0.1% Tween 20, and 50 µg/mL heparin) at 37°C. Hairpin amplification was performed by heating 2 µL of each hairpin to 95°C for 90 seconds, cooling to room temperature for 30 minutes, then adding to 50 µL amplification buffer (5X SSC, 0.1% Tween 20, and 10% dextran sulfate). Samples were incubated in amplification buffer for 30 minutes at room temperature before overnight incubation with hairpin solution at room temperature in the dark. Samples were washed 5 times with 5X SSCT (5X SSC and 0.1% Tween 20) for 5 minutes each, followed by three 5-minute washes in 1X PBS. Tissues were then mounted in mounting medium on a cover slip and imaged. Images were acquired using an Olympus BX63 microscope (Olympus) equipped with a Cool LED pE-300 light source and Hamamatsu ORCA Spark camera (Hamamatsu Photonics C11440-36U), using 20x/0.80 UPlan XApo objective (Figures 2C-2F) or Olympus Uplan Fl 40x/0.75 objective (Figure 2G). Images were acquired as a 1920x1200 size image. Image acquisition was performed using Olympus cellSens software.

Antennae RNA *in situ* hybridization

RNA *in situ* hybridization was conducted in whole mount female and male antenna to detect RNA using adaptations of published protocols[36,206,208]. Products including HCR custom probes, amplifiers, probe hybridization buffer, probe wash buffer, and amplification buffer were purchased from Molecular Instruments Inc. (https://www.moleclarinstruments.com). All staining steps were done in a modified cell strainer snap cap (Fisher Scientific, Falcon 352235) in a well of a 24-well plate (Fisher Scientific, Falcon 353047).14-day-old adult Liverpool mosquitoes were anesthetized on wet ice. Antennae were dissected in a bubble of ice-cold 1X PBS (Thermo Fisher Scientific AM9625) in a 100 mm Petri dish (Corning 430293) lined with SYLGARD 184 silicone (World Precision Instruments SYLG184) on a reusable ice pack (GenTap, Cooler Shock. Amazon.com 854850006121) using Dumont #5 Forceps (Fine Science Tools 11295-10/11295-20 or Roboz Surgical RS-4955). Samples were digested in a chitinase-chymotrypsin solution [119 mM NaCl, 48 mM KCl, 2 mM $CaCl_2$, 2 mM $MgCl_2$, 25 mM HEPES, 5 U/mL chitinase (Sigma-Aldrich C6137-50UN), 100 U/mL alpha-chymotrypsin (Sigma-Aldrich CHY5S-10VL), 1% DMSO] rotating at 37°C for 1.5 hours. Antennae were washed in 1% PBS, 0.1% Tween-20 (PBST) for 10 minutes three times at room temperature. Samples were then fixed in 4% paraformaldehyde (Electron Microscopy Sciences 15710-S) in 1X PBS, 0.025% Triton X-100 for two hours at room temperature, following six five-minute washes at room temperature in PBST. Antennae were then dehydrated at 4°C in a stepwise sequence of 25% methanol/PBST, 50% methanol/PBST, 75% methanol/PBST, then 100% methanol twice, for 10 minutes at each step. Samples were kept in 100% methanol overnight at -20°C. The following day tissues were rehydrated at 4°C in a stepwise sequence of 75% methanol/PBST, 50% methanol/PBST, 25% methanol/PBST for 10 minutes each. At room temperature, samples were washed in PBST four times for ten minutes, fixed in 4%

paraformaldehyde in PBS with 0.1% Tween for 20 minutes, and then washed again in PBST three times for 15 minutes. Antennae were transferred to preheated probe hybridization buffer at 37°C for 30 minutes. 8 µL of 1 µM stock of each probe was added to 800 µL of preheated probe hybridization buffer at 37°C, samples were transferred to this probe solution for two nights and kept at 37°C (Full list of probes can be found in Table S11). They were then washed four times for 15 minutes at 37°C in probe wash buffer, followed by four 15-minute washes in 5X SSC (Invitrogen 15557044) in nuclease-free water, 0.1% Tween 20 solution (SSCT) at room temperature. Antennae were then incubated in amplification buffer for 30 minutes at room temperature. Hairpin amplifiers were combined and activated per the manufacturer's instructions. 8 µL of 3 µM stock hairpins were added to 800 µL of amplification buffer at room temperature overnight in the dark. At room temperature, samples were washed in SSCT twice for 15 minutes, incubated in 1:500 DAPI (Sigma-Aldrich D9542-5MG) in SSCT for one hour, then washed again in SSCT five times for 15 minutes. Tissues were then mounted on slides in SlowFade Diamond (Thermo Fisher S36972), topped with a coverslip, sealed with clear nail polish, and stored at 4°C until imaged.

Antennal imaging and image processing

Confocal images of antennae were acquired on a Zeiss Axio Observer 7 Inverted LSM 980 scanning confocal microscope (Zeiss) with a 63x/1.40 PlanApochromat Oil DIC M27 objective. The sample was scanned bidirectionally without averaging (Figures 5E-5F and S18A) or with 4x averaging (Figures 4F-4K). The images were acquired as a standard 1024x1024 size image, which, depending on the zoom used, resulted in a voxel size of 0.0658 µm x 0.0658 µm x 0.24 µm (for Figures 4F-4K) or 0.1315 µm x 0.1315 µm x 0.26 µm (for Figures 5E-5F and S18A). Zen Blue v3.5 software was used for image acquisition.

For all comparative experiments, image acquisition parameters were kept consistent. We note that all confocal imaging was conducted in a manner that would maximize our ability to visualize the presence or absence of each fluorophore and was not intended as a quantitative measure of fluorescence intensity. Confocal images were processed in ImageJ (NIH). Brightness/contrast was adjusted to maximize visualization, and for all comparative experiments, adjusted parameters were kept consistent.

Quantification and statistical analysis

Gene Annotation File

Gene annotations were prepared from VectorBase (www.vectorbase.org, Release 58, as of June 2022) using the *Aedes aegypti* LVP_AGWG AaegL5.3 Genome[53,58]. These were merged with the manual chemoreceptor annotation from[53], then double checked and corrected for errors manually as well as using AGAT[190] and then processed using gffread[191]. For quick identification in downstream analyses, the prefixes “MT-”, “RP-” and “RR-” were appended to all AAEL gene IDs for mitochondrial, ribosomal protein, and rRNA genes, respectively. Final annotation file was assembled using Cell Ranger package (version 7.1.0) function *mkgtf*[67] using the *Aedes aegypti* genome, including the mitochondrial chromosome, downloaded from NCBI (NCBI RefSeq assembly:

GCF_002204515.2)[53,209]. Gene annotation file (including prefixes identifying MT, PR, and RR genes) is available in Zenodo Supplemental Data.

Alignment and ambient RNA removal

FASTQ files were aligned using 10x Genomics Cell Ranger 7.1.0 (include-introns set to "true")[67]. While the Cell Ranger performs alignment, PCR duplication correction and identification of empty droplets, the cells are susceptible to ambient RNA noise. A droplet containing a nucleus may also contain remnant floating RNA, which can occlude the nucleus' expression. We therefore used the CellBender package[68] for ambient RNA correction (epochs = 200, fpr = 0.01). We used the Cell Ranger cell count estimate as the number of expected cells and set the number of total droplets to the recommended default value (generally 30,000 droplets for typical samples). We selected the learning rate based on the smoothness of ELBO value along the epochs, as suggested by the developers. For most cases, we used the default learning rate and in cases where the ELBO value was "wobbly" we chose x0.1, x0.5 or x0.01 as suggested in the CellBender package[68]. A list of parameter values is provided in Table S1 and scripts used for Cell Ranger and CellBender are available in Zenodo Supplemental Data.

Prior to ambient RNA removal, on average for each sample, we sequenced 115,918 reads/nucleus, a median of 1,417 genes/nucleus and 3,809 UMI counts/nucleus, with a sequence saturation of 82% (for metrics on individual samples, see Table S1). On average across an entire sample, we detected a total of 16,285 out of 19,920 annotated genes (Table S1).

Quality control and cell filtering

For all downstream analysis, we used the Scanpy package (referred to as sc from here on[54], in Python[192,210] in addition to standard Python libraries such as numpy, pandas, matplotlib, csv, os, datetime[194–196]. Most analysis was carried out in Jupyter notebooks[193], and all scripts and additional data are available on Zenodo Supplemental Data.

Quality control metrics: We began by evaluating basic quality control metrics using *calculate_qc_metrics* function in Scanpy in each sample. We evaluated the distribution of each metric such as the total counts in a cell, total number of genes expressed in a cell and the number of cells each gene is expressed in to filter for high quality cells and genes. We also evaluated Mitochondrial (MT), rRNA (RR), and ribosomal protein (RP) fractional expression distribution across cells. These metrics are associated with apoptotic cells or are typically uninformative[211], hence understanding their contribution to the expression of each cell is important. To err on the conservative side, we began by removing only a few cells that were clearly noisy or outliers. Specific parameters and scripts for each sample are in Table S1 and Zenodo Supplemental Data.

We also performed basic filtering in the gene space. First, as a standard practice in the analysis of scRNA-seq data, we removed RP genes from downstream computation, as they are typically uninformative and are often confounders in biological signals[211]. Additionally, to reduce noise in the data, genes that were expressed in fewer than 12

cells were also removed, unless they were registered as possibly biologically meaningful after discussion with Aedes aegypti Mosquito Cell Atlas co-authors. For this, we compiled a list of around 2,464 genes that were of interest based on the current literature (see Zenodo Supplemental Data).

Data Normalization: After basic clean-up, each sample was median library size normalized followed by log-transformation, which was recently shown to perform just as well, if not better, than more sophisticated transformations[212]. We used *sc.pp.normalize_total* function in Scanpy and took the natural logarithm of the data with a pseudocount of 1 to preserve zeroes. We then computed the top 4000 highly variable genes (*sc.pp.highly_variable_genes*), followed by a principal component analysis (PCA, 30 components). We then computed k-nearest neighbors using *sc.pp.neighbors(n_neighbors=30, use_rep='X_pca', metric='euclidean')* function in Scanpy. UMAP, tSNE, Force Directed Layout (FDL) visualizations were used for visualization of data in 2D.

Doublet detection: For doublet detection, we used the scrublet package[197]. Scrublet expects an estimate of doublets as an input, for which we used the formula $y = 0.000759x + 0.052721$ from the expected multiplet table provided by 10x Genomics, where x is the total number of cells in the dataframe. The predicted doublets were then analyzed together with other quality metrics for data clean-up as described below.

Cell type-informed data filtering: Combining all the metrics discussed above, cell filtering was performed through identification of low quality clusters. A typical strategy to filter individual cells relies on individual metrics such as library size or doublet score, which can be manual and less generalizable. We instead sought to utilize the entire transcriptome to first group cells and filter out clusters of cells that cumulatively have low quality scores for the above described set of metrics: doublet score, mitochondrial gene fraction, ribosomal protein fraction, total counts, gene counts and cell type-specific gene expression. We removed clusters of cells that demonstrated low quality features (Table S1). To do this systematically, we first identified obvious outlier clusters, using which we defined a threshold that was uniformly applied to all clusters in each sample. For clustering we used the PhenoGraph[198] package with the Leiden algorithm (resolution_parameter = 5 or 10, see Table S1) as implemented in the *sc.external* module. We chose such a high value of resolution_parameter, which results in a large number of clusters, to ensure that only highly specific noisy clusters were removed from downstream analysis. At minimum, clusters from all samples were removed that had a mitochondrial gene fraction of 5 or higher, and a doublet score of 0.3 or higher (Table S1). In many cases, these thresholds were adjusted based on their distribution to retain only high-quality cells for downstream analysis (see individual sample scripts in Zenodo Supplemental Data), because low-quality cells confound the characterization of real biological features in the data. Thus, we prioritized our analysis on high quality cells to enhance our understanding of these uncharacterized cell types with minimal exceptions (see testes data below),

Because there is limited prior knowledge on basic quality metrics for single-nuclei data from mosquitoes, we sought to biologically guide and complement our cell-filtering

strategy using whatever limited information we have about cell type markers in mosquitoes. For the purposes of a preliminary annotation to inform cell filtering strategy, we queried genes that appear often in most samples and utilized those to represent broad cell type categories. In particular, we used *AAEL024921* (*nSyb*) for neurons, *AAEL027131* (*repo*) for glia, *AAEL019468* (*Ppn*) for hemocytes, *AAEL001168* (*grh*) for epithelial-like cells, *AAEL002417* (*troponin T*) for muscle, *AAEL001194* (*FASN1*) for fat cells. We also included *AAEL019457* (*Lim1*), a commonly expressed transcription factor, that typically labels a discrete subset of cells. Cells that expressed these genes were typically not removed in filtering and used as reference for setting thresholds (described above) and identifying outlier clusters (Table S1).

To validate male and female samples, we also queried *AAEL022912* (*Nix*), which showed markedly differential expression in male and female samples, as expected[26,213].

Samples were then each reprocessed, which included renormalizing the data, re-computing highly variable genes, PCA, and nearest neighbors. Same sets of parameters were used. For clustering, we used the Jaccard + Louvain algorithm implementation of PhenoGraph at resolution 1 for downstream annotation and analysis, unless indicated otherwise[198,199]. Preliminary annotation was performed on each sample as described in the next section. Only one round of filtering (or cluster removal) was performed for each sample. Preliminary annotation was performed on each sample individually.

***Exception for testes sample*:** We processed the testes sample both with and without CellBender. We observed that CellBender discarded more 6,151 nuclei compared to Cell Ranger. We reasoned that these might be spermatids, which after meiosis slow transcription, and therefore have low transcript counts[70]. For this reason, to detect spermatids in our snRNA-seq data, we did not apply ambient RNA removal and did not discard clusters with features such as low UMI-count (Figures S14A-S14D). Spermatids were readily identifiable by their low transcript count and their expression of *S-Lap* (*AAEL000108*), *DBF4* (*AAEL008779*)[72], and *Orco* (*AAEL005776*)[73] (Figures 2B, S14E-S14G). To avoid potential batch effects (from lack of ambient RNA removal) in the integrated *Aedes aegypti* Mosquito Cell Atlas object (Figures 1C-1F and S3), we used the testes data that were processed with ambient RNA removal and thus lacks spermatids. Testes data processed without CellBender are available on UCSC Cell Browser (http://mosquito.cells.ucsc.edu) and with CellBender at Zenodo Supplemental Data.

We note that the testes sample (without CellBender), as well as others, including those collected from male reproductive glands, and the male and female malpighian tubules, have low fraction reads in cells (Table S1). This may be due to technical artifacts within these particular samples that lead to increased ambient RNA or may indicate the possibility of additional low RNA-count cell populations. Without biological reasoning (such as in the case of spermatids) and specific gene markers to identify low RNA-count cell populations, we did not investigate these other potential cell populations.

Sample merging
In cases where we had multiple samples for a tissue, we merged data, including male and female samples. In general, for a more robust annotation of cell types informed by a greater number of cells, and to enable comparison across sexes, we merged male and female samples. Our preliminary annotations (see Methods: Annotations and gene selection) showed in most cases a noticeable similarity in general cell types in male and female samples. We used *AnnData.concatenate* function[201] and repeated the processing as described above. Genes expressed in fewer than 18 cells were removed unless they were present in a more comprehensive list of genes of interest (20,587 genes, see Zenodo Supplemental Data). We then renormalized the data, re-computed highly variable genes, principal components (PCs), nearest neighbors, and re-clustered as described above, unless indicated otherwise. See Table S2 for list of final objects. All objects available through either UCSC Cell Browser (https://mosquito.cells.ucsc.edu) or Zenodo Supplemental Data.

Batch correction
In the case of the two merged ovary samples, we saw a noticeable batch effect of unknown origin (Figure S1G). We batch-corrected all genes using *batchelor.fastmnn*[202]. Quality control and filtering was done iteratively and informed by annotations on individual and merged samples. It was not necessary to batch correct any other samples for our other analyses.

Annotations and gene selection
In non-model organisms, lack of knowledge of expected cell types, absence of extensive gene characterization, and few established cell markers, makes cell type annotation challenging. Prior to analysis and annotation, we contacted an international group of mosquito experts to solicit hypotheses about putative cell types, as well as potential cell markers or genes of interest. *Aedes aegypti* genes came from sources including previous mosquito literature and previous bioinformatics analyses assessing putative function or gene families from the AaegL5 genome.

Gene orthology to Drosophila melanogaster: In addition to information collected from the *Aedes aegypti* Mosquito Cell Atlas Consortium, we used information from homologues in *Drosophila melanogaster* that have been better-characterized. Orthologous genes were assessed using Ensembl Metazoa BioMart database (Ensembl Genomes release 56[56], BLAST (nucleotide or protein)[57], or VectorBase[58]. We also used curated and computed cell marker genes from the Fly Cell Atlas[24]. It is important to note that *Aedes aegypti* and *Drosophila melanogaster* are separated by 260 million years since their last common ancestor[59,61], with distinct behaviors, life cycles and physiology, so relying on *Drosophila melanogaster* homology to interpret *Aedes aegypti* genes can be problematic.

For instance, in a comparative genomic study of *Drosophila melanogaster* and several mosquito species of developmental genes, while many were well-conserved, key developmental genes in *Drosophila melanogaster* (as well as other insects) were not identified in mosquito genomes[59]. The fibroblast growth factor (FGF) signaling pathway

involved in many biological processes including cell differentiation and migration, is conserved between flies and vertebrates, but was not identified in mosquito species. Additionally, cases were also observed of increased copy numbers of developmental genes in mosquitoes. How these individual copies differ from their homolog in *Drosophila melanogaster* is not known. While some genes and pathways are conserved, divergence in gene function and expression patterns is also expected, which can easily lead to misinterpretation and errors in analysis if one relies too heavily on *Drosophila melanogaster* to benchmark discoveries in *Aedes aegypti*.

Gene marker selection: Genes were selected based on *sc.tl.rank_genes_groups* and MAST on Louvain or Leiden algorithm clustering[54,55]. Top computed marker genes for each cluster were each assessed visually (UMAP) and by comparing average gene expression across all clusters in the data object. Genes were manually selected based on their ability to confer information of cell type, orthology to known *Drosophila melanogaster* marker genes, and their distinctiveness as a marker gene across cell types in all datasets. For instance, the transcription factor *Sox100B* (*AAEL009473*) was used as a marker and commonly observed in sensory tissues. Recent work identifying these cells in *Drosophila melanogaster* tarsi suggests that *Sox100B*-expressing cells may be important for neural lamella formation[145].

Computed gene markers for Louvain or Leiden algorithms used for annotations using *rank_genes_groups* (integrated data object of all sugar-fed cells) and MAST (all other tissues) are available on Zenodo Supplemental Data. Computed gene markers on manual annotations for all tissues using *rank_genes_groups* are available on UCSC Cell Browser and Zenodo Supplemental Data.

Annotation using gene markers: Annotations were performed using a combination of semi-automated and manual methods. Principal annotations were performed on each tissue (Figures 2, 3, 7, S4-S13, S18, and S21-S22) and on the integrated data object of all sugar-fed cells (Figure 1). Preliminary annotations were performed on each sample individually before merging all samples of each tissue (Table S1). Data were clustered using Louvain or Leiden algorithms and clusters were assigned cell type annotations. Clustering resolution was set based on cellular complexity of tissue and amount of prior information on tissue cell types (Table S2). Clusters were assessed for mean expression of identified gene markers using outputs from MAST, UMAPs, heatmaps, violin plots and bar plots (Zenodo Supplemental Data). Clusters were assigned a cell type annotation based on expression of thresholded gene markers or combinations of gene markers (Table S4, for annotation script see Zenodo Supplemental Data). Gene markers for each cell type were also assigned a threshold through assessment of mean expression levels across clusters (Table S4).

Sensory neuron annotations: *nompC*-negative sensory neuron populations in the antenna, maxillary palps, tarsi and proboscis were annotated separately in a similar pattern to tissues (Figures 5, 6, and S24-S25). We used the same combination of semi-automated and manual methods as described above, however for these populations, we attributed extra significance to a list of putative sensory genes that

might affect the stimulus response profile of a given cell type (Table S4). Clusters were computed with the Leiden algorithm, at high resolution due to sensory neuron complexity (Table S2). Clusters were assigned a cell type annotation. Cell types were named for chemoreceptors uniquely expressed in a cell type.

In the antenna, despite separating clusters at high resolution (Leiden, resolution 10), we found at least 6 examples of chemoreceptor genes co-expressed within a cluster but not within the same cells - indicating mutual exclusivity - and could not be separated via clustering algorithms. This suggests that these cells may belong to distinct, but transcriptomically similar olfactory sensory neuron cell types (for instance, *Ir41b* and *Ir41*e in Figures 5C-5D, S20B, and Zenodo Supplemental Data).

Sensory neuron analysis

For the antennae, maxillary palps, and proboscis samples, we subsetted and filtered *nompC*-negative sensory neurons for further analysis. We identified the neuronal population based on the expression of *Syt1* (*AAEL000704*), *brp* (*AAEL018153*), *nSyb* (*AAEL024921*) and *CadN* (*AAEL000597*) (Figures 5A, S23A and S24A). We excluded mechanosensory neurons based on the expression of the *Drosophila melanogaster* orthologue of mechanosensory receptor *nompC* (*AAEL019818*) (Figures S19A-S19B). We removed clusters with a high doublet score (Figures S19C-S19D). Before reclustering, we additionally removed individual nuclei with a doublet score above 0.15 (Figure S19H). This ensured a conservative filtering of potential doublets given our interest in possible co-expression of receptor genes. For the antenna, we also filtered on neuronal gene fraction to ensure we were only looking at high quality neuronal nuclei (Figure S19E), although we note that this step removed *Gr20* cells from our analysis (cluster 83, Figures S18B, S19A, S19C, S19G and S19R). For wing and abdominal tip neuron subsetting, all neurons were included for assessment of putative sensory gene expression (Zenodo Supplemental Data). As with other tissues, we removed individual nuclei with a doublet score above 0.15 (Figure S19H).

Cell type comparison across conditions/sexes

Cell abundance comparison: For the sexual cell type abundance difference, the frequencies of each cell type in each tissue for both sexes were determined by calculating the proportion of each cell type relative to the total number of cells in the tissue. The sexual abundance difference index for each cell type in each tissue was calculated using the following equation (Figures S4-S12, S18, S21-S22, scripts in Zenodo Supplemental Data):

$$abundance\ index = \frac{Frequency\ (female) - Frequency\ (male)}{Frequency\ (female) + Frequency\ (male)}$$

Sexual abundance difference index: Where cell type was categorized based on abundance difference across sexes, cells were considered “Female biased” if abundance index > 0.3; “Neutral” if abundance index was -0.3 to 0.3, inclusive; “Male biased” if abundance index < -0.3. In bar plots, if there are biological replicates, the value for each replicate was shown as dots, and the standard error was calculated.

Differentially expressed genes: MAST was used to calculate the differentially expressed genes for cell type annotation, across sexes, and blood-feeding conditions for each cell type[55]. Log fold change is represented by MAST coefficients *(coef)*.

For counting significantly differentially expressed genes in Figures 7, 8 and S26C, MAST output files were thresholded for absolute value of *coef* above 1, and a false discovery rate of 0.05. *coef* was calculated from normalized expression (natural log). We only analyzed cell types with at least 10 cells in all conditions. In some cases, MAST *coef* could not be calculated for some genes due to their normalized-log expression being zero or close to zero in at least one of the conditions (NaN genes). NaN genes were included in differentially expressed gene counts (bar plots) if they were expressed in greater than 10% of genes in at least one condition and had normalized expression value greater than 1 (Tables S5, S6, S9, S10, and Zenodo Supplemental Data). Most NaN genes did not meet this criteria and were discarded. No NaN genes met this criteria for generation of volcano plots (Figures 6, 7 and S27). NaN genes were left grey for log fold change heatmaps (Figures 8 and S29).

For male versus female differential gene expression analysis across annotated cell types in Figures S4-S12, S18 and S21-S22, genes were discarded prior to analysis if they were not expressed in at least 10% of cells in each sex within each cell type. differentially expressed gene counts were determined by genes that were |*coef*/log(2)| > 1 and a false discovery rate < 0.05.

Volcano plots, log fold change heatmaps: Volcano plots and log fold change heatmaps on differentially expressed genes were made using MAST differentially expressed genes. Log fold change is represented by MAST coefficients *(coef)*. Volcano plots were made with *seaborn.scatterplot* on $-\log_{10}$(false discovery rate)[200]. Log fold change heatmaps using *seaborn.heatmap* on individual genes were made by identifying all clusters where the gene had a calculated false discovery rate < 0.05 in at least one timepoint. Heatmaps were sorted by sum of *coef* values. Only clusters that had more than 10 cells in each timepoint were included.

Data visualization

UMAPs, Gene fraction visualization: UMAP coordinates were created using *scanpy tl.umap* function on the constructed nearest neighbors graph (described above). The *min_dist* parameter used are described in Table S2. We visualized UMAPs using *sc.pl.umap* function.

We quantify gene signature expression by computing gene fraction defined as: np.asarray(np.sum(adata.X[:, genelist_indices], axis = 1)/np.sum(adata.X, axis = 1)).squeeze() * 100) and visualized on UMAP. This is the mRNA content represented by the genes in the list for a given cell as a fraction of total mRNA of the cell.

Dotplots and heatmaps: Clusters for dotplots and heatmaps were organized using *sc.tl.dendrogram, sc.tl.heatmap* functions followed by *sc.pl.dendrogram* or *sc.pl.heatmap* functions on selected genes. Heatmaps were visualized using seaborn *sn.heatmap*[200]. Full heatmaps of all putative sensory genes expressed in selected

sensory neurons are available in Zenodo Supplemental Data, in addition to wing and abdominal tip datasets. For neuropeptide-related gene heatmaps, genes were identified from literature and *Drosophila melanogaster* orthology, as previously described[56,214,215]. Genes were considered expressed by a cell type if they had a normalized expression value of at least 1 and were expressed by at least 20 percent of all cells in that cluster.

Violin plots, stacked bar plots, box plots: Violin plots were made using *sc.pl.violin* or *sc.pl.stacked_violin*. Proportion stacked bar plots were made using *matplotlib ax.bar*. Boxplots made with *seaborn.boxplot* and *seaborn.stripplot*.

Diffusion component & cluster distance analysis:
To quantify the transcriptomic difference between male *ppk317* and other antenna cell types, we applied diffusion components analysis (Figures S17E-S17F) using *sc.tl.diffmap*, with 80 diffusion components using the nearest neighbors graph (described above). Diffusion components have been widely used in single-cell data analysis to approximate phenotypic distances between subpopulations of cells[216–220]. Because the top diffusion components explain the most variance in the data[218,219], we calculated the top correlating gene for the diffusion components 1 and 2 (Zenodo Supplemental Data). *ppk317* (*AAEL000873*) was the highest scoring gene of diffusion component 1 (|correlation score| > 0.89) (Figure S17E, first panel). Neuronal markers including *Syt1 (AAEL000704)* and *nSyb* (*AAEL024921*) ranked highly for diffusion component 2 (for both a |correlation score| > 0.72) (Figure S17E, second panel). We then selected top components based on eigengap as has been done previously[218,219]. We observed that the first major gap in eigenvalues occurred between 18th and 19th eigenvalues, as such we chose top 18 eigenvectors for further analysis: Eigenvalues 1 through 18. Partition-based graph abstraction (*sc.tl.paga*) was then made through recalculating nearest neighbors using thus computed diffusion components (Figure S17F). For boxplot in Figure S17J, pairwise Euclidean distances were computed to approximate phenotypic distance based on diffusion embeddings using *sklearn.metrics.pairwise_distances* [221] and plotted with *matplotlib.boxplot*.

Correlation matrix heatmap: To evaluate pairwise correlation of gene expression between clusters in Figure S17G, we computed the Pearson correlation coefficient matrix (*numpy.corrcoef*) between normalized gene expression matrices for every pair of clusters. We computed correlation between every pair of cells for every pair of clusters and reported the mean correlation value as a heatmap. Diagonal values (cluster to itself) represent intra-cluster correlation values, which vary based on features such as cell number and gene heterogeneity.

Raw counts scatterplot: To generate the scatter plot on antenna olfactory sensory neurons in Figure S20C, raw transcript counts (unique molecular identifiers) for a list of putative sensory genes (Table S4) were counted and plotted for each sample using *matplotlib.scatter*.

Cross-species comparison

For comparison of the *Aedes aegypti* Mosquito Cell Atlas brain to the fly cell atlas (FCA) head data, we used SAMap (v1.0.15[156]). SAMap was used according to documentation. All versus all NCBI BLAST (v2.9.0[57]) was run using the SAMap script map_genes.sh on the annotated proteins from the VectorBase-58 version of LVP_AGWG genome and the "all translation" file from the FB2023_02 version of the FlyBase genome. Analyses were performed on the FCA head dataset[24] and the *Aedes aegypti* Mosquito Cell Atlas all brain dataset. These datasets were subsetted into neurons and glia and abundant cell clusters were subsampled using scanpy. The FCA head dataset was subsetted using the FCA cell type annotation clusters. Clusters with mean expression of the gene *Dm_repo* >0.4 were considered glia and mean expression of *Dm_nSyb* >1.2 were considered neurons. Then cell clusters of neurons (Leiden algorithm, resolution = 4) with >1000 cells were subsampled down to 1000 using *scanpy.subsample*. The *Aedes aegypti* Mosquito Cell Atlas brain dataset was subsetted using the Leiden algorithm (resolution = 5) clusters. Clusters with mean expression of the gene *repo (AAEL027131)* >2.0 were considered glia and mean expression of *nSyb (AAEL024921)* >0.7 were considered neurons. Neurons clusters with >1000 cells were subsampled down to 1000 using the subsample function in Scanpy. Subsampled neurons and all glia were then run in SAMap using default parameters. FCA and *Aedes aegypti* Mosquito Cell Atlas neurons were run together, FCA and *Aedes aegypti* Mosquito Cell Atlas glia were run together, and as a control FCA glia and *Aedes aegypti* Mosquito Cell Atlas neurons were run together (Figures S28E-S28K). Mapping scores were determined between FCA cell type annotations and *Aedes aegypti* Mosquito Cell Atlas (Leiden, resolution = 5) clusters. Kenyon cells (KCs) were identified in the *Aedes aegypti* Mosquito Cell Atlas dataset by high mapping scores with the FCA KCs and expression of the known markers including *Hr51 (AAEL020847)* and *sNPF (AAEL019691)* (Figures S28L and S28M). We also queried markers for potential Kenyon cell subtypes in the *Aedes aegypti* Mosquito Cell Atlas using *Pde8* (*AAEL019528*) (alpha/beta KCs), *mamo* (*AAEL019481*) (alpha'/beta' KCs) and *Imp1* (*AAEL006876*) (gamma KCs) (Figures S28N-S28P)[24,158].

References

1. World Health Organization ed. World malaria report 2024.
2. Disease Outbreak News; Dengue - Global Situation (2024).
3. Kraemer, M.U.G., Reiner, R.C., Brady, O.J., Messina, J.P., Gilbert, M., Pigott, D.M., Yi, D., Johnson, K., Earl, L., Marczak, L.B., et al. (2019). Past and future spread of the arbovirus vectors Aedes aegypti and Aedes albopictus. Nat. Microbiol. *4*, 854–863.
4. Gubler, D.J. (2009). Vector-borne diseases. Rev. Sci. Tech. *28*, 583–588.
5. Souza-Neto, J.A., Powell, J.R., and Bonizzoni, M. (2019). Aedes aegypti vector competence studies: A review. Infect. Genet. Evol. *67*, 191–209.
6. Wang, G.-H., Hoffmann, A., and Champer, J. (2025). Gene drive and symbiont technologies for control of mosquito-borne diseases. Annu. Rev. Entomol. *70*, 229–249.

7. Bernier, U.R., Kline, D.L., Barnard, D.R., Schreck, C.E., and Yost, R.A. (2000). Analysis of human skin emanations by gas chromatography/mass spectrometry. 2. Identification of volatile compounds that are candidate attractants for the yellow fever mosquito (Aedes aegypti). Anal. Chem. *72*, 747–756.
8. McMeniman, C.J., Corfas, R.A., Matthews, B.J., Ritchie, S.A., and Vosshall, L.B. (2014). Multimodal integration of carbon dioxide and other sensory cues drives mosquito attraction to humans. Cell *156*, 1060–1071.
9. De Obaldia, M.E., Morita, T., Dedmon, L.C., Boehmler, D.J., Jiang, C.S., Zeledon, E.V., Cross, J.R., and Vosshall, L.B. (2022). Differential mosquito attraction to humans is associated with skin-derived carboxylic acid levels. Cell *185*, 4099–4116.e13.
10. Morita, T., Lyn, N.G., von Heynitz, R.K., Goldman, O.V., Sorrells, T.R., DeGennaro, M., Matthews, B.J., Houri-Zeevi, L., and Vosshall, L.B. (2025). Cross-modal sensory compensation increases mosquito attraction to humans. Sci. Adv. *11*, eadn5758.
11. Brown, J.E., Evans, B.R., Zheng, W., Obas, V., Barrera-Martinez, L., Egizi, A., Zhao, H., Caccone, A., and Powell, J.R. (2014). Human impacts have shaped historical and recent evolution in Aedes aegypti, the dengue and yellow fever mosquito. Evolution *68*, 514–525.
12. McBride, C.S., Baier, F., Omondi, A.B., Spitzer, S.A., Lutomiah, J., Sang, R., Ignell, R., and Vosshall, L.B. (2014). Evolution of mosquito preference for humans linked to an odorant receptor. Nature *515*, 222–227.
13. Klowden, M.J., and Lea, A.O. (1978). Blood meal size as a factor affecting continued host-seeking by Aedes aegypti (L.). Am. J. Trop. Med. Hyg. *27*, 827–831.
14. Klowden, M.J., and Lea, A.O. (1979). Humoral inhibition of host-seeking in Aedes aegypti during oöcyte maturation. J. Insect Physiol. *25*, 231–235.
15. Klowden, M.J., and Lea, A.O. (1979). Abdominal distention terminates subsequent host-seeking behaviour of Aedes aegypti following a blood meal. J. Insect Physiol. *25*, 583–585.
16. Liesch, J., Bellani, L.L., and Vosshall, L.B. (2013). Functional and genetic characterization of neuropeptide Y-like receptors in Aedes aegypti. PLoS Negl. Trop. Dis. *7*, e2486.
17. Duvall, L.B., Ramos-Espiritu, L., Barsoum, K.E., Glickman, J.F., and Vosshall, L.B. (2019). Small-Molecule Agonists of Ae. aegypti Neuropeptide Y Receptor Block Mosquito Biting. Cell *176*, 687–701.e5.
18. Cao, J., Packer, J.S., Ramani, V., Cusanovich, D.A., Huynh, C., Daza, R., Qiu, X., Lee, C., Furlan, S.N., Steemers, F.J., et al. (2017). Comprehensive single-cell transcriptional profiling of a multicellular organism. Science *357*, 661–667.
19. Gao, S.M., Qi, Y., Zhang, Q., Guan, Y., Lee, Y.-T., Ding, L., Wang, L., Mohammed, A.S., Li, H., Fu, Y., et al. (2024). Aging atlas reveals cell-type-specific effects of pro-longevity strategies. Nat. Aging *4*, 998–1013.
20. Fincher, C.T., Wurtzel, O., de Hoog, T., Kravarik, K.M., and Reddien, P.W. (2018). Cell type transcriptome atlas for the planarian Schmidtea mediterranea. Science *360*, eaaq1736.
21. Tabula Muris Consortium, Overall coordination, Logistical coordination, Organ collection and processing, Library preparation and sequencing, Computational data

analysis, Cell type annotation, Writing group, Supplemental text writing group, and Principal investigators (2018). Single-cell transcriptomics of 20 mouse organs creates a Tabula Muris. Nature *562*, 367–372.
22. Tabula Muris Consortium (2020). A single-cell transcriptomic atlas characterizes ageing tissues in the mouse. Nature *583*, 590–595.
23. The Tabula Microcebus Consortium, Ezran, C., Liu, S., Chang, S., Ming, J., Botvinnik, O., Penland, L., Tarashansky, A., de Morree, A., Travaglini, K.J., et al. (2021). Tabula Microcebus: A transcriptomic cell atlas of mouse lemur, an emerging primate model organism. bioRxiv. https://doi.org/10.1101/2021.12.12.469460.
24. Li, H., Janssens, J., De Waegeneer, M., Kolluru, S.S., Davie, K., Gardeux, V., Saelens, W., David, F.P.A., Brbić, M., Spanier, K., et al. (2022). Fly Cell Atlas: A single-nucleus transcriptomic atlas of the adult fruit fly. Science *375*, eabk2432.
25. Bohbot, J., Pitts, R.J., Kwon, H.-W., Rützler, M., Robertson, H.M., and Zwiebel, L.J. (2007). Molecular characterization of the Aedes aegypti odorant receptor gene family. Insect Mol. Biol. *16*, 525–537.
26. Matthews, B.J., McBride, C.S., DeGennaro, M., Despo, O., and Vosshall, L.B. (2016). The neurotranscriptome of the Aedes aegypti mosquito. BMC Genomics *17*, 32.
27. Sparks, J.T., and Dickens, J.C. (2014). Physiological recordings and RNA sequencing of the gustatory appendages of the yellow-fever mosquito Aedes aegypti. J. Vis. Exp., 52088.
28. Hixson, B., Bing, X.-L., Yang, X., Bonfini, A., Nagy, P., and Buchon, N. (2022). A transcriptomic atlas of Aedes aegypti reveals detailed functional organization of major body parts and gut regional specializations in sugar-fed and blood-fed adult females. Elife *11*, e76132.
29. Venkataraman, K., Shai, N., Lakhiani, P., Zylka, S., Zhao, J., Herre, M., Zeng, J., Neal, L.A., Molina, H., Zhao, L., et al. (2023). Two novel, tightly linked, and rapidly evolving genes underlie Aedes aegypti mosquito reproductive resilience during drought. Elife *12*, e80489.
30. Jové, V., Gong, Z., Hol, F.J.H., Zhao, Z., Sorrells, T.R., Carroll, T.S., Prakash, M., McBride, C.S., and Vosshall, L.B. (2020). Sensory Discrimination of Blood and Floral Nectar by Aedes aegypti Mosquitoes. Neuron *108*, 1163–1180.e12.
31. Li, Y., Piermarini, P.M., Esquivel, C.J., Price, D.P., Drumm, H.E., Schilkey, F.D., and Hansen, I.A. (2017). RNA-Seq Comparison of Larval and Adult Malpighian Tubules of the Yellow Fever Mosquito Aedes aegypti Reveals Life Stage-Specific Changes in Renal Function. Front. Physiol. *8*, 283.
32. Cui, Y., and Franz, A.W.E. (2020). Heterogeneity of midgut cells and their differential responses to blood meal ingestion by the mosquito, Aedes aegypti. Insect Biochem. Mol. Biol. *127*, 103496.
33. Chen, T.-Y., Raduwan, H., Marín-López, A., Cui, Y., and Fikrig, E. (2024). Zika virus exists in enterocytes and enteroendocrine cells of the Aedes aegypti midgut. iScience *27*, 110353.
34. Wang, S., Huang, Y., Wang, F., Han, Q., Ren, N., Wang, X., Cui, Y., Yuan, Z., and Xia, H. (2024). A cell atlas of the adult female Aedes aegypti midgut revealed by single-cell RNA sequencing. Sci. Data *11*, 587.
35. Vial, T., Lopez-Maestre, H., Couderc, E., Pinaud, S., Howick, V., Akorli, J.,

Lawniczak, M., Marti, G., and Merkling, S.H. (2024). Single-cell transcriptional landscapes of*Aedes aegypti*midgut and fat body after a bloodmeal. bioRxiv. https://doi.org/10.1101/2024.11.08.622039.
36. Herre, M., Goldman, O.V., Lu, T.-C., Caballero-Vidal, G., Qi, Y., Gilbert, Z.N., Gong, Z., Morita, T., Rahiel, S., Ghaninia, M., et al. (2022). Non-canonical odor coding in the mosquito. Cell *185*, 3104–3123.e28.
37. Adavi, E.D., Dos Anjos, V.L., Kotb, S., Metz, H.C., Tian, D., Zhao, Z., Zung, J.L., Rose, N.H., and McBride, C.S. (2024). Olfactory receptor coexpression and co-option in the dengue mosquito. Preprint at Neuroscience, https://doi.org/10.1101/2024.08.21.608847 https://doi.org/10.1101/2024.08.21.608847.
38. Cui, Y., Behura, S.K., and Franz, A.W.E. (2022). Cellular diversity and gene expression profiles in the male and female brain of Aedes aegypti. BMC Genomics *23*, 119.
39. Yin, C., Morita, T., and Parrish, J.Z. (2024). A cell atlas of the larval Aedes aegypti ventral nerve cord. Neural Dev. *19*, 2.
40. Page, N., Taxiarchi, C., Tonge, D., Kuburic, J., Chesters, E., Kriezis, A., Kyrou, K., Game, L., Nolan, T., and Galizi, R. (2023). Single-cell profiling of Anopheles gambiae spermatogenesis defines the onset of meiotic silencing and premeiotic overexpression of the X chromosome. Commun. Biol. *6*, 850.
41. Taxiarchi, C., Kranjc, N., Kriezis, A., Kyrou, K., Bernardini, F., Russell, S., Nolan, T., Crisanti, A., and Galizi, R. (2019). High-resolution transcriptional profiling of Anopheles gambiae spermatogenesis reveals mechanisms of sex chromosome regulation. Sci. Rep. *9*, 14841.
42. Raddi, G., Barletta, A.B.F., Efremova, M., Ramirez, J.L., Cantera, R., Teichmann, S.A., Barillas-Mury, C., and Billker, O. (2020). Mosquito cellular immunity at single-cell resolution. Science *369*, 1128–1132.
43. Saha, B., McNinch, C.M., Lu, S., Ho, M.C.W., De Carvalho, S.S., and Barillas-Mury, C. (2024). In-depth transcriptomic analysis of Anopheles gambiae hemocytes uncovers novel genes and the oenocytoid developmental lineage. BMC Genomics *25*, 80.
44. Fitzmeyer, E.A., Dutt, T.S., Pinaud, S., Graham, B., Gallichotte, E.N., Hill, J.L., Campbell, C.L., Ogg, H., Howick, V., Lawniczak, M.K.N., et al. (2025). A single-cell atlas of the Culex tarsalis midgut during West Nile virus infection. PLoS Pathog. *21*, e1012855.
45. Soghigian, J., Sither, C., Justi, S.A., Morinaga, G., Cassel, B.K., Vitek, C.J., Livdahl, T., Xia, S., Gloria-Soria, A., Powell, J.R., et al. (2023). Phylogenomics reveals the history of host use in mosquitoes. Nat. Commun. *14*, 6252.
46. Elmentaite, R., Domínguez Conde, C., Yang, L., and Teichmann, S.A. (2022). Single-cell atlases: shared and tissue-specific cell types across human organs. Nat. Rev. Genet. *23*, 395–410.
47. Martin, B.K., Qiu, C., Nichols, E., Phung, M., Green-Gladden, R., Srivatsan, S., Blecher-Gonen, R., Beliveau, B.J., Trapnell, C., Cao, J., et al. (2023). Optimized single-nucleus transcriptional profiling by combinatorial indexing. Nat. Protoc. *18*, 188–207.
48. Lu, T.-C., Brbić, M., Park, Y.-J., Jackson, T., Chen, J., Kolluru, S.S., Qi, Y.,

Katheder, N.S., Cai, X.T., Lee, S., et al. (2023). Aging Fly Cell Atlas identifies exhaustive aging features at cellular resolution. Science *380*, eadg0934.
49. Rinker, D.C., Pitts, R.J., Zhou, X., Suh, E., Rokas, A., and Zwiebel, L.J. (2013). Blood meal-induced changes to antennal transcriptome profiles reveal shifts in odor sensitivities in Anopheles gambiae. Proc. Natl. Acad. Sci. U. S. A. *110*, 8260–8265.
50. Fox, A.N., Pitts, R.J., Robertson, H.M., Carlson, J.R., and Zwiebel, L.J. (2001). Candidate odorant receptors from the malaria vector mosquito Anopheles gambiae and evidence of down-regulation in response to blood feeding. Proc. Natl. Acad. Sci. U. S. A. *98*, 14693–14697.
51. Qiu, Y.-T., Gort, G., Torricelli, R., Takken, W., and van Loon, J.J.A. (2013). Effects of blood-feeding on olfactory sensitivity of the malaria mosquito Anopheles gambiae: application of mixed linear models to account for repeated measurements. J. Insect Physiol. *59*, 1111–1118.
52. Siju, K.P., Hill, S.R., Hansson, B.S., and Ignell, R. (2010). Influence of blood meal on the responsiveness of olfactory receptor neurons in antennal sensilla trichodea of the yellow fever mosquito, Aedes aegypti. J. Insect Physiol. *56*, 659–665.
53. Matthews, B.J., Dudchenko, O., Kingan, S.B., Koren, S., Antoshechkin, I., Crawford, J.E., Glassford, W.J., Herre, M., Redmond, S.N., Rose, N.H., et al. (2018). Improved reference genome of Aedes aegypti informs arbovirus vector control. Nature *563*, 501–507.
54. Wolf, F.A., Angerer, P., and Theis, F.J. (2018). SCANPY: large-scale single-cell gene expression data analysis. Genome Biol. *19*, 15.
55. Finak, G., McDavid, A., Yajima, M., Deng, J., Gersuk, V., Shalek, A.K., Slichter, C.K., Miller, H.W., McElrath, M.J., Prlic, M., et al. (2015). MAST: a flexible statistical framework for assessing transcriptional changes and characterizing heterogeneity in single-cell RNA sequencing data. Genome Biol. *16*, 278.
56. Cunningham, F., Allen, J.E., Allen, J., Alvarez-Jarreta, J., Amode, M.R., Armean, I.M., Austine-Orimoloye, O., Azov, A.G., Barnes, I., Bennett, R., et al. (2022). Ensembl 2022. Nucleic Acids Res. *50*, D988–D995.
57. Altschul, S.F., Gish, W., Miller, W., Myers, E.W., and Lipman, D.J. (1990). Basic local alignment search tool. J. Mol. Biol. *215*, 403–410.
58. Giraldo-Calderón, G.I., Harb, O.S., Kelly, S.A., Rund, S.S., Roos, D.S., and McDowell, M.A. (2022). VectorBase.org updates: bioinformatic resources for invertebrate vectors of human pathogens and related organisms. Curr. Opin. Insect Sci. *50*, 100860.
59. Behura, S.K., Haugen, M., Flannery, E., Sarro, J., Tessier, C.R., Severson, D.W., and Duman-Scheel, M. (2011). Comparative genomic analysis of Drosophila melanogaster and vector mosquito developmental genes. PLoS One *6*, e21504.
60. da Silva, A.F., Machado, L.C., de Paula, M.B., da Silva Pessoa Vieira, C.J., de Morais Bronzoni, R.V., de Melo Santos, M.A.V., and Wallau, G.L. (2020). Culicidae evolutionary history focusing on the Culicinae subfamily based on mitochondrial phylogenomics. Sci. Rep. *10*, 18823.
61. Arensburger, P., Megy, K., Waterhouse, R.M., Abrudan, J., Amedeo, P., Antelo, B., Bartholomay, L., Bidwell, S., Caler, E., Camara, F., et al. (2010). Sequencing of Culex quinquefasciatus establishes a platform for mosquito comparative genomics. Science *330*, 86–88.

62. Wang, S., and Samakovlis, C. (2012). Grainy head and its target genes in epithelial morphogenesis and wound healing. Curr. Top. Dev. Biol. *98*, 35–63.
63. Bray, S.J., and Kafatos, F.C. (1991). Developmental function of Elf-1: an essential transcription factor during embryogenesis in Drosophila. Genes Dev. *5*, 1672–1683.
64. Zuber, R., Norum, M., Wang, Y., Oehl, K., Gehring, N., Accardi, D., Bartozsewski, S., Berger, J., Flötenmeyer, M., and Moussian, B. (2018). The ABC transporter Snu and the extracellular protein Snsl cooperate in the formation of the lipid-based inward and outward barrier in the skin of Drosophila. Eur. J. Cell Biol. *97*, 90–101.
65. Corthals, K., Andersson, V., Churcher, A., Reimegård, J., and Enjin, A. (2023). Genetic atlas of hygro-and thermosensory cells in the vinegar fly Drosophila melanogaster. Sci. Rep. *13*, 15202.
66. Speir, M.L., Bhaduri, A., Markov, N.S., Moreno, P., Nowakowski, T.J., Papatheodorou, I., Pollen, A.A., Raney, B.J., Seninge, L., Kent, W.J., et al. (2021). UCSC Cell Browser: visualize your single-cell data. Bioinformatics *37*, 4578–4580.
67. Zheng, G.X.Y., Terry, J.M., Belgrader, P., Ryvkin, P., Bent, Z.W., Wilson, R., Ziraldo, S.B., Wheeler, T.D., McDermott, G.P., Zhu, J., et al. (2017). Massively parallel digital transcriptional profiling of single cells. Nat. Commun. *8*, 14049.
68. Fleming, S.J., Chaffin, M.D., Arduini, A., Akkad, A.-D., Banks, E., Marioni, J.C., Philippakis, A.A., Ellinor, P.T., and Babadi, M. (2023). Unsupervised removal of systematic background noise from droplet-based single-cell experiments using CellBender. Nat. Methods *20*, 1323–1335.
69. Shibata, N., Umesono, Y., Orii, H., Sakurai, T., Watanabe, K., and Agata, K. (1999). Expression of vasa(vas)-related genes in germline cells and totipotent somatic stem cells of planarians. Dev. Biol. *206*, 73–87.
70. Olivieri, G., and Olivieri, A. (1965). Autoradiographic study of nucleic acid synthesis during spermatogenesis in Drosophila melanogaster. Mutat. Res. *2*, 366–380.
71. Raz, A.A., Vida, G.S., Stern, S.R., Mahadevaraju, S., Fingerhut, J.M., Viveiros, J.M., Pal, S., Grey, J.R., Grace, M.R., Berry, C.W., et al. (2023). Emergent dynamics of adult stem cell lineages from single nucleus and single cell RNA-Seq of Drosophila testes. Elife *12*, e82201.
72. Sun, X., Wang, X., Shi, K., Lyu, X., Sun, J., Raikhel, A.S., and Zou, Z. (2024). Leucine aminopeptidase1 controls egg deposition and hatchability in male Aedes aegypti mosquitoes. Nat. Commun. *15*, 106.
73. Pitts, R.J., Liu, C., Zhou, X., Malpartida, J.C., and Zwiebel, L.J. (2014). Odorant receptor-mediated sperm activation in disease vector mosquitoes. Proc. Natl. Acad. Sci. U. S. A. *111*, 2566–2571.
74. Miyamoto, T., and Amrein, H. (2014). Diverse roles for the Drosophila fructose sensor Gr43a. Fly (Austin) *8*, 19–25.
75. Depetris-Chauvin, A., Galagovsky, D., and Grosjean, Y. (2015). Chemicals and chemoreceptors: ecologically relevant signals driving behavior in Drosophila. Front. Ecol. Evol. *3*. https://doi.org/10.3389/fevo.2015.00041.
76. Zhang, S., Gu, Q., Li, Y., Li, Y., Li, M., Li, D., and He, N. (2025). An amino acid-tuned gustatory receptor relatively abundant in the silkworm gut is crucial for growth and development. Pest Manag. Sci. https://doi.org/10.1002/ps.8783.
77. Raad, H., Ferveur, J.-F., Ledger, N., Capovilla, M., and Robichon, A. (2016). Functional gustatory role of chemoreceptors in Drosophila wings. Cell Rep. *15*,

1442–1454.
78. David, O.G., Sanchez, K.M., Arce, A.V., Costa-da-Silva, A.L., Bellantuono, A.J., and DeGennaro, M. (2023). Fertility decline in female mosquitoes is regulated by the orco olfactory co-receptor. iScience *26*, 106883.
79. Smith, R.C., Walter, M.F., Hice, R.H., O'Brochta, D.A., and Atkinson, P.W. (2007). Testis-specific expression of the beta2 tubulin promoter of Aedes aegypti and its application as a genetic sex-separation marker. Insect Mol. Biol. *16*, 61–71.
80. Kemphues, K.J., Kaufman, T.C., Raff, R.A., and Raff, E.C. (1982). The testis-specific beta-tubulin subunit in Drosophila melanogaster has multiple functions in spermatogenesis. Cell *31*, 655–670.
81. Fabrizio, J.J., Boyle, M., and DiNardo, S. (2003). A somatic role for eyes absent (eya) and sine oculis (so) in Drosophila spermatocyte development. Dev. Biol. *258*, 117–128.
82. Martin-Martin, I., Smith, L.B., Chagas, A.C., Sá-Nunes, A., Shrivastava, G., Valenzuela-Leon, P.C., and Calvo, E. (2020). Aedes albopictus D7 Salivary Protein Prevents Host Hemostasis and Inflammation. Biomolecules *10*, 1372.
83. Wang, Z.-Y., Nie, K.-X., Niu, J.-C., and Cheng, G. (2024). Research progress toward the influence of mosquito salivary proteins on the transmission of mosquito-borne viruses. Insect Sci. *31*, 663–673.
84. Visser, I., Koenraadt, C.J.M., Koopmans, M.P.G., and Rockx, B. (2023). The significance of mosquito saliva in arbovirus transmission and pathogenesis in the vertebrate host. One Health *16*, 100506.
85. Spencer Clinton, J.L., Vogt, M.B., Kneubehl, A.R., Hibl, B.M., Paust, S., and Rico-Hesse, R. (2023). Sialokinin in mosquito saliva shifts human immune responses towards intracellular pathogens. PLoS Negl. Trop. Dis. *17*, e0011095.
86. Guerrero, D., Cantaert, T., and Missé, D. (2020). Aedes Mosquito Salivary Components and Their Effect on the Immune Response to Arboviruses. Front. Cell. Infect. Microbiol. *10*, 407.
87. Guerrero, D., Vo, H.T.M., Lon, C., Bohl, J.A., Nhik, S., Chea, S., Man, S., Sreng, S., Pacheco, A.R., Ly, S., et al. (2022). Evaluation of cutaneous immune response in a controlled human in vivo model of mosquito bites. Nat. Commun. *13*, 7036.
88. Gavor, E., Choong, Y.K., Liu, Y., Pompon, J., Ooi, E.E., Mok, Y.K., Liu, H., Kini, R.M., and Sivaraman, J. (2022). Identification of Aedes aegypti salivary gland proteins interacting with human immune receptor proteins. PLoS Negl. Trop. Dis. *16*, e0010743.
89. Sri-In, C., Weng, S.-C., Shiao, S.-H., and Tu, W.-C. (2020). A simplified method for blood feeding, oral infection, and saliva collection of the dengue vector mosquitoes. PLoS One *15*, e0233618.
90. Vogt, M.B., Lahon, A., Arya, R.P., Kneubehl, A.R., Spencer Clinton, J.L., Paust, S., and Rico-Hesse, R. (2018). Mosquito saliva alone has profound effects on the human immune system. PLoS Negl. Trop. Dis. *12*, e0006439.
91. Ribeiro, J.M.C., and Francischetti, I.M.B. (2003). Role of arthropod saliva in blood feeding: sialome and post-sialome perspectives. Annu. Rev. Entomol. *48*, 73–88.
92. Cantillo, J.F., Fernández-Caldas, E., and Puerta, L. (2014). Immunological aspects of the immune response induced by mosquito allergens. Int. Arch. Allergy Immunol. *165*, 271–282.

93. Wang, Z., Nie, K., Liang, Y., Niu, J., Yu, X., Zhang, O., Liu, L., Shi, X., Wang, Y., Feng, X., et al. (2024). A mosquito salivary protein-driven influx of myeloid cells facilitates flavivirus transmission. EMBO J. *43*, 1690–1721.
94. Pimenta, P.F., Touray, M., and Miller, L. (1994). The journey of malaria sporozoites in the mosquito salivary gland. J. Eukaryot. Microbiol. *41*, 608–624.
95. Raquin, V., and Lambrechts, L. (2017). Dengue virus replicates and accumulates in Aedes aegypti salivary glands. Virology *507*, 75–81.
96. Lee, W.-S., Webster, J.A., Madzokere, E.T., Stephenson, E.B., and Herrero, L.J. (2019). Mosquito antiviral defense mechanisms: a delicate balance between innate immunity and persistent viral infection. Parasit. Vectors *12*, 165.
97. Derouiche, S., Li, T., Sakai, Y., Uta, D., Aoyagi, S., and Tominaga, M. (2022). Inhibition of transient receptor potential vanilloid 1 and transient receptor potential ankyrin 1 by mosquito and mouse saliva. Pain *163*, 299–307.
98. Vega-Rúa, A., Zouache, K., Girod, R., Failloux, A.-B., and Lourenço-de-Oliveira, R. (2014). High level of vector competence of Aedes aegypti and Aedes albopictus from ten American countries as a crucial factor in the spread of Chikungunya virus. J. Virol. *88*, 6294–6306.
99. Sanchez-Vargas, I., Olson, K.E., and Black, W.C. (2021). The Genetic Basis for Salivary Gland Barriers to Arboviral Transmission. Insects *12*, 73.
100. Juhn, J., Naeem-Ullah, U., Maciel Guedes, B.A., Majid, A., Coleman, J., Paolucci Pimenta, P.F., Akram, W., James, A.A., and Marinotti, O. (2011). Spatial mapping of gene expression in the salivary glands of the dengue vector mosquito, Aedes aegypti. Parasit. Vectors *4*, 1.
101. Conway, M.J., Londono-Renteria, B., Troupin, A., Watson, A.M., Klimstra, W.B., Fikrig, E., and Colpitts, T.M. (2016). Aedes aegypti D7 Saliva Protein Inhibits Dengue Virus Infection. PLoS Negl. Trop. Dis. *10*, e0004941.
102. Chowdhury, A., Modahl, C.M., Missé, D., Kini, R.M., and Pompon, J. (2021). High resolution proteomics of Aedes aegypti salivary glands infected with either dengue, Zika or chikungunya viruses identify new virus specific and broad antiviral factors. Sci. Rep. *11*, 23696.
103. Fiorillo, C., Yen, P.-S., Colantoni, A., Mariconti, M., Azevedo, N., Lombardo, F., Failloux, A.-B., and Arcà, B. (2022). MicroRNAs and other small RNAs in Aedes aegypti saliva and salivary glands following chikungunya virus infection. Sci. Rep. *12*, 9536.
104. Maharaj, P.D., Widen, S.G., Huang, J., Wood, T.G., and Thangamani, S. (2015). Discovery of mosquito saliva microRNAs during CHIKV infection. PLoS Negl. Trop. Dis. *9*, e0003386.
105. Arcá, B., Lombardo, F., de Lara Capurro, M., della Torre, A., Dimopoulos, G., James, A.A., and Coluzzi, M. (1999). Trapping cDNAs encoding secreted proteins from the salivary glands of the malaria vector Anopheles gambiae. Proc. Natl. Acad. Sci. U. S. A. *96*, 1516–1521.
106. Hastings, A.K., Uraki, R., Gaitsch, H., Dhaliwal, K., Stanley, S., Sproch, H., Williamson, E., MacNeil, T., Marin-Lopez, A., Hwang, J., et al. (2019). Aedes aegypti NeSt1 Protein Enhances Zika Virus Pathogenesis by Activating Neutrophils. J. Virol. *93*, e00395–19.
107. Dhawan, R., Kumar, M., Mohanty, A.K., Dey, G., Advani, J., Prasad, T.S.K., and

Kumar, A. (2017). Mosquito-Borne Diseases and Omics: Salivary Gland Proteome of the Female Aedes aegypti Mosquito. OMICS *21*, 45–54.
108. Klug, D., Arnold, K., Mela-Lopez, R., Marois, E., and Blandin, S.A. (2022). A toolbox of engineered mosquito lines to study salivary gland biology and malaria transmission. PLoS Pathog. *18*, e1010881.
109. Wells, M.B., and Andrew, D.J. (2015). “Salivary gland cellular architecture in the Asian malaria vector mosquito Anopheles stephensi.” Parasit. Vectors *8*, 617.
110. Martin-Martin, I., Alves E Silva, T.L., Williams, A.E., Vega-Rodriguez, J., and Calvo, E. (2022). Performing Immunohistochemistry in Mosquito Salivary Glands. Cold Spring Harb. Protoc. *2022*, Pdb.top107699.
111. Wells, M.B., Villamor, J., and Andrew, D.J. (2017). Salivary gland maturation and duct formation in the African malaria mosquito Anopheles gambiae. Sci. Rep. *7*, 601.
112. Sun, P., Nie, K., Zhu, Y., Liu, Y., Wu, P., Liu, Z., Du, S., Fan, H., Chen, C.-H., Zhang, R., et al. (2020). A mosquito salivary protein promotes flavivirus transmission by activation of autophagy. Nat. Commun. *11*, 260.
113. Arnoldi, I., Mancini, G., Fumagalli, M., Gastaldi, D., D’Andrea, L., Bandi, C., Di Venere, M., Iadarola, P., Forneris, F., and Gabrieli, P. (2022). A salivary factor binds a cuticular protein and modulates biting by inducing morphological changes in the mosquito labrum. Curr. Biol. *32*, 3493–3504.e11.
114. Bulet, P., Hetru, C., Dimarcq, J.L., and Hoffmann, D. (1999). Antimicrobial peptides in insects; structure and function. Dev. Comp. Immunol. *23*, 329–344.
115. Dekker, T., Geier, M., and Cardé, R.T. (2005). Carbon dioxide instantly sensitizes female yellow fever mosquitoes to human skin odours. J. Exp. Biol. *208*, 2963–2972.
116. Gillies, M.T. (1980). The role of carbon dioxide in host-finding by mosquitoes (Diptera: Culicidae): a review. Bull. Entomol. Res. *70*, 525–532.
117. Grant, A.J., Wigton, B.E., Aghajanian, J.G., and O’Connell, R.J. (1995). Electrophysiological responses of receptor neurons in mosquito maxillary palp sensilla to carbon dioxide. J. Comp. Physiol. A *177*, 389–396.
118. Acree, F., Turner, R.B., Gouck, H.K., Beroza, M., and Smith, N. (1968). L-Lactic acid: a mosquito attractant isolated from humans. Science *161*, 1346–1347.
119. Cook, J.I., Majeed, S., Ignell, R., Pickett, J.A., Birkett, M.A., and Logan, J.G. (2011). Enantiomeric selectivity in behavioural and electrophysiological responses of Aedes aegypti and Culex quinquefasciatus mosquitoes. Bull. Entomol. Res. *101*, 541–550.
120. Raji, J.I., Konopka, J.K., and Potter, C.J. (2023). A spatial map of antennal-expressed ionotropic receptors in the malaria mosquito. Cell Rep. *42*, 112101.
121. Konopka, J.K., Task, D., Poinapen, D., and Potter, C.J. (2023). Neurogenetic identification of mosquito sensory neurons. iScience *26*, 106690.
122. Chandel, A., DeBeaubien, N.A., Ganguly, A., Meyerhof, G.T., Krumholz, A.A., Liu, J., Salgado, V.L., and Montell, C. (2024). Thermal infrared directs host-seeking behaviour in Aedes aegypti mosquitoes. Nature *633*, 615–623.
123. Ye, Z., Liu, F., Sun, H., Ferguson, S.T., Baker, A., Ochieng, S.A., and Zwiebel, L.J. (2022). Discrete roles of Ir76b ionotropic coreceptor impact olfaction, blood feeding,

and mating in the malaria vector mosquito Anopheles coluzzii. Proc. Natl. Acad. Sci. U. S. A. *119*, e2112385119.
124. Maguire, S.E., Afify, A., Goff, L.A., and Potter, C.J. (2022). Odorant-receptor-mediated regulation of chemosensory gene expression in the malaria mosquito Anopheles gambiae. Cell Rep. *38*, 110494.
125. Greppi, C., Laursen, W.J., Budelli, G., Chang, E.C., Daniels, A.M., van Giesen, L., Smidler, A.L., Catteruccia, F., and Garrity, P.A. (2020). Mosquito heat seeking is driven by an ancestral cooling receptor. Science *367*, 681–684.
126. Paris, V., Hardy, C., Hoffmann, A.A., and Ross, P.A. (2023). How often are male mosquitoes attracted to humans? R. Soc. Open Sci. *10*, 230921.
127. Basrur, N.S., De Obaldia, M.E., Morita, T., Herre, M., von Heynitz, R.K., Tsitohay, Y.N., and Vosshall, L.B. (2020). Fruitless mutant male mosquitoes gain attraction to human odor. Elife *9*, e63982.
128. Persad, S., Choo, Z.-N., Dien, C., Sohail, N., Masilionis, I., Chaligné, R., Nawy, T., Brown, C.C., Sharma, R., Pe'er, I., et al. (2023). SEACells infers transcriptional and epigenomic cellular states from single-cell genomics data. Nat. Biotechnol. *41*, 1746–1757.
129. Adams, C.M., Anderson, M.G., Motto, D.G., Price, M.P., Johnson, W.A., and Welsh, M.J. (1998). Ripped pocket and pickpocket, novel Drosophila DEG/ENaC subunits expressed in early development and in mechanosensory neurons. J. Cell Biol. *140*, 143–152.
130. Zelle, K.M., Lu, B., Pyfrom, S.C., and Ben-Shahar, Y. (2013). The genetic architecture of degenerin/epithelial sodium channels in Drosophila. G3 (Bethesda) *3*, 441–450.
131. Matthews, B.J., Younger, M.A., and Vosshall, L.B. (2019). The ion channel ppk301 controls freshwater egg-laying in the mosquito Aedes aegypti. Elife *8*, e43963.
132. Bohbot, J.D., Durand, N.F., Vinyard, B.T., and Dickens, J.C. (2013). Functional Development of the Octenol Response in Aedes aegypti. Front. Physiol. *4*, 39.
133. DeGennaro, M., McBride, C.S., Seeholzer, L., Nakagawa, T., Dennis, E.J., Goldman, C., Jasinskiene, N., James, A.A., and Vosshall, L.B. (2013). orco mutant mosquitoes lose strong preference for humans and are not repelled by volatile DEET. Nature *498*, 487–491.
134. Dennis, E.J., Goldman, O.V., and Vosshall, L.B. (2019). Aedes aegypti mosquitoes use their legs to sense DEET on contact. Curr. Biol. *29*, 1551–1556.e5.
135. Lang, J.T. (1977). Contact sex pheromone in the mosquito Culiseta inornata (Diptera: Culicidae. J. Med. Entomol. *14*, 448–454.
136. Lang, J.T., and Foster, W.A. (1976). Is There a Female Sex Pheromone in the MosquitoCuliseta inornata1,2,3. Environ. Entomol. *5*, 1109–1115.
137. Nijhout, H.F., and Craig, G.B., Jr (1971). REPRODUCTIVE ISOLATION IN *STEGOMYIA* MOSQUITOES. III EVIDENCE FOR A SEXUAL PHEROMONE. Entomol. Exp. Appl. *14*, 399–412.
138. Hudson, B.N.A. (1956). The behaviour of the female mosquito in selecting water for oviposition. J. Exp. Biol. *33*, 478–492.
139. Sanford, J.L., Shields, V.D.C., and Dickens, J.C. (2013). Gustatory receptor neuron responds to DEET and other insect repellents in the yellow-fever mosquito, Aedes aegypti. Sci. Nat. *100*, 269–273.

140. Sparks, J.T., Vinyard, B.T., and Dickens, J.C. (2013). Gustatory receptor expression in the labella and tarsi of Aedes aegypti. Insect Biochem. Mol. Biol. *43*, 1161–1171.
141. Pappas, L.G., and Larsen, J.R. (1976). Gustatory hairs on the mosquito, Culiseta inornata. J. Exp. Zool. *196*, 351–360.
142. Elizarov, Y.A., and Sinitsina, E.E. (1974). Contact chemoreceptors Aedes aegypti (Diptera: Culicidae). Zool Zh *53*, 577–584.
143. McIver, S.B. (1982). Sensilla mosquitoes (Diptera: Culicidae). J. Med. Entomol. *19*, 489–535.
144. Konopka, J.K., Task, D., Afify, A., Raji, J., Deibel, K., Maguire, S., Lawrence, R., and Potter, C.J. (2021). Olfaction in Anopheles mosquitoes. Chem. Senses *46*, bjab021.
145. Hopkins, B.R., Barmina, O., and Kopp, A. (2023). A single-cell atlas of the sexually dimorphic Drosophila foreleg and its sensory organs during development. PLoS Biol. *21*, e3002148.
146. Corfas, R.A., and Vosshall, L.B. (2015). The cation channel TRPA1 tunes mosquito thermotaxis to host temperatures. Elife *4*, e11750.
147. Liu, T., Wang, Y., Tian, Y., Zhang, J., Zhao, J., and Guo, A. (2020). The receptor channel formed by ppk25, ppk29 and ppk23 can sense the Drosophila female pheromone 7,11-heptacosadiene. Genes Brain Behav. *19*, e12529.
148. Predel, R., Neupert, S., Garczynski, S.F., Crim, J.W., Brown, M.R., Russell, W.K., Kahnt, J., Russell, D.H., and Nachman, R.J. (2010). Neuropeptidomics of the mosquito Aedes aegypti. J. Proteome Res. *9*, 2006–2015.
149. Amaro, I.A., Wohl, M.P., Pitcher, S., Alfonso-Parra, C., Avila, F.W., Paige, A.S., Helinski, M.E.H., Duvall, L.B., Harrington, L.C., Wolfner, M.F., et al. (2024). Sex peptide receptor is not required for refractoriness to remating or induction of egg laying in Aedes aegypti. Genetics *227*, iyae034.
150. Ju, L., Glastad, K.M., Sheng, L., Gospocic, J., Kingwell, C.J., Davidson, S.M., Kocher, S.D., Bonasio, R., and Berger, S.L. (2023). Hormonal gatekeeping via the blood-brain barrier governs caste-specific behavior in ants. Cell *186*, 4289–4309.e23.
151. Zhang, W., Wang, L., Zhao, Y., Wang, Y., Chen, C., Hu, Y., Zhu, Y., Sun, H., Cheng, Y., Sun, Q., et al. (2022). Single-cell transcriptomic analysis of honeybee brains identifies vitellogenin as caste differentiation-related factor. iScience *25*, 104643.
152. Klowden, M.J., and Lea, A.O. (1979). Effect of defensive host behavior on the blood meal size and feeding success of natural populations of mosquitoes (Diptera: Culicidae). J. Med. Entomol. *15*, 514–517.
153. Raji, J.I., and Potter, C.J. (2021). The number of neurons in Drosophila and mosquito brains. PLoS One *16*, e0250381.
154. Baik, L.S., Nave, C., Au, D.D., Guda, T., Chevez, J.A., Ray, A., and Holmes, T.C. (2020). Circadian Regulation of Light-Evoked Attraction and Avoidance Behaviors in Daytime- versus Nighttime-Biting Mosquitoes. Curr. Biol. *30*, 3252–3259.e3.
155. Dong, L., Hormigo, R., Barnett, J.M., Greppi, C., and Duvall, L.B. (2024). Circadian modulation of mosquito host-seeking persistence by Pigment-Dispersing Factor impacts daily biting patterns. Preprint at Neuroscience, https://doi.org/10.1101/2024.09.19.613886 https://doi.org/10.1101/2024.09.19.613886.

156. Tarashansky, A.J., Musser, J.M., Khariton, M., Li, P., Arendt, D., Quake, S.R., and Wang, B. (2021). Mapping single-cell atlases throughout Metazoa unravels cell type evolution. Elife *10*. https://doi.org/10.7554/eLife.66747.
157. Strausfeld, N.J., Wolff, G.H., and Sayre, M.E. (2020). Mushroom body evolution demonstrates homology and divergence across Pancrustacea. Elife *9*, e52411.
158. Davie, K., Janssens, J., Koldere, D., De Waegeneer, M., Pech, U., Kreft, Ł., Aibar, S., Makhzami, S., Christiaens, V., Bravo González-Blas, C., et al. (2018). A single-cell transcriptome atlas of the aging Drosophila brain. Cell *174*, 982–998.e20.
159. Lee, D., Shahandeh, M.P., Abuin, L., and Benton, R. (2025). Comparative single-cell transcriptomic atlases of drosophilid brains suggest glial evolution during ecological adaptation. PLoS Biol. *23*, e3003120.
160. Roy, S., Saha, T.T., Zou, Z., and Raikhel, A.S. (2018). Regulatory Pathways Controlling Female Insect Reproduction. Annu. Rev. Entomol. *63*, 489–511.
161. Brovero, S.G., Fortier, J.C., Hu, H., Lovejoy, P.C., Newell, N.R., Palmateer, C.M., Tzeng, R.-Y., Lee, P.-T., Zinn, K., and Arbeitman, M.N. (2021). Investigation of Drosophila fruitless neurons that express Dpr/DIP cell adhesion molecules. Elife *10*. https://doi.org/10.7554/eLife.63101.
162. Neville, M.C., Nojima, T., Ashley, E., Parker, D.J., Walker, J., Southall, T., Van de Sande, B., Marques, A.C., Fischer, B., Brand, A.H., et al. (2014). Male-specific fruitless isoforms target neurodevelopmental genes to specify a sexually dimorphic nervous system. Curr. Biol. *24*, 229–241.
163. Ito, H., Sato, K., Koganezawa, M., Ote, M., Matsumoto, K., Hama, C., and Yamamoto, D. (2012). Fruitless recruits two antagonistic chromatin factors to establish single-neuron sexual dimorphism. Cell *149*, 1327–1338.
164. Brovkina, M.V., Duffié, R., Burtis, A.E.C., and Clowney, E.J. (2021). Fruitless decommissions regulatory elements to implement cell-type-specific neuronal masculinization. PLoS Genet. *17*, e1009338.
165. Anderson, M.A.E., Gonzalez, E., Ang, J.X.D., Shackleford, L., Nevard, K., Verkuijl, S.A.N., Edgington, M.P., Harvey-Samuel, T., and Alphey, L. (2023). Closing the gap to effective gene drive in Aedes aegypti by exploiting germline regulatory elements. Nat. Commun. *14*, 338.
166. Li, M., Yang, T., Kandul, N.P., Bui, M., Gamez, S., Raban, R., Bennett, J., Sánchez C, H.M., Lanzaro, G.C., Schmidt, H., et al. (2020). Development of a confinable gene drive system in the human disease vector Aedes aegypti. Elife *9*. https://doi.org/10.7554/eLife.51701.
167. Bontonou, G., Saint-Leandre, B., Kafle, T., Baticle, T., Hassan, A., Sánchez-Alcañiz, J.A., and Arguello, J.R. (2024). Evolution of chemosensory tissues and cells across ecologically diverse Drosophilids. Nat. Commun. *15*, 1047.
168. Liu, L., Johnson, W.A., and Welsh, M.J. (2003). Drosophila DEG/ENaC pickpocket genes are expressed in the tracheal system, where they may be involved in liquid clearance. Proc. Natl. Acad. Sci. U. S. A. *100*, 2128–2133.
169. Lin, H., Mann, K.J., Starostina, E., Kinser, R.D., and Pikielny, C.W. (2005). A Drosophila DEG/ENaC channel subunit is required for male response to female pheromones. Proc. Natl. Acad. Sci. U. S. A. *102*, 12831–12836.
170. Lu, B., LaMora, A., Sun, Y., Welsh, M.J., and Ben-Shahar, Y. (2012).

ppk23-Dependent chemosensory functions contribute to courtship behavior in Drosophila melanogaster. PLoS Genet. *8*, e1002587.
171. Toda, H., Zhao, X., and Dickson, B.J. (2012). The Drosophila female aphrodisiac pheromone activates ppk23(+) sensory neurons to elicit male courtship behavior. Cell Rep. *1*, 599–607.
172. Liu, Z., Wu, M.-H., Wang, Q.-X., Lin, S.-Z., Feng, X.-Q., Li, B., and Liang, X. (2022). Drosophila mechanical nociceptors preferentially sense localized poking. Elife *11*, e76574.
173. Li, J., Merchant, A., Zhou, S., Wang, T., Zhou, X., and Zhou, C. (2022). Neuroanatomical basis of sexual dimorphism in the mosquito brain. iScience *25*, 105255.
174. Arican, C., Schmitt, F.J., Rössler, W., Strube-Bloss, M.F., and Nawrot, M.P. (2023). The mushroom body output encodes behavioral decision during sensory-motor transformation. Curr. Biol. *33*, 4217–4224.e4.
175. Bittern, J., Pogodalla, N., Ohm, H., Brüser, L., Kottmeier, R., Schirmeier, S., and Klämbt, C. (2021). Neuron-glia interaction in the Drosophila nervous system. Dev. Neurobiol. *81*, 438–452.
176. Yildirim, K., Petri, J., Kottmeier, R., and Klämbt, C. (2019). Drosophila glia: Few cell types and many conserved functions. Glia *67*, 5–26.
177. Winkler, B., Funke, D., Benmimoun, B., Spéder, P., Rey, S., Logan, M.A., and Klämbt, C. (2021). Brain inflammation triggers macrophage invasion across the blood-brain barrier in Drosophila during pupal stages. Sci. Adv. *7*, eabh0050.
178. Freeman, M.R., and Doherty, J. (2006). Glial cell biology in Drosophila and vertebrates. Trends Neurosci. *29*, 82–90.
179. MacNamee, S.E., Liu, K.E., Gerhard, S., Tran, C.T., Fetter, R.D., Cardona, A., Tolbert, L.P., and Oland, L.A. (2016). Astrocytic glutamate transport regulates a Drosophila CNS synapse that lacks astrocyte ensheathment. J. Comp. Neurol. *524*, 1979–1998.
180. De Backer, J.-F., and Grunwald Kadow, I.C. (2022). A role for glia in cellular and systemic metabolism: insights from the fly. Curr. Opin. Insect Sci. *53*, 100947.
181. Sanders, H.R., Evans, A.M., Ross, L.S., and Gill, S.S. (2003). Blood meal induces global changes in midgut gene expression in the disease vector, Aedes aegypti. Insect Biochem. Mol. Biol. *33*, 1105–1122.
182. Bonizzoni, M., Dunn, W.A., Campbell, C.L., Olson, K.E., Dimon, M.T., Marinotti, O., and James, A.A. (2011). RNA-seq analyses of blood-induced changes in gene expression in the mosquito vector species, Aedes aegypti. BMC Genomics *12*, 82.
183. Ding, J., Adiconis, X., Simmons, S.K., Kowalczyk, M.S., Hession, C.C., Marjanovic, N.D., Hughes, T.K., Wadsworth, M.H., Burks, T., Nguyen, L.T., et al. (2020). Systematic comparison of single-cell and single-nucleus RNA-sequencing methods. Nat. Biotechnol. *38*, 737–746.
184. Mika, K., and Benton, R. (2021). Olfactory Receptor Gene Regulation in Insects: Multiple Mechanisms for Singular Expression. Front. Neurosci. *15*, 738088.
185. Brahma, A., Frank, D.D., Pastor, P.D.H., Piekarski, P.K., Wang, W., Luo, J.-D., Carroll, T.S., and Kronauer, D.J.C. (2023). Transcriptional and post-transcriptional control of odorant receptor choice in ants. Curr. Biol. *33*, 5456–5466.e5.
186. Kim, N., Kang, H., Jo, A., Yoo, S.-A., and Lee, H.-O. (2023). Perspectives on

single-nucleus RNA sequencing in different cell types and tissues. J Pathol Transl Med *57*, 52–59.
187. Slyper, M., Porter, C.B., and Ashenberg, O. (2020). single-cell singlenucleus RNA-Seq toolbox fresh frozen human tumors. Nat Med *26*, 792–802.
188. Sayers, E.W., Beck, J., Bolton, E.E., Brister, J.R., Chan, J., Comeau, D.C., Connor, R., DiCuccio, M., Farrell, C.M., Feldgarden, M., et al. (2024). Database resources of the National Center for Biotechnology Information. Nucleic Acids Res. *52*, D33–D43.
189. Öztürk-Çolak, A., Marygold, S.J., Antonazzo, G., Attrill, H., Goutte-Gattat, D., Jenkins, V.K., Matthews, B.B., Millburn, G., Dos Santos, G., Tabone, C.J., et al. (2024). FlyBase: updates to the Drosophila genes and genomes database. Genetics *227*. https://doi.org/10.1093/genetics/iyad211.
190. Dainat, J. (2020). AGAT: Another Gff Analysis Toolkit handle annotations any GTF/GFF format.
191. Pertea, G., and Pertea, M. (2020). GFF utilities: GffRead and GffCompare. F1000Res. *9*, 304.
192. Python Software Foundation (2020). Python 3.8. https://www.python.org/downloads/release/python-380/.
193. Kluyver, T., Ragan-Kelley, B., Granger, B., Bussonnier, M., Frederic, J., and Willing, C. (2016). Jupyter Notebooks - publishing format reproducible computational workflows. In Positioning Power Academic Publishing: Players, Agents Agendas, F. Loizides and B. Schmidt, eds., pp. 87–90.
194. Harris, C.R., Millman, K.J., van der Walt, S.J., Gommers, R., Virtanen, P., Cournapeau, D., Wieser, E., Taylor, J., Berg, S., Smith, N.J., et al. (2020). Array programming with NumPy. Nature *585*, 357–362.
195. The pandas development team (2024). pandas-dev/pandas: Pandas (Zenodo) https://doi.org/10.5281/ZENODO.3509134.
196. Hunter, J.D. (2007). Matplotlib: A 2D Graphics Environment. Comput. Sci. Eng. *9*, 90–95.
197. Wolock, S.L., Lopez, R., and Klein, A.M. (2019). Scrublet: Computational identification of cell Doublets in Single-cell transcriptomic data. Cell Syst. *8*, 281–291.e9.
198. Levine, J.H., Simonds, E.F., Bendall, S.C., Davis, K.L., Amir, E.-A.D., Tadmor, M.D., Litvin, O., Fienberg, H.G., Jager, A., Zunder, E.R., et al. (2015). Data-driven phenotypic dissection of AML reveals progenitor-like cells that correlate with prognosis. Cell *162*, 184–197.
199. Virtanen, P., Gommers, R., Oliphant, T.E., Haberland, M., Reddy, T., Cournapeau, D., Burovski, E., Peterson, P., Weckesser, W., Bright, J., et al. (2020). SciPy 1.0: fundamental algorithms for scientific computing in Python. Nat. Methods *17*, 261–272.
200. Waskom, M., Botvinnik, O., O'Kane, D., Hobson, P., Lukauskas, S., Gemperline, D.C., Augspurger, T., Halchenko, Y., Cole, J.B., Warmenhoven, J., et al. (2017). mwaskom/seaborn: v0.8.1 (September 2017) (Zenodo) https://doi.org/10.5281/ZENODO.883859.
201. Virshup, I., Rybakov, S., Theis, F.J., Angerer, P., and Wolf, F.A. (2024). anndata: Access and store annotated data matrices. J. Open Source Softw. *9*, 4371.

202. Haghverdi, L., Lun, A.T.L., Morgan, M.D., and Marioni, J.C. (2018). Batch effects in single-cell RNA-sequencing data are corrected by matching mutual nearest neighbors. Nat. Biotechnol. *36*, 421–427.
203. Schindelin, J., Arganda-Carreras, I., Frise, E., Kaynig, V., Longair, M., Pietzsch, T., Preibisch, S., Rueden, C., Saalfeld, S., Schmid, B., et al. (2012). Fiji: an open-source platform for biological-image analysis. Nat. Methods *9*, 676–682.
204. McLaughlin, C.N., Brbić, M., Xie, Q., Li, T., Horns, F., Kolluru, S.S., Kebschull, J.M., Vacek, D., Xie, A., Li, J., et al. (2021). Single-cell transcriptomes of developing and adult olfactory receptor neurons in Drosophila. Elife *10*. https://doi.org/10.7554/eLife.63856.
205. McLaughlin, C.N., Qi, Y., Quake, S.R., Luo, L., and Li, H. (2022). Isolation and RNA sequencing of single nuclei from Drosophila tissues. STAR Protoc *3*, 101417.
206. Choi, H.M.T., Schwarzkopf, M., Fornace, M.E., Acharya, A., Artavanis, G., Stegmaier, J., Cunha, A., and Pierce, N.A. (2018). Third-generation in situ hybridization chain reaction: multiplexed, quantitative, sensitive, versatile, robust. Development *145*. https://doi.org/10.1242/dev.165753.
207. Moth, E., Messer, F., Chaudhary, S., and White-Cooper, H. (2024). Differential gene expression underpinning the production of distinct sperm morphs in the wax moth Galleria mellonella. Open Biol. *14*, 240002.
208. Herre, M. (2023). RNA in situ hybridization of whole-mount mosquito olfactory tissues. Cold Spring Harb. Protoc. *2023*, 4–7.
209. Sayers, E.W., Bolton, E.E., Brister, J.R., Canese, K., Chan, J., Comeau, D.C., Connor, R., Funk, K., Kelly, C., Kim, S., et al. (2022). Database resources of the national center for biotechnology information. Nucleic Acids Res. *50*, D20–D26.
210. Van Rossum, G., and Drake, F.L. (1995). Python reference manual. Centrum voor Wiskunde en Informatica Amsterdam.
211. Freytag, S., Tian, L., Lönnstedt, I., Ng, M., and Bahlo, M. (2018). Comparison of clustering tools in R for medium-sized 10x Genomics single-cell RNA-sequencing data. F1000Res. *7*, 1297.
212. Ahlmann-Eltze, C., and Huber, W. (2023). Comparison of transformations for single-cell RNA-seq data. Nat. Methods *20*, 665–672.
213. Hall, A.B., Basu, S., Jiang, X., Qi, Y., Timoshevskiy, V.A., Biedler, J.K., Sharakhova, M.V., Elahi, R., Anderson, M.A.E., Chen, X.-G., et al. (2015). SEX DETERMINATION. A male-determining factor in the mosquito Aedes aegypti. Science *348*, 1268–1270.
214. Nässel, D.R., and Winther, A.M.E. (2010). Drosophila neuropeptides in regulation of physiology and behavior. Prog. Neurobiol. *92*, 42–104.
215. Nässel, D.R., and Zandawala, M. (2019). Recent advances in neuropeptide signaling in Drosophila, from genes to physiology and behavior. Prog. Neurobiol. *179*, 101607.
216. Haghverdi, L., Buettner, F., and Theis, F.J. (2015). Diffusion maps for high-dimensional single-cell analysis of differentiation data. Bioinformatics *31*, 2989–2998.
217. Haber, A.L., Biton, M., Rogel, N., Herbst, R.H., Shekhar, K., Smillie, C., Burgin, G., Delorey, T.M., Howitt, M.R., Katz, Y., et al. (2017). A single-cell survey of the small intestinal epithelium. Nature *551*, 333–339.

218. Setty, M., Kiseliovas, V., Levine, J., Gayoso, A., Mazutis, L., and Pe'er, D. (2019). Characterization of cell fate probabilities in single-cell data with Palantir. Nat. Biotechnol. *37*, 451–460.
219. Setty, M., Tadmor, M.D., Reich-Zeliger, S., Angel, O., Salame, T.M., Kathail, P., Choi, K., Bendall, S., Friedman, N., and Pe'er, D. (2016). Wishbone identifies bifurcating developmental trajectories from single-cell data. Nat. Biotechnol. *34*, 637–645.
220. Azizi, E., Carr, A.J., Plitas, G., Cornish, A.E., Konopacki, C., Prabhakaran, S., Nainys, J., Wu, K., Kiseliovas, V., Setty, M., et al. (2018). Single-cell map of diverse immune phenotypes in the breast tumor microenvironment. Cell *174*, 1293–1308.e36.
221. Buitinck, L., Louppe, G., Blondel, M., Pedregosa, F., Mueller, A., Grisel, O., Niculae, V., Prettenhofer, P., Gramfort, A., Grobler, J., et al. (2013). API design for machine learning software: experiences from the scikit-learn project. arXiv [cs.LG]. https://doi.org/10.48550/ARXIV.1309.0238.
222. CellBender removes technical artifacts from single-cell RNA sequencing data (2023). Nat. Methods *20*, 1285–1286.
223. National Center for Biotechnology Information (NCBI)[Internet]. Bethesda (MD): National Library of Medicine (US), National Center for Biotechnology Information; [1988] https://www.ncbi.nlm.nih.gov/.

Supplemental figures

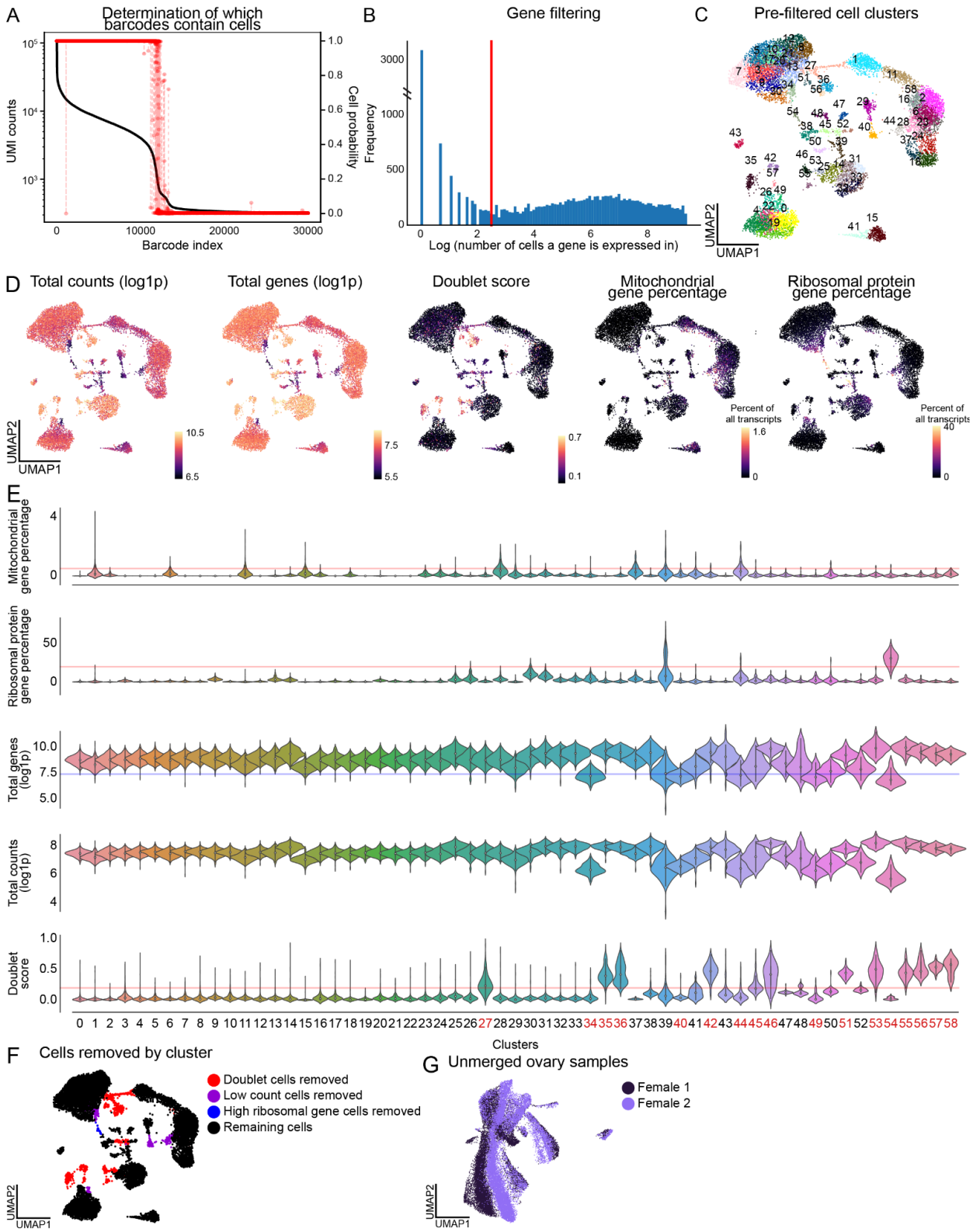

Figure S1. Processing of mated, sugar-fed female salivary gland sample, related to Figures 1 and 3.

(A) Determination of individual cell barcodes that contain cells by CellBender[222]. Unique molecular identifier (UMI) counts (black, left axis), probability that a barcode index is a cell (red, right axis). Low probability cells were removed by the CellBender.

(B) Histogram of number of cells that an individual gene is expressed in (log scale). Genes expressed in fewer than 13 cells were removed from a given sample (red line).

(C) UMAP of mated, sugar-fed salivary gland cells clustered using the Leiden algorithm (resolution = 5) for quality control and cell filtering.

(D-E) UMAPs **(D)** and violin plots **(E)** depicting total counts, total genes, doublet score (generated through scrublet[197], mitochondrial gene percentage, ribosomal gene percentages (log1p, indicates a pseudocount of 1 was used for log-scaling) for each cell and across each cluster. Lines in (E) indicate thresholds by which clusters with an average value above (red) or below (blue) were removed from further analysis. Removed clusters indicated in red on the bottom of (E).

(F) UMAP colored by cluster that were kept for further analysis (black) or removed due to quality control metrics depicted in (D-E).

(G) UMAP of mated, sugar-fed ovary samples female 1 (dark purple) and female 2 (light purple) prior to merging.

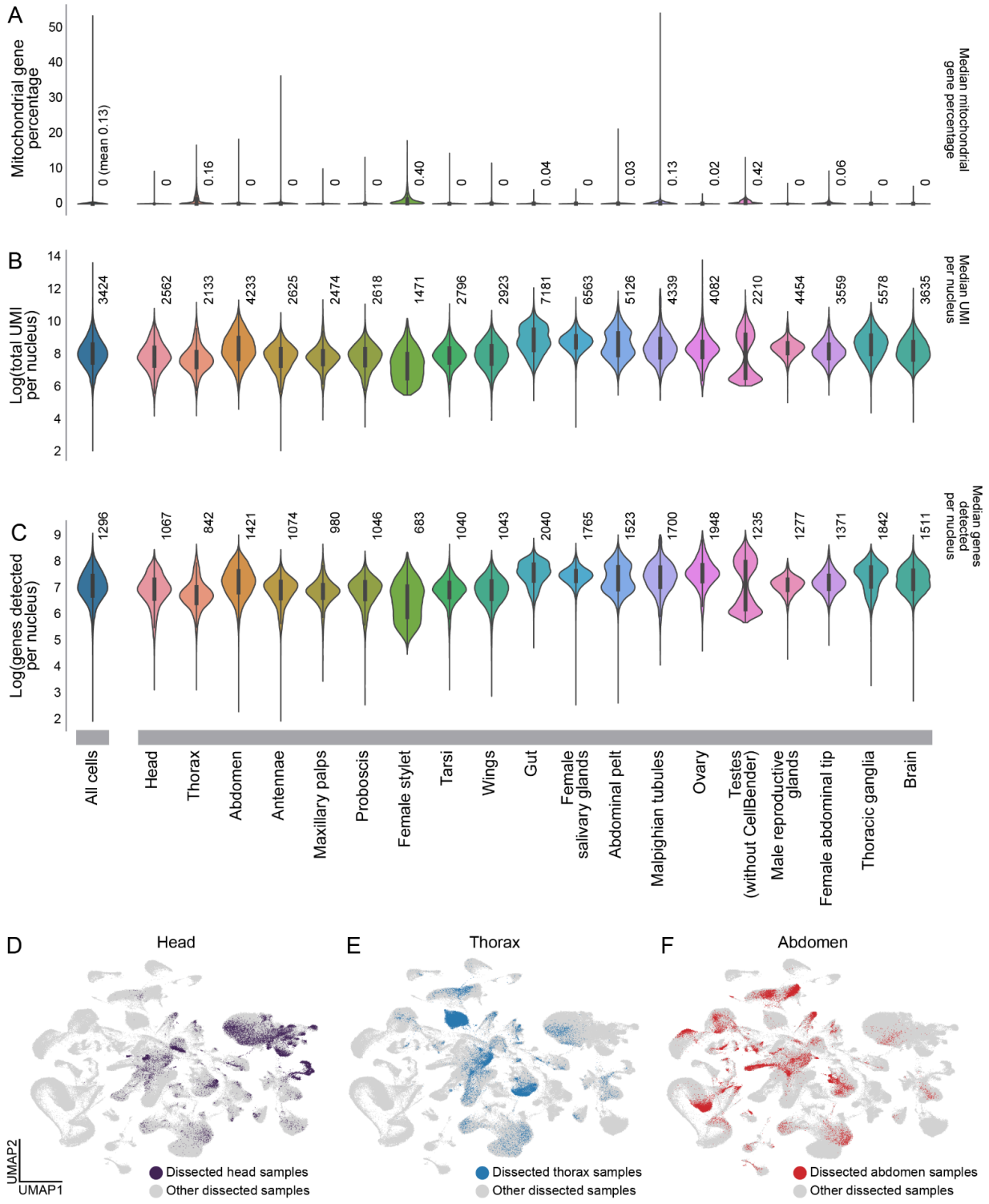
A
Mitochondrial gene percentage
0 (mean 0.13)
0
0.16
0
0
0
0
0.40
0
0
0.04
0
0.03
0.13
0.02
0.42
0
0.06
0
0
Median mitochondrial gene percentage
B
Log(total UMI per nucleus)
3424
2562
2133
4233
2625
2474
2618
1471
2796
2923
7181
6563
5126
4339
4082
2210
4454
3559
5578
3635
Median UMI per nucleus
C
Log(genes detected per nucleus)
1296
1067
842
1421
1074
980
1046
683
1040
1043
2040
1765
1523
1700
1948
1235
1277
1371
1842
1511
Median genes detected per nucleus
All cells
Head
Thorax
Abdomen
Antennae
Maxillary palps
Proboscis
Female stylet
Tarsi
Wings
Gut
Female salivary glands
Abdominal pelt
Malpighian tubules
Ovary
Testes (without CellBender)
Male reproductive glands
Female abdominal tip
Thoracic ganglia
Brain
D
Head
E
Thorax
F
Abdomen
UMAP2
UMAP1
Dissected head samples
Other dissected samples
Dissected thorax samples
Other dissected samples
Dissected abdomen samples
Other dissected samples

Figure S2. Final data quality control post filtering, related to Figure 1.
(A-C) Box plots depicting post-quality control filtering for mitochondrial gene percentage (A), total unique molecular identifiers (UMI) per nuclei (B), and genes detected per cell (C) for all cells (left) and for each tissue (right). Across all nuclei from all tissues, median mitochondrial gene percentage was 0.00% (mean 0.13%), median total UMI per nucleus was 3,424, and median genes per nucleus was 1,296. Annotations above each violin represent median values unless otherwise indicated. Pre-filtering gene per nucleus and UMI per nucleus metrics are available in Table S1, as well as filtering parameters. Note clusters were filtered by quality control metrics, not filtered by individual cells (Figure S1, Table S1). Multiple samples (10x Genomics libraries) from males and females are included for each tissues. Inner boxes represent first quartile to third quartile, and middle white point represents median. Box plot lines represent 1.5x interquartile range. Length of violin indicates complete range of the data, with thickness of the violin representing number of cells at that value.
(D-F) UMAPs of integrated *Aedes aegypti* Mosquito Cell Atlas data, colored by samples representing major body parts: female and male head (D), thorax (E), and abdomen (F).

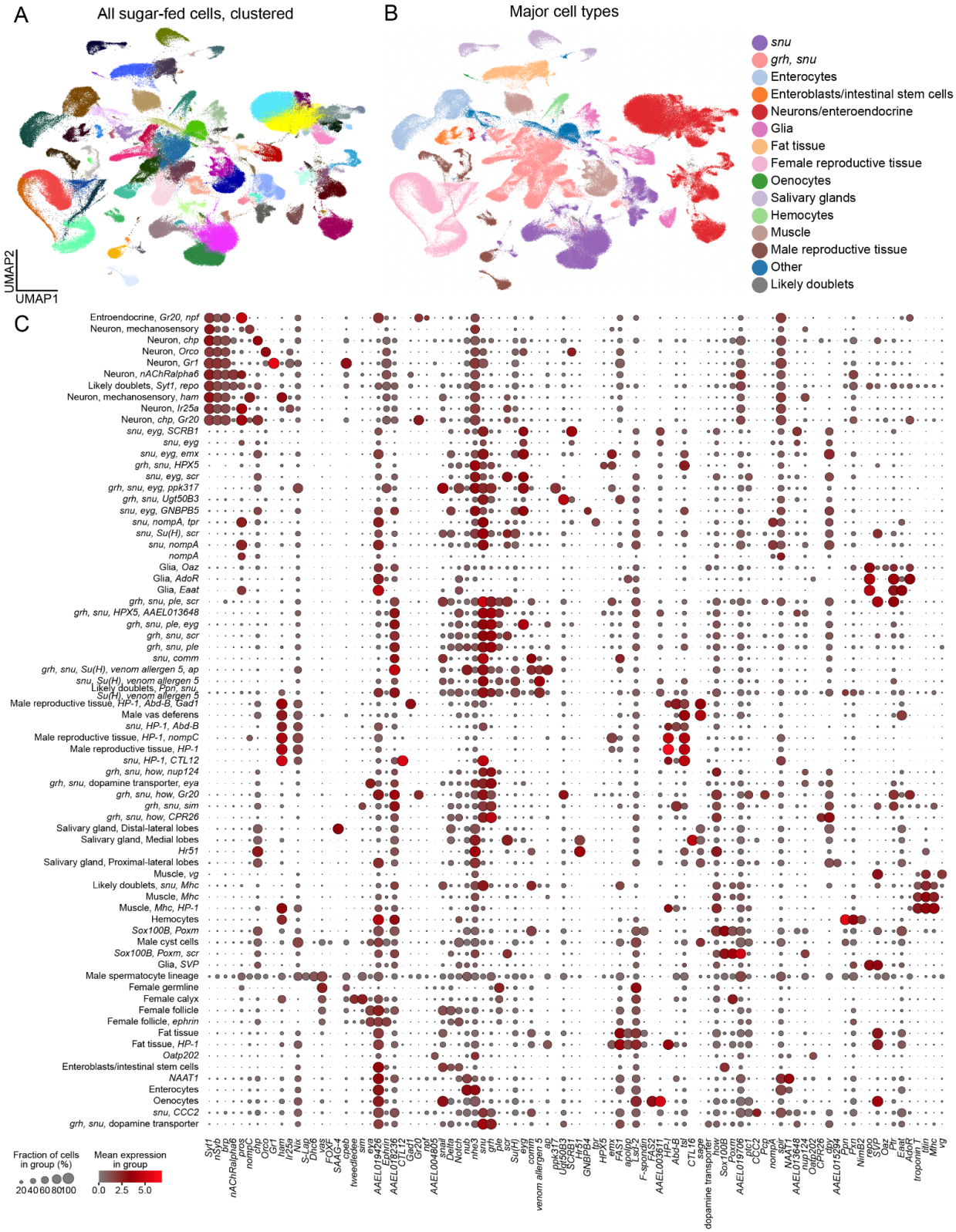
A
All sugar-fed cells, clustered
B
Major cell types
snu
grh, snu
Enterocytes
Enteroblasts/intestinal stem cells
Neurons/enteroendocrine
Glia
Fat tissue
Female reproductive tissue
Oenocytes
Salivary glands
Hemocytes
Muscle
Male reproductive tissue
Other
Likely doublets
UMAP2
UMAP1
C
Entroendocrine, Gr20, npf
Neuron, mechanosensory
Neuron, chp
Neuron, Orco
Neuron, Gr1
Neuron, nAChRalpha6
Likely doublets, Syt1, repo
Neuron, mechanosensory, ham
Neuron, Ir25a
Neuron, chp, Gr20
snu, eyg, SCRB1
snu, eyg
snu, eyg, emx
grh, snu, HPX5
snu, eyg, scr
grh, snu, eyg, ppk317
grh, snu, Ugt50B3
snu, eyg, GNBPB5
snu, nompA, tpr
snu, Su(H), scr
snu, nompA
nompA
Glia, Oaz
Glia, AdoR
Glia, Eaat
grh, snu, ple, scr
grh, snu, HPX5, AAEL013648
grh, snu, ple, eyg
grh, snu, scr
grh, snu, ple
snu, comm
grh, snu, Su(H), venom allergen 5, ap
snu, Su(H), venom allergen 5
Likely doublets, Ppn, snu, Su(H), venom allergen 5
Male reproductive tissue, HP-1, Abd-B, Gad1
Male vas deferens
snu, HP-1, Abd-B
Male reproductive tissue, HP-1, nompC
Male reproductive tissue, HP-1
snu, HP-1, CTL12
grh, snu, how, nup124
grh, snu, dopamine transporter, eya
grh, snu, how, Gr20
grh, snu, sim
grh, snu, how, CPR26
Salivary gland, Distal-lateral lobes
Salivary gland, Medial lobes
Hr51
Salivary gland, Proximal-lateral lobes
Muscle, vg
Likely doublets, snu, Mhc
Muscle, Mhc
Muscle, Mhc, HP-1
Hemocytes
Sox100B, Poxm
Male cyst cells
Sox100B, Poxm, scr
Glia, SVP
Male spermatocyte lineage
Female germline
Female calyx
Female follicle
Female follicle, ephrin
Fat tissue
Fat tissue, HP-1
Oatp202
Enteroblasts/intestinal stem cells
NAAT1
Enterocytes
Oenocytes
snu, CCC2
grh, snu, dopamine transporter
Syt1
nSyb
brp
nAChRalpha6
pros
nompC
chp
Orco
Gr1
ham
Ir25a
Nix
S-Lap
Dhc6
vas
FOXF
SAAG-4
opeb
tweedledee
sim
eya
AAEL019426
Ephrin
AAEL018236
CTL12
Gad1
Gr20
npf
AAEL004805
snail
Delta
Notch
nub
nhe3
snu
grh
ple
scr
Su(H)
eyg
comm
venom allergen 5
ap
ppk317
Ugt50B3
SCRB1
Hr51
GNBPB4
tpr
HPX5
emx
FAS1
apolpp
Lsd-2
F-spondin
FAS2
AAEL003611
HP-1
Abd-B
tsl
CTL16
sage
dopamine transporter
how
Sox100B
Poxm
AAEL019706
plc1
CCC2
Pcp
nompA
spir
NAAT1
AAEL013648
nup124
Oatp202
CPR26
dpy
AAEL015294
Ppn
Pxn
NimB2
repo
SVP
Oaz
Ptr
Eaat
AdoR
troponin T
titin
Mhc
vg
Fraction of cells in group (%)
20 40 60 80 100
Mean expression in group
0.0 2.5 5.0

Figure S3. Integrated *Aedes aegypti* Mosquito Cell Atlas tissues and data, related to Figure 1.

(A-B) UMAPs of integrated *Aedes aegypti* Mosquito Cell Atlas data colored by clustering (Louvain algorithm, resolution = 1) (A) and major cell types based on manual annotation in Figure 1F (B).

(C) Dotplot of integrated *Aedes aegypti* Mosquito Cell Atlas annotations and gene markers. Color scale indicates mean normalized expression of gene within cell type, size of dot indicates percent of cells expressing gene within the group. See Table S3 and Table S4 for gene IDs and thresholds.

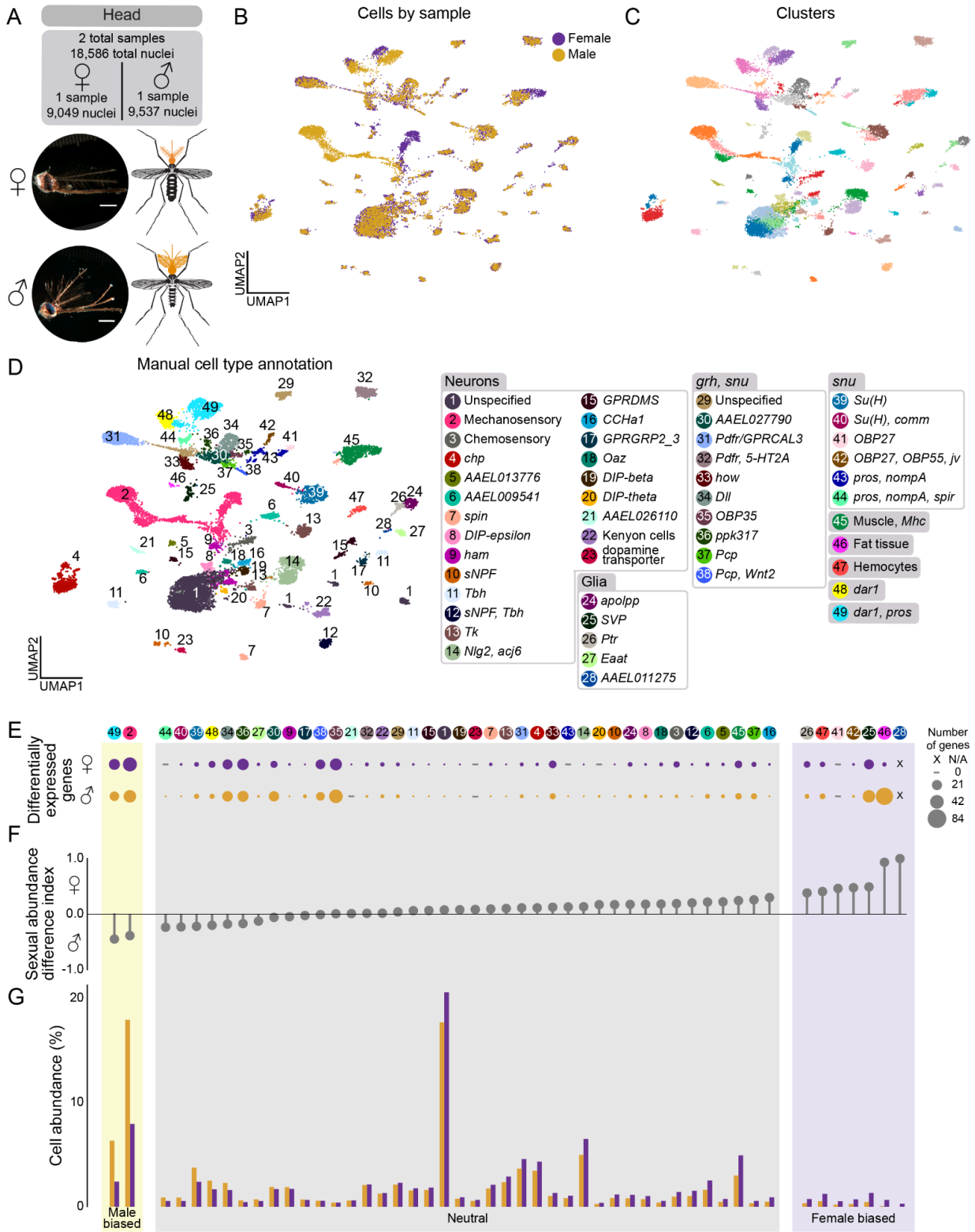
A
Head
2 total samples
18,586 total nuclei
1 sample
9,049 nuclei
1 sample
9,537 nuclei
B
Cells by sample
Female
Male
UMAP2
UMAP1
C
Clusters
D
Manual cell type annotation
Neurons
1 Unspecified
2 Mechanosensory
3 Chemosensory
4 chp
5 AAEL013776
6 AAEL009541
7 spin
8 DIP-epsilon
9 ham
10 sNPF
11 Tbh
12 sNPF, Tbh
13 Tk
14 Nlg2, acj6
15 GPRDMS
16 CCHa1
17 GPRGRP2_3
18 Oaz
19 DIP-beta
20 DIP-theta
21 AAEL026110
22 Kenyon cells
23 dopamine transporter
Glia
24 apolpp
25 SVP
26 Ptr
27 Eaat
28 AAEL011275
grh, snu
29 Unspecified
30 AAEL027790
31 Pdfr/GPRCAL3
32 Pdfr, 5-HT2A
33 how
34 Dll
35 OBP35
36 ppk317
37 Pcp
38 Pcp, Wnt2
snu
39 Su(H)
40 Su(H), comm
41 OBP27
42 OBP27, OBP55, jv
43 pros, nompA
44 pros, nompA, spir
45 Muscle, Mhc
46 Fat tissue
47 Hemocytes
48 dar1
49 dar1, pros
E
Differentially expressed genes
Number of genes
X N/A
0
21
42
84
F
Sexual abundance difference index
1.0
0.0
-1.0
G
Cell abundance (%)
20
10
0
Male biased
Neutral
Female biased

Figure S4. Annotation and differentially-expressed genes in mated, sugar-fed male and female heads, related to Figure 1.

(A) Representative photo of mated, sugar-fed female (top) and male (bottom) head dissection with anatomical diagram (in orange). Two samples (10x Genomics libraries) yielded 17,937 nuclei from 60 animals, post-quality control filtering. Scale bar: 500 μm.

(B) UMAP of head nuclei, colored by sample (female samples = 1, male samples = 1).

(C) UMAP of head cells clustered using the Leiden algorithm (resolution = 5) for annotation.

(D) UMAP of nuclei from both head samples, colored and numbered by manual annotation using selected marker genes as listed in legend at the right of the figure panel. Categorization of cell type annotations represented by shaded gray headers. See Table S3 and Table S4 for gene IDs and thresholds.

(E-G) Quantification of differences between male and female samples. Numbered and colored circles above (E) correspond to annotations in (D).

(E) Dot plot of number of differentially expressed genes between females and males in each cell type. Dots represent relative number of differentially expressed genes upregulated in male or female with a |log fold change| > 1 and false discovery rate < 0.05, determined by MAST on normalized expression and converted to $\log_2$ fold change.

(F) Sexual abundance difference index from data in (G). Each cell type was categorized based on the following index: Female biased (purple) if 0.3 < abundance index; Neutral (grey) if -0.3 ≤ abundance index ≤ 0.3; Male biased (yellow) if abundance index < -0.3.

(G) Bar plot of relative cell abundance, represented as the percent of each cell type of all nuclei collected from each sex for tissue. Separated by female (purple) and male (yellow).

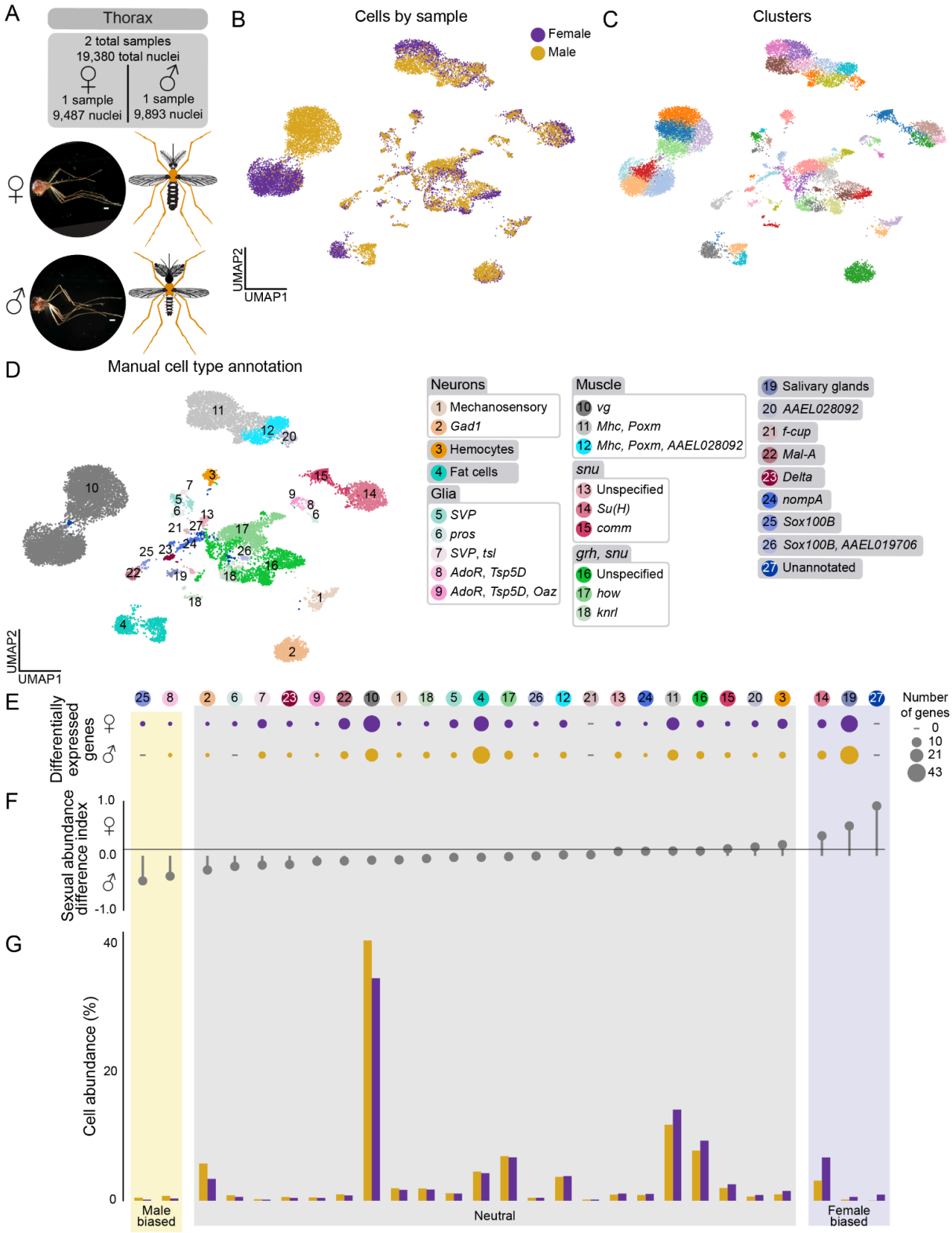
A
Thorax
2 total samples
19,380 total nuclei
1 sample
9,487 nuclei
1 sample
9,893 nuclei
B
Cells by sample
Female
Male
UMAP2
UMAP1
C
Clusters
D
Manual cell type annotation
Neurons
1 Mechanosensory
2 Gad1
3 Hemocytes
4 Fat cells
Glia
5 SVP
6 pros
7 SVP, tsl
8 AdoR, Tsp5D
9 AdoR, Tsp5D, Oaz
Muscle
10 vg
11 Mhc, Poxm
12 Mhc, Poxm, AAEL028092
snu
13 Unspecified
14 Su(H)
15 comm
grh, snu
16 Unspecified
17 how
18 knrl
19 Salivary glands
20 AAEL028092
21 f-cup
22 Mal-A
23 Delta
24 nompA
25 Sox100B
26 Sox100B, AAEL019706
27 Unannotated
E
Differentially expressed genes
Number of genes
0
10
21
43
F
Sexual abundance difference index
1.0
0.0
-1.0
G
Cell abundance (%)
40
20
0
Male biased
Neutral
Female biased

Figure S5. Annotation and differentially-expressed genes in mated, sugar-fed male and female thorax, related to Figure 1.

(A) Representative photo of mated, sugar-fed female (top) and male (bottom) thorax dissection with anatomical diagram (in orange). Two samples (10x Genomics libraries) yielded 19,380 nuclei from 180 animals, post-quality control filtering Scale bar: 500 µm.

(B) UMAP of thorax nuclei, colored by sample (female samples = 1, male samples = 1)

(C) UMAP of thorax nuclei clustered using the Leiden algorithm (resolution = 5) for annotation.

(D) UMAP of nuclei from both thorax samples, colored and numbered by manual annotation using selected marker genes as listed in legend at the right of the figure panel. Categorization of cell type annotations represented by shaded gray headers. See Table S3 and Table S4 for gene IDs and thresholds.

(E-G) Quantification of differences between male and female samples. Numbered and colored circles above (E) correspond to annotations in (D).

(E) Dot plot of number of differentially expressed genes between females and males in each cell type. Dots represent relative number of differentially expressed genes upregulated in male or female with a |log fold change| > 1 and false discovery rate < 0.05, determined by MAST on normalized expression and converted to $\log_2$ fold change.

(F) Sexual abundance difference index from data in (G). Each cell type was categorized based on the following index: Female biased (purple) if 0.3 < abundance index; Neutral (grey) if -0.3 ≤ abundance index ≤ 0.3; Male biased (yellow) if abundance index < -0.3.

(G) Bar plot of relative cell abundance, represented as the percent of each cell type of all nuclei collected from each sex for tissue. Separated by female (purple) and male (yellow).

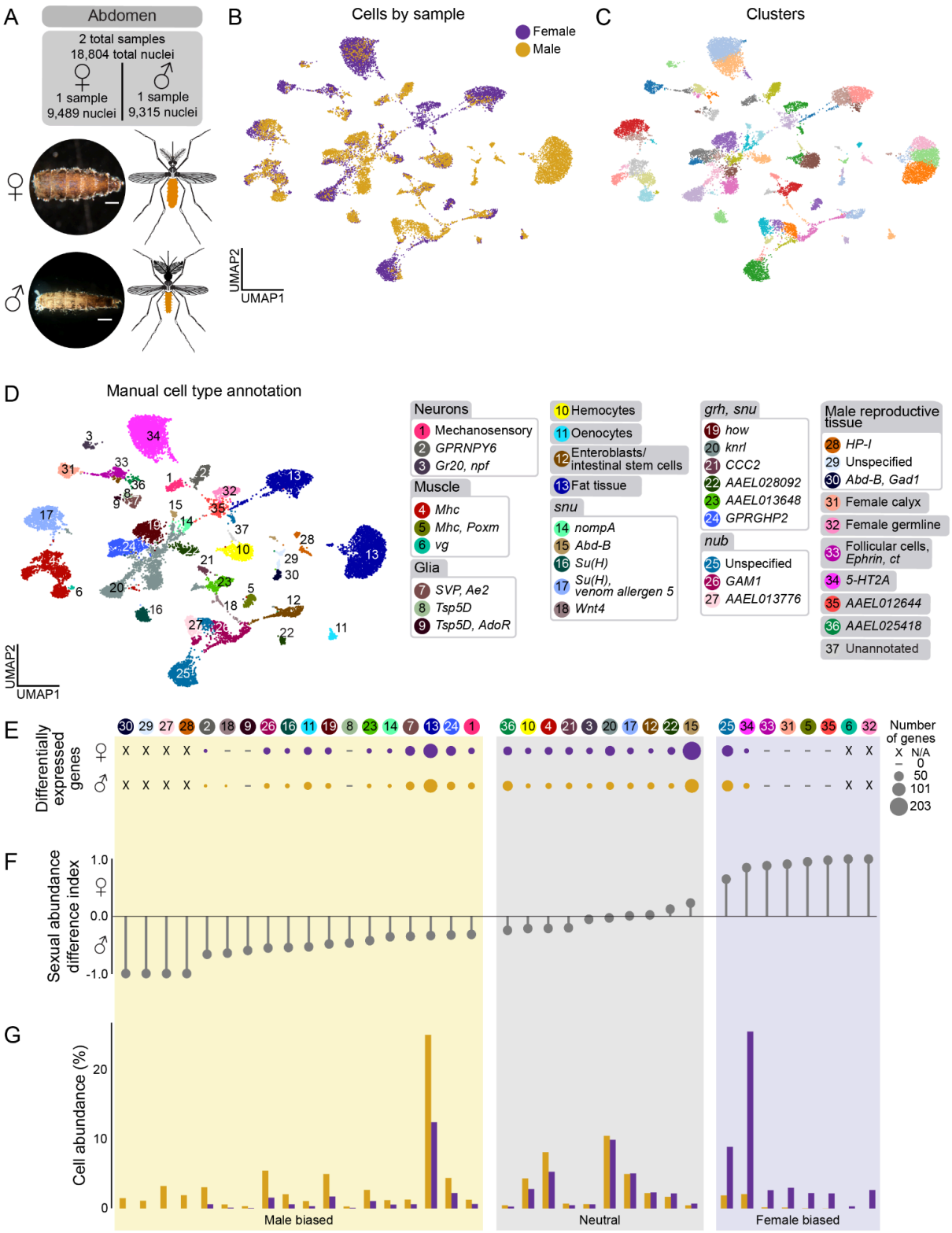
A
Abdomen
2 total samples
18,804 total nuclei
1 sample
9,489 nuclei
1 sample
9,315 nuclei
B
Cells by sample
Female
Male
UMAP2
UMAP1
C
Clusters
D
Manual cell type annotation
Neurons
1 Mechanosensory
2 GPRNPY6
3 Gr20, npf
Muscle
4 Mhc
5 Mhc, Poxm
6 vg
Glia
7 SVP, Ae2
8 Tsp5D
9 Tsp5D, AdoR
10 Hemocytes
11 Oenocytes
12 Enteroblasts/ intestinal stem cells
13 Fat tissue
snu
14 nompA
15 Abd-B
16 Su(H)
17 Su(H), venom allergen 5
18 Wnt4
grh, snu
19 how
20 knrl
21 CCC2
22 AAEL028092
23 AAEL013648
24 GPRGHP2
nub
25 Unspecified
26 GAM1
27 AAEL013776
Male reproductive tissue
28 HP-I
29 Unspecified
30 Abd-B, Gad1
31 Female calyx
32 Female germline
33 Follicular cells, Ephrin, ct
34 5-HT2A
35 AAEL012644
36 AAEL025418
37 Unannotated
E
Differentially expressed genes
Number of genes
X N/A
0
50
101
203
F
Sexual abundance difference index
1.0
0.0
-1.0
G
Cell abundance (%)
20
10
0
Male biased
Neutral
Female biased

Figure S6. Annotation and differentially-expressed genes in mated, sugar-fed male and female abdomen, related to Figure 1.

(A) Representative photo of mated, sugar-fed female (top) and male (bottom) abdomen dissection with anatomical diagram (in orange). Two samples (10x Genomics libraries) yielded 18,804 nuclei from 99 animals, post-quality control filtering. Scale bar: 500 μm.

(B) UMAP of abdomen nuclei, colored by sample (female samples = 1, male samples = 1)

(C) UMAP of abdomen nuclei clustered using the Leiden algorithm (resolution = 5) for annotation.

(D) UMAP of nuclei from both abdomen samples, colored and numbered by manual annotation using selected marker genes as listed in legend at the right of the figure panel. Categorization of cell type annotations represented by shaded gray headers. See Table S3 and Table S4 for gene IDs and thresholds.

(E-G) Quantification of differences between male and female samples. Numbered and colored circles above (E) correspond to annotations in (D).

(E) Dot plot of number of differentially expressed genes between females and males in each cell type. Dots represent relative number of differentially expressed genes upregulated in male or female with a |log fold change| > 1 and false discovery rate < 0.05, determined by MAST on normalized expression and converted to $\log_2$ fold change.

(F) Sexual abundance difference index from data in (G). Each cell type was categorized based on the following index: Female biased (purple) if 0.3 < abundance index; Neutral (grey) if -0.3 ≤ abundance index ≤ 0.3; Male biased (yellow) if abundance index < -0.3.

(G) Bar plot of relative cell abundance, represented as the percent of each cell type of all nuclei collected from each sex for tissue. Separated by female (purple) and male (yellow).

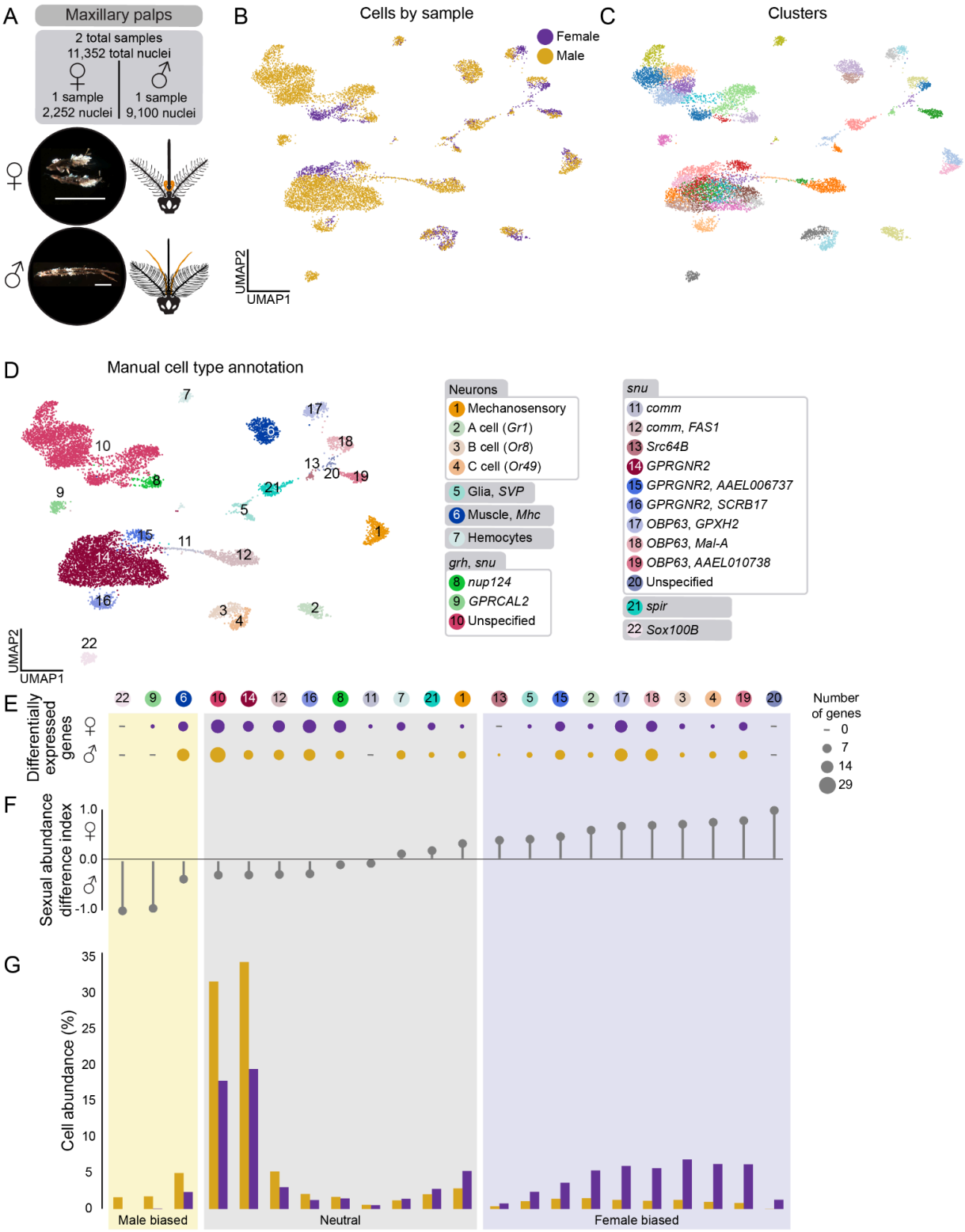
A
Maxillary palps
2 total samples
11,352 total nuclei
1 sample
2,252 nuclei
1 sample
9,100 nuclei
B
Cells by sample
Female
Male
UMAP2
UMAP1
C
Clusters
D
Manual cell type annotation
Neurons
1 Mechanosensory
2 A cell (Gr1)
3 B cell (Or8)
4 C cell (Or49)
5 Glia, SVP
6 Muscle, Mhc
7 Hemocytes
grh, snu
8 nup124
9 GPRCAL2
10 Unspecified
snu
11 comm
12 comm, FAS1
13 Src64B
14 GPRGNR2
15 GPRGNR2, AAEL006737
16 GPRGNR2, SCRB17
17 OBP63, GPXH2
18 OBP63, Mal-A
19 OBP63, AAEL010738
20 Unspecified
21 spir
22 Sox100B
E
Differentially expressed genes
Number of genes
0
7
14
29
F
Sexual abundance difference index
1.0
0.0
-1.0
G
Cell abundance (%)
35
30
25
20
15
10
5
0
Male biased
Neutral
Female biased

Figure S7. Annotation and differentially-expressed genes in mated, sugar-fed male and female maxillary palps, related to Figure 1.

(A) Representative photo of mated, sugar-fed female (top) and male (bottom) maxillary palp dissection with anatomical diagram (in orange). Two samples (10x Genomics libraries) yielded 11,352 nuclei from 1,967 animals, post-quality control filtering. Scale bar: 500 μm.

(B) UMAP of maxillary palp nuclei, colored by sample (female samples = 1, male samples = 1)

(C) UMAP of maxillary palp nuclei clustered using the Leiden algorithm (resolution = 5) for annotation.

(D) UMAP of nuclei from both maxillary palp samples, colored and numbered by manual annotation using selected marker genes as listed in legend at the right of the figure panel. Categorization of cell type annotations represented by shaded gray headers. See Table S3 and Table S4 for gene IDs and thresholds.

(E-G) Quantification of differences between male and female samples. Numbered and colored circles above (E) correspond to annotations in (D).

(E) Dot plot of number of differentially expressed genes between females and males in each cell type. Dots represent relative number of differentially expressed genes upregulated in male or female with a |log fold change| > 1 and false discovery rate < 0.05, determined by MAST on normalized expression and converted to $\log_2$ fold change.

(F) Sexual abundance difference index from data in (G). Each cell type was categorized based on the following index: Female biased (purple) if 0.3 < abundance index; Neutral (grey) if -0.3 ≤ abundance index ≤ 0.3; Male biased (yellow) if abundance index < -0.3.

(G) Bar plot of relative cell abundance, represented as the percent of each cell type of all nuclei collected from each sex for tissue. Separated by female (purple) and male (yellow).

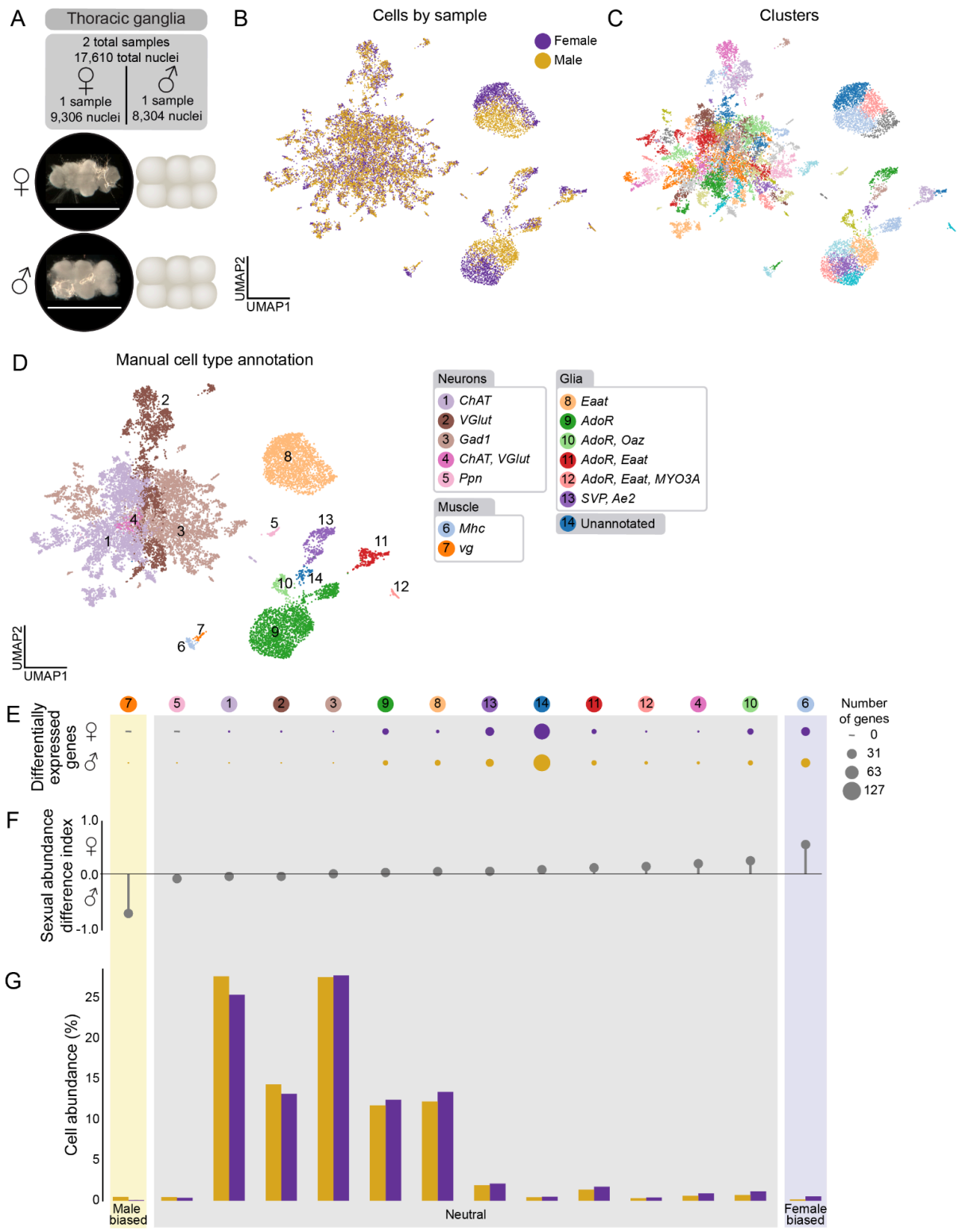
A
Thoracic ganglia
2 total samples
17,610 total nuclei
1 sample
9,306 nuclei
1 sample
8,304 nuclei
B
Cells by sample
Female
Male
UMAP2
UMAP1
C
Clusters
D
Manual cell type annotation
Neurons
1 ChAT
2 VGlut
3 Gad1
4 ChAT, VGlut
5 Ppn
Muscle
6 Mhc
7 vg
Glia
8 Eaat
9 AdoR
10 AdoR, Oaz
11 AdoR, Eaat
12 AdoR, Eaat, MYO3A
13 SVP, Ae2
14 Unannotated
E
Differentially expressed genes
Number of genes
0
31
63
127
F
Sexual abundance difference index
1.0
0.0
-1.0
G
Cell abundance (%)
Male biased
Neutral
Female biased

Figure S8. Annotation and differentially-expressed genes in mated, sugar-fed male and female thoracic ganglia, related to Figure 1.

(A) Representative photo of mated, sugar-fed female (top) and male (bottom) thoracic ganglia dissection with anatomical diagram. Two samples (10x Genomics libraries) yielded 17,610 nuclei from 240 animals, post-quality control filtering. Scale bar: 500 μm.

(B) UMAP of thoracic ganglia nuclei, colored by sample (female samples = 1, male samples = 1)

(C) UMAP of thoracic ganglia nuclei clustered using the Leiden algorithm (resolution = 5) for annotation.

(D) UMAP of nuclei from both thoracic ganglia samples, colored and numbered by manual annotation using selected marker genes as listed in legend at the right of the figure panel. Categorization of cell type annotations represented by shaded gray headers. See Table S3 and Table S4 for gene IDs and thresholds.

(E-G) Quantification of differences between male and female samples. Numbered and colored circles above (E) correspond to annotations in (D).

(E) Dot plot of number of differentially expressed genes between females and males in each cell type. Dots represent relative number of differentially expressed genes upregulated in male or female with a |log fold change| > 1 and false discovery rate < 0.05, determined by MAST on normalized expression and converted to $\log_2$ fold change.

(F) Sexual abundance difference index from data in (G). Each cell type was categorized based on the following index: Female biased (purple) if 0.3 < abundance index; Neutral (grey) if -0.3 ≤ abundance index ≤ 0.3; Male biased (yellow) if abundance index < -0.3.

(G) Bar plot of relative cell abundance, represented as the percent of each cell type of all nuclei collected from each sex for tissue. Separated by female (purple) and male (yellow).

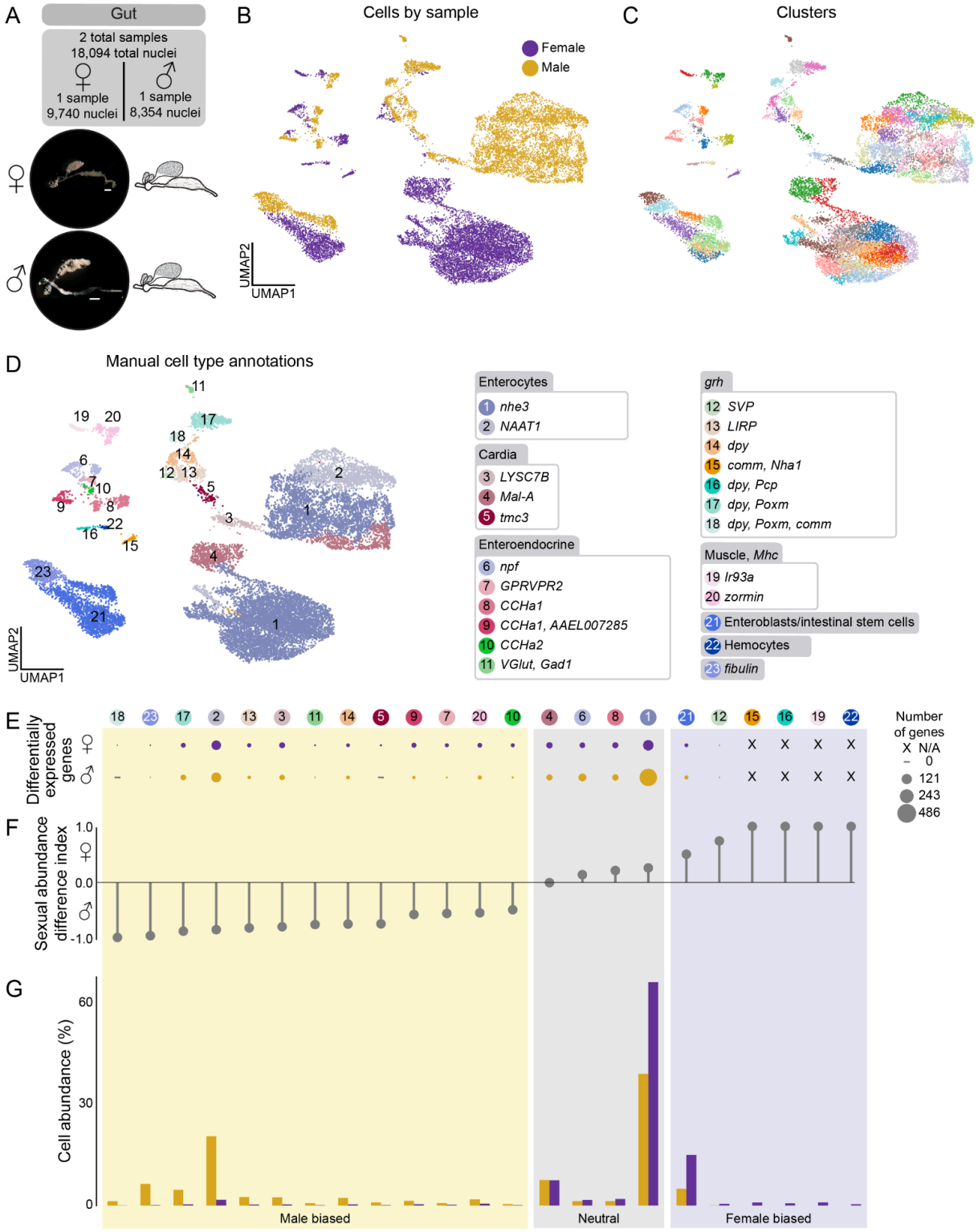
A
Gut
2 total samples
18,094 total nuclei
1 sample
9,740 nuclei
1 sample
8,354 nuclei
B
Cells by sample
Female
Male
UMAP2
UMAP1
C
Clusters
D
Manual cell type annotations
Enterocytes
1 nhe3
2 NAAT1
Cardia
3 LYSC7B
4 Mal-A
5 tmc3
Enteroendocrine
6 npf
7 GPRVPR2
8 CCHa1
9 CCHa1, AAEL007285
10 CCHa2
11 VGlut, Gad1
grh
12 SVP
13 LIRP
14 dpy
15 comm, Nha1
16 dpy, Pcp
17 dpy, Poxm
18 dpy, Poxm, comm
Muscle, Mhc
19 Ir93a
20 zormin
21 Enteroblasts/intestinal stem cells
22 Hemocytes
23 fibulin
E
Differentially expressed genes
Number of genes
X N/A
0
121
243
486
F
Sexual abundance difference index
1.0
0.0
-1.0
G
Cell abundance (%)
60
30
0
Male biased
Neutral
Female biased

Figure S9. Annotation and differentially-expressed genes in mated, sugar-fed male and female gut, related to Figure 1.

(A) Representative photo of mated, sugar-fed female (top) and male (bottom) gut dissection with anatomical diagram. Two samples (10x Genomics libraries) yielded 18,094 nuclei from 180 animals, post-quality control filtering. Scale bar: 500 μm.

(B) UMAP of gut nuclei, colored by sample (female samples = 1, male samples = 1)

(C) UMAP of gut nuclei clustered using the Leiden algorithm (resolution = 5) for annotation.

(D) UMAP of nuclei from both gut samples, colored and numbered by manual annotation using selected marker genes as listed in legend at the right of the figure panel. Categorization of cell type annotations represented by shaded gray headers. See Table S3 and Table S4 for gene IDs and thresholds.

(E-G) Quantification of differences between male and female samples. Numbered and colored circles above (E) correspond to annotations in (D).

(E) Dot plot of number of differentially expressed genes between females and males in each cell type. Dots represent relative number of differentially expressed genes upregulated in male or female with a |log fold change| > 1 and false discovery rate < 0.05, determined by MAST on normalized expression and converted to $\log_2$ fold change.

(F) Sexual abundance difference index from data in (G). Each cell type was categorized based on the following index: Female biased (purple) if 0.3 < abundance index; Neutral (grey) if -0.3 ≤ abundance index ≤ 0.3; Male biased (yellow) if abundance index < -0.3.

(G) Bar plot of relative cell abundance, represented as the percent of each cell type of all nuclei collected from each sex for tissue. Separated by female (purple) and male (yellow).

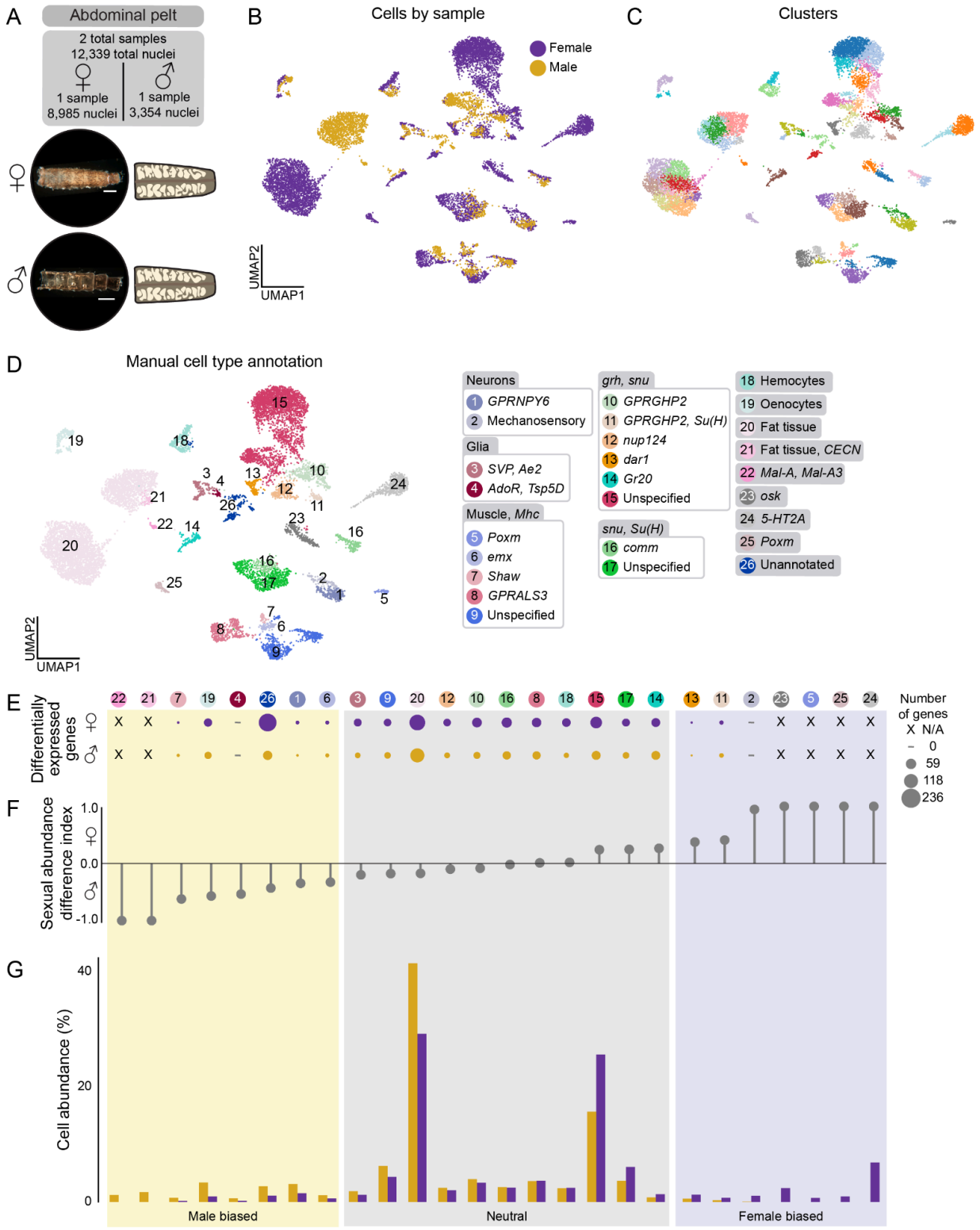
A
Abdominal pelt
2 total samples
12,339 total nuclei
♀
1 sample
8,985 nuclei
♂
1 sample
3,354 nuclei
B
Cells by sample
Female
Male
UMAP2
UMAP1
C
Clusters
D
Manual cell type annotation
Neurons
1 GPRNPY6
2 Mechanosensory
Glia
3 SVP, Ae2
4 AdoR, Tsp5D
Muscle, Mhc
5 Poxm
6 emx
7 Shaw
8 GPRALS3
9 Unspecified
grh, snu
10 GPRGHP2
11 GPRGHP2, Su(H)
12 nup124
13 dar1
14 Gr20
15 Unspecified
snu, Su(H)
16 comm
17 Unspecified
18 Hemocytes
19 Oenocytes
20 Fat tissue
21 Fat tissue, CECN
22 Mal-A, Mal-A3
23 osk
24 5-HT2A
25 Poxm
26 Unannotated
E
Differentially expressed genes
Number of genes
X N/A
– 0
59
118
236
F
Sexual abundance difference index
1.0
0.0
-1.0
G
Cell abundance (%)
40
20
0
Male biased
Neutral
Female biased

Figure S10. Annotation and differentially-expressed genes in mated, sugar-fed male and female abdominal pelt, related to Figure 1.

(A) Representative photo of mated, sugar-fed female (top) and male (bottom) abdominal pelt dissection with anatomical diagram. Two samples (10x Genomics libraries) yielded 12,339 nuclei from 180 animals, post-quality control filtering. Scale bar: 500 µm.

(B) UMAP of abdominal pelt nuclei, colored by sample (female samples = 1, male samples = 1)

(C) UMAP of abdominal pelt nuclei clustered using the Leiden algorithm (resolution = 5) for annotation.

(D) UMAP of nuclei from both abdominal pelt samples, colored and numbered by manual annotation using selected marker genes as listed in legend at the right of the figure panel. Categorization of cell type annotations represented by shaded gray headers. See Table S3 and Table S4 for gene IDs and thresholds.

(E-G) Quantification of differences between male and female samples. Numbered and colored circles above (E) correspond to annotations in (D).

(E) Dot plot of number of differentially expressed genes between females and males in each cell type. Dots represent relative number of differentially expressed genes upregulated in male or female with a |log fold change| > 1 and false discovery rate < 0.05, determined by MAST on normalized expression and converted to $\log_2$ fold change.

(F) Sexual abundance difference index from data in (G). Each cell type was categorized based on the following index: Female biased (purple) if 0.3 < abundance index; Neutral (grey) if -0.3 ≤ abundance index ≤ 0.3; Male biased (yellow) if abundance index < -0.3.

(G) Bar plot of relative cell abundance, represented as the percent of each cell type of all nuclei collected from each sex for tissue. Separated by female (purple) and male (yellow).

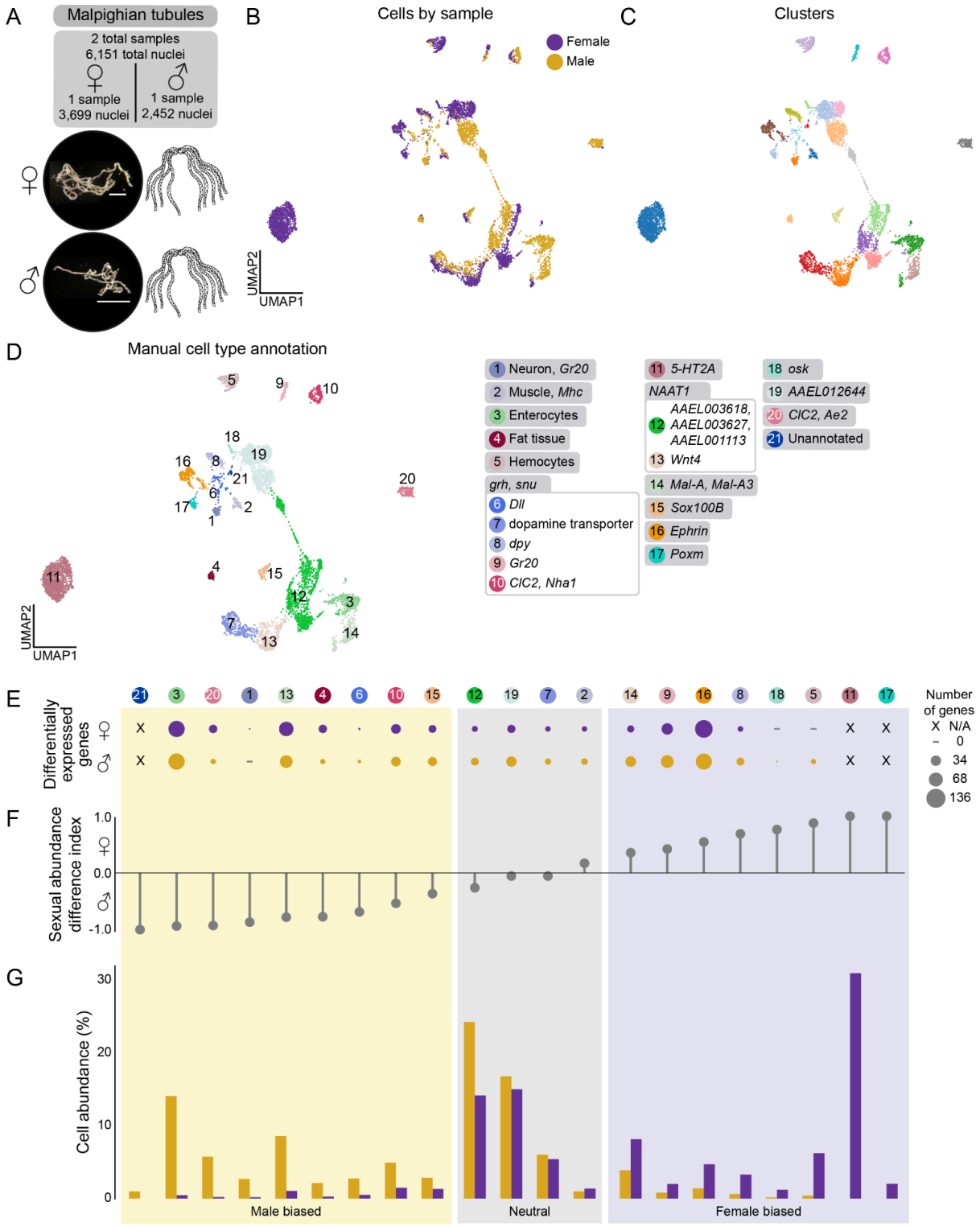
A
Malpighian tubules
2 total samples
6,151 total nuclei
♀
1 sample
3,699 nuclei
♂
1 sample
2,452 nuclei
B
Cells by sample
Female
Male
UMAP2
UMAP1
C
Clusters
D
Manual cell type annotation
1 Neuron, Gr20
2 Muscle, Mhc
3 Enterocytes
4 Fat tissue
5 Hemocytes
grh, snu
6 Dll
7 dopamine transporter
8 dpy
9 Gr20
10 ClC2, Nha1
11 5-HT2A
NAAT1
12 AAEL003618, AAEL003627, AAEL001113
13 Wnt4
14 Mal-A, Mal-A3
15 Sox100B
16 Ephrin
17 Poxm
18 osk
19 AAEL012644
20 ClC2, Ae2
21 Unannotated
E
Differentially expressed genes
Number of genes
X N/A
0
34
68
136
F
Sexual abundance difference index
1.0
0.0
-1.0
G
Cell abundance (%)
30
20
10
0
Male biased
Neutral
Female biased

Figure S11. Annotation and differentially-expressed genes in mated, sugar-fed male and female malpighian tubules, related to Figure 1.

(A) Representative photo of mated, sugar-fed female (top) and male (bottom) malpighian tubule dissection with anatomical diagram. Two samples (10x Genomics libraries) yielded 6,151 nuclei from 309 animals, post-quality control filtering. Scale bar: 500 µm.

(B) UMAP of malpighian tubules nuclei, colored by sample (female samples = 1, male samples = 1)

(C) UMAP of malpighian tubules nuclei clustered using the Leiden algorithm (resolution = 5) for annotation.

(D) UMAP of nuclei from both malpighian tubules samples, colored and numbered by manual annotation using selected marker genes as listed in legend at the right of the figure panel. Categorization of cell type annotations represented by shaded gray headers. See Table S3 and Table S4 for gene IDs and thresholds.

(E-G) Quantification of differences between male and female samples. Numbered and colored circles above (E) correspond to annotations in (D).

(E) Dot plot of number of differentially expressed genes between females and males in each cell type. Dots represent relative number of differentially expressed genes upregulated in male or female with a |log fold change| > 1 and false discovery rate < 0.05, determined by MAST on normalized expression and converted to $\log_2$ fold change.

(F) Sexual abundance difference index from data in (G). Each cell type was categorized based on the following index: Female biased (purple) if 0.3 < abundance index; Neutral (grey) if -0.3 ≤ abundance index ≤ 0.3; Male biased (yellow) if abundance index < -0.3.

(G) Bar plot of relative cell abundance, represented as the percent of each cell type of all nuclei collected from each sex for tissue. Separated by female (purple) and male (yellow).

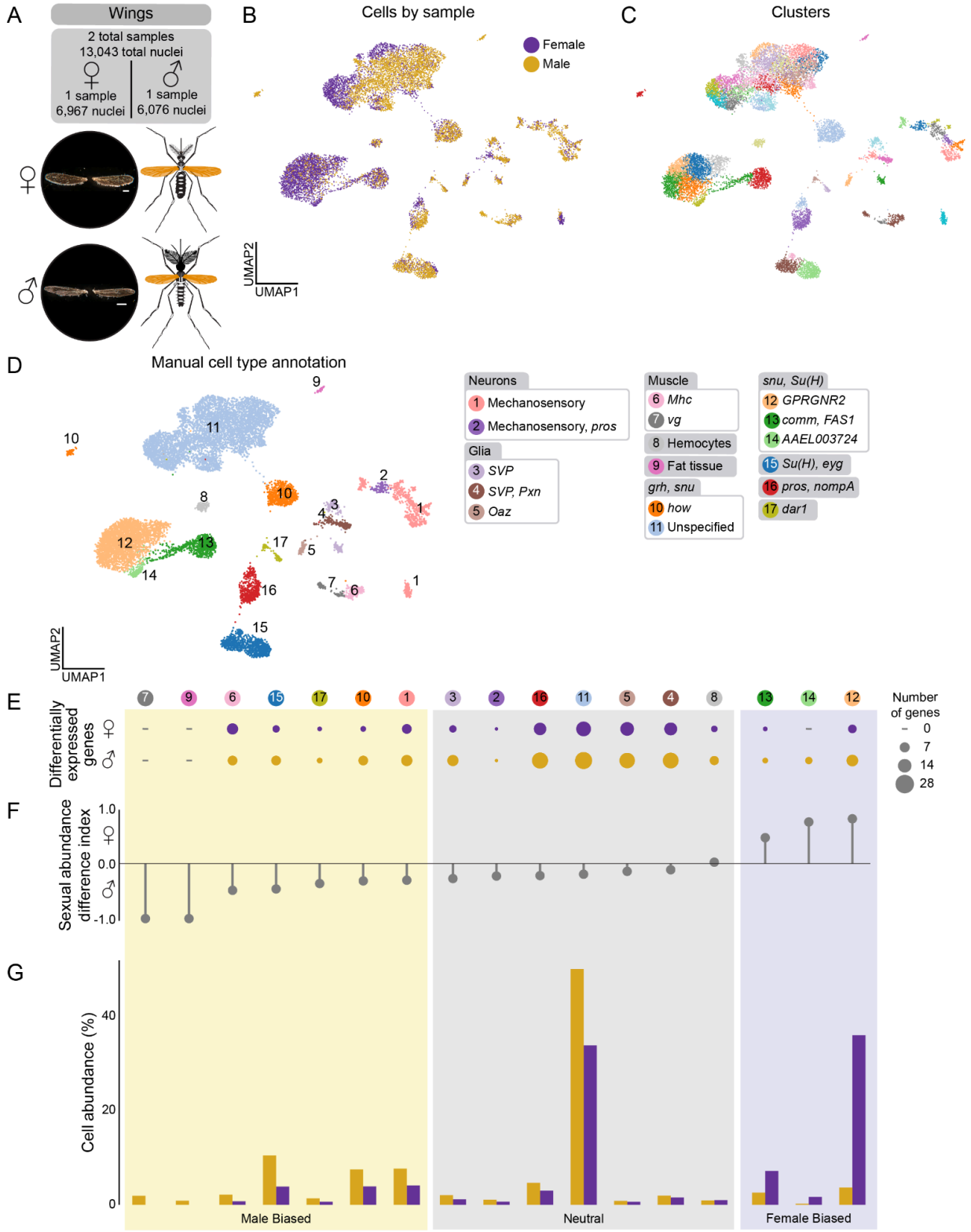
A
Wings
2 total samples
13,043 total nuclei
1 sample
6,967 nuclei
1 sample
6,076 nuclei
B
Cells by sample
Female
Male
UMAP2
UMAP1
C
Clusters
D
Manual cell type annotation
Neurons
1 Mechanosensory
2 Mechanosensory, pros
Glia
3 SVP
4 SVP, Pxn
5 Oaz
Muscle
6 Mhc
7 vg
8 Hemocytes
9 Fat tissue
grh, snu
10 how
11 Unspecified
snu, Su(H)
12 GPRGNR2
13 comm, FAS1
14 AAEL003724
15 Su(H), eyg
16 pros, nompA
17 dar1
E
Differentially expressed genes
Number of genes
0
7
14
28
F
Sexual abundance difference index
1.0
0.0
-1.0
G
Cell abundance (%)
40
20
0
Male Biased
Neutral
Female Biased

Figure S12. Annotation and differentially-expressed genes in mated, sugar-fed male and female wings, related to Figure 1.

(A) Representative photo of mated, sugar-fed female (top) and male (bottom) wing dissection with anatomical diagram (in orange). Two samples (10x Genomics libraries) yielded 13,043 nuclei from 528 animals, post-quality control filtering. Scale bar: 500 µm.

(B) UMAP of wing nuclei, colored by sample (female samples = 1, male samples = 1)

(C) UMAP of wing nuclei clustered using the Leiden algorithm (resolution = 5) for annotation.

(D) UMAP of nuclei from both wing samples, colored and numbered by manual annotation using selected marker genes as listed in legend at the right of the figure panel. Categorization of cell type annotations represented by shaded gray headers. See Table S3 and Table S4 for gene IDs and thresholds.

(E-G) Quantification of differences between male and female samples. Numbered and colored circles above (E) correspond to annotations in (D).

(E) Dot plot of number of differentially expressed genes between females and males in each cell type. Dots represent relative number of differentially expressed genes upregulated in male or female with a |log fold change| > 1 and false discovery rate < 0.05, determined by MAST on normalized expression and converted to $\log_2$ fold change.

(F) Sexual abundance difference index from data in (G). Each cell type was categorized based on the following index: Female biased (purple) if 0.3 < abundance index; Neutral (grey) if -0.3 ≤ abundance index ≤ 0.3; Male biased (yellow) if abundance index < -0.3.

(G) Bar plot of relative cell abundance, represented as the percent of each cell type of all nuclei collected from each sex for tissue. Separated by female (purple) and male (yellow).

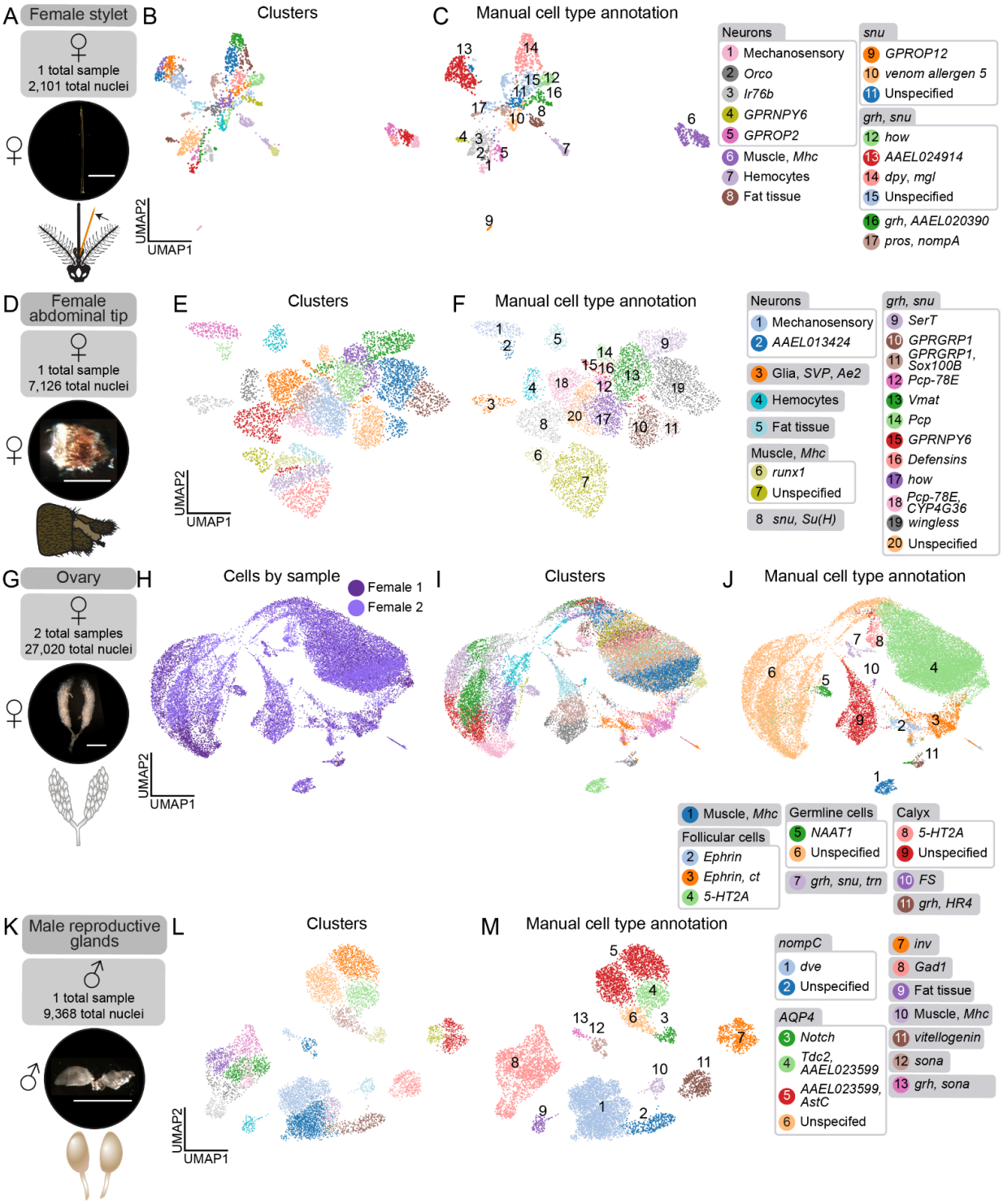
A
Female stylet
1 total sample
2,101 total nuclei
B
Clusters
C
Manual cell type annotation
Neurons
1 Mechanosensory
2 Orco
3 Ir76b
4 GPRNPY6
5 GPROP2
6 Muscle, Mhc
7 Hemocytes
8 Fat tissue
snu
9 GPROP12
10 venom allergen 5
11 Unspecified
grh, snu
12 how
13 AAEL024914
14 dpy, mgl
15 Unspecified
16 grh, AAEL020390
17 pros, nompA
UMAP2
UMAP1
D
Female abdominal tip
1 total sample
7,126 total nuclei
E
Clusters
F
Manual cell type annotation
Neurons
1 Mechanosensory
2 AAEL013424
3 Glia, SVP, Ae2
4 Hemocytes
5 Fat tissue
Muscle, Mhc
6 runx1
7 Unspecified
8 snu, Su(H)
grh, snu
9 SerT
10 GPRGRP1
11 GPRGRP1, Sox100B
12 Pcp-78E
13 Vmat
14 Pcp
15 GPRNPY6
16 Defensins
17 how
18 Pcp-78E, CYP4G36
19 wingless
20 Unspecified
G
Ovary
2 total samples
27,020 total nuclei
H
Cells by sample
Female 1
Female 2
I
Clusters
J
Manual cell type annotation
1 Muscle, Mhc
Follicular cells
2 Ephrin
3 Ephrin, ct
4 5-HT2A
Germline cells
5 NAAT1
6 Unspecified
7 grh, snu, trn
Calyx
8 5-HT2A
9 Unspecified
10 FS
11 grh, HR4
K
Male reproductive glands
1 total sample
9,368 total nuclei
L
Clusters
M
Manual cell type annotation
nompC
1 dve
2 Unspecified
AQP4
3 Notch
4 Tdc2, AAEL023599
5 AAEL023599, AstC
6 Unspecifed
7 inv
8 Gad1
9 Fat tissue
10 Muscle, Mhc
11 vitellogenin
12 sona
13 grh, sona

Figure S13. Annotation of mated, sugar-fed female stylet, female abdominal tip, ovaries and male reproductive glands, related to Figure 1.
(A) Representative photo of mated, sugar-fed female stylet dissection with anatomical diagram (in orange). One sample (10x Genomics library) yielded 2,101 nuclei from 1,747 animals, post-quality control filtering. Scale bar: 500 µm.
(B) UMAP of female stylet nuclei clustered using the Leiden algorithm (resolution = 5) for annotation.
(C) UMAP of nuclei from female stylet sample, colored and numbered by manual annotation using selected marker genes as listed in legend at the right of the figure panel. Categorization of cell type annotations represented by shaded gray headers. See Table S3 and Table S4 for gene IDs and thresholds.
(D) Representative photo of mated, sugar-fed female abdominal tip dissection with anatomical diagram. One sample (10x Genomics library) yielded 7,126 nuclei from 89 animals, post-quality control filtering. Scale bar: 500 µm.
(E) UMAP of female abdominal tip nuclei clustered using the Leiden algorithm (resolution = 5) for annotation.
(F) UMAP of nuclei from female abdominal tip sample, colored and numbered by manual annotation using selected marker genes as listed in legend at the right of the figure panel. Categorization of cell type annotations represented by shaded gray headers. See Table S3 and Table S4 for gene IDs and thresholds.
(G) Representative photo of mated, sugar-fed female ovary dissection with anatomical diagram. Two samples (10x Genomics libraries) yielded 27,020 nuclei from 60 animals, post-quality control filtering. Scale bar: 500 µm.
(H) UMAP of ovary nuclei, colored by sample (female samples = 2)
(I) UMAP of ovary nuclei clustered using the Leiden algorithm (resolution = 5) for annotation.
(J) UMAP of nuclei from ovary samples, colored and numbered by manual annotation using selected marker genes as listed in legend at the bottom of figure panel. Categorization of cell type annotations represented by shaded gray headers. See Table S3 and Table S4 for gene IDs and thresholds.
(K) Representative photo of mated, sugar-fed male reproductive gland dissection with anatomical diagram. One sample (10x Genomics library) yielded 9,368 nuclei from 264 animals, post-quality control filtering. Scale bar: 500 µm.
(L) UMAP of male reproductive gland nuclei clustered using the Leiden algorithm (resolution = 5) for annotation.
(M) UMAP of nuclei from male reproductive gland sample, colored and numbered by manual annotation using selected marker genes as listed in legend at the right of the figure panel. Categorization of cell type annotations represented by shaded gray headers. See Table S3 and Table S4 for gene IDs and thresholds.

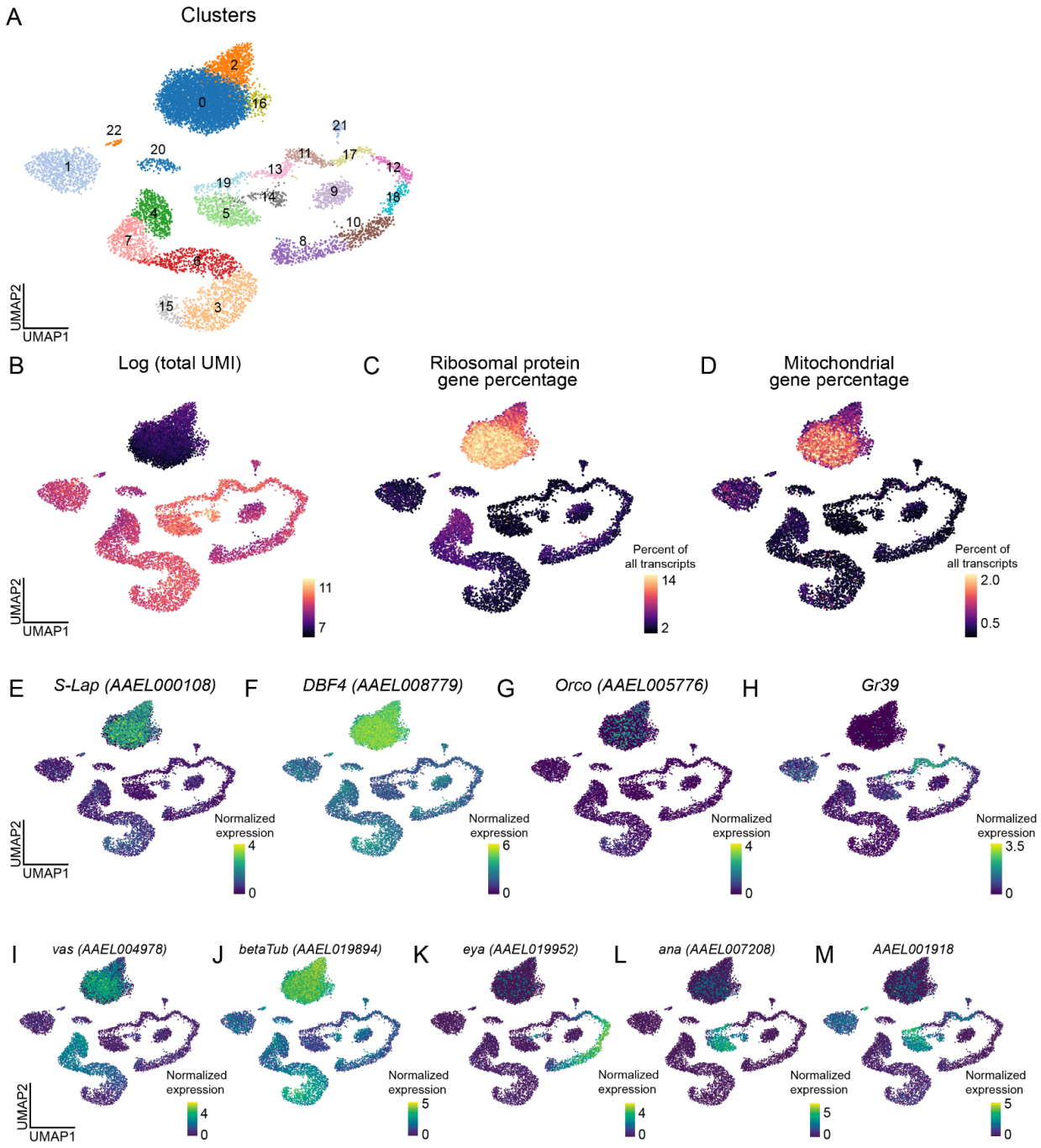

Figure S14. Localization of spermatid RNA transcripts in mated, sugar-fed testes data, related to Figure 2.

(A) UMAP of all testes cells after quality control and filtering (Louvain algorithm, resolution = 1).

(B) UMAP of testes cells colored by log total UMI for each cell.

(C-D) UMAP of testes sample colored by percent of all transcripts in each cell for expression of ribosomal protein genes (C), expression of mitochondrial genes (D). Each end of color bars trimmed 0.5% for visibility.
(E-H) UMAPs of testes normalized expression of *S-Lap* (*AAEL000108*) (E), *DBF4* (*AAEL008779*) (F), *Orco* (*AAEL005776*) (G), and *Gr39* (H).Normalized expression is ln([(raw count/total cell counts)x median total counts across cells]+1).
(I-M) UMAP of normalized gene expression of a subset of genes used to annotate testes data that were used in Figure 2C-2G. Genes include include *vas* (*AAEL004978*) (I), *betaTub* (*AAEL019894*) (J), *eya (AAEL019952*) (K), *ana (AAEL007208)* (L), and *AAEL001918* (M). Note normalized signal of genes expressed in spermatids appears high relative to other cell types in normalized expression due to their overall low transcript count (Figure S14B).

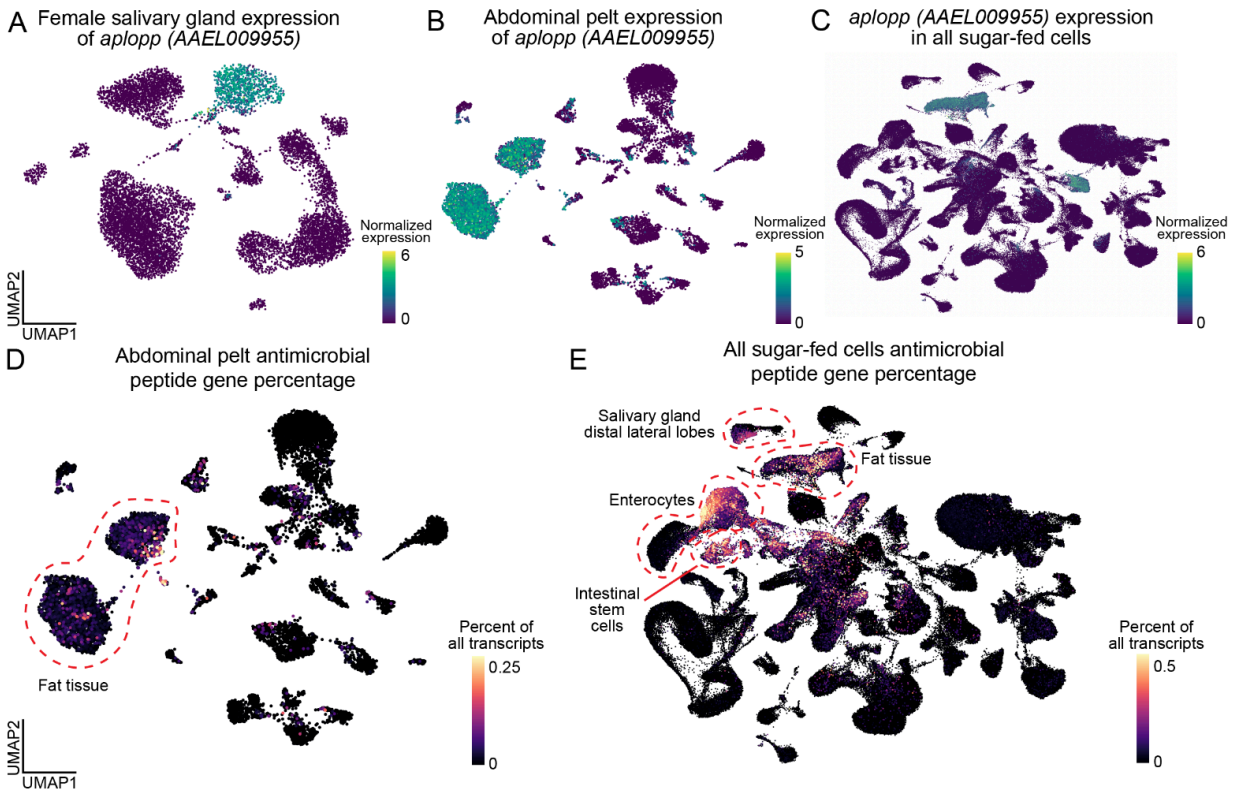

Figure S15. Antimicrobial genes in fat tissue, related to Figure 3.
(A-C) UMAPs of normalized expression of marker gene for fat tissue *aplopp* (*AAEL009955*) in the salivary gland (A), abdominal pelt (B), and all mated, sugar-fed nuclei (C). Normalized expression is ln([(raw count/total cell counts)x median total counts across cells]+1).
(D-E) UMAP, colored by expression of antimicrobial peptides gene set (Table S2) for abdominal pelt (D) and all sugar-fed nuclei (E). Color represents fraction of total transcripts in each cell (each end of color bar trimmed 0.1% for visibility). Relevant cell types labeled.

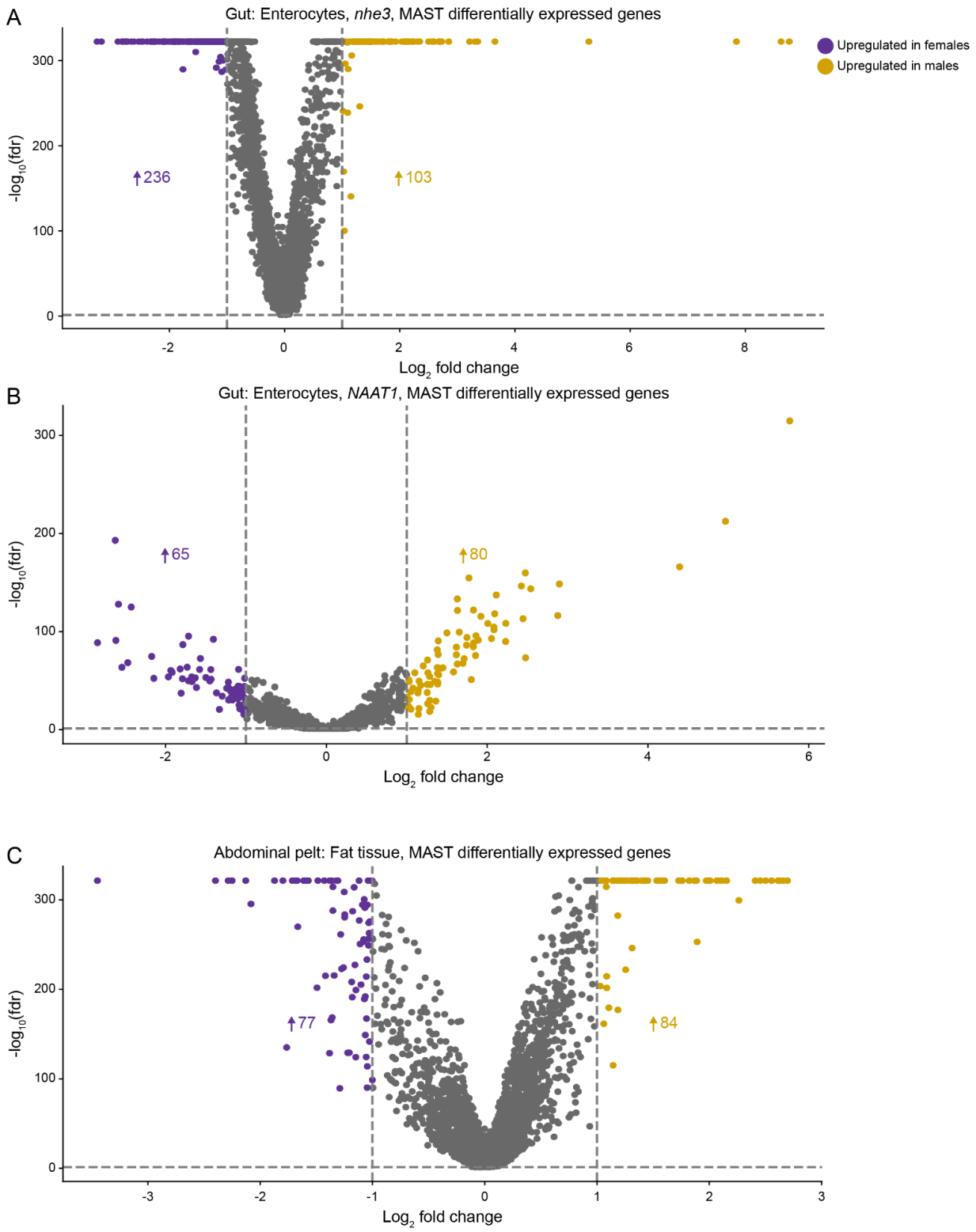
A
Gut: Enterocytes, nhe3, MAST differentially expressed genes
Upregulated in females
Upregulated in males
236
103
-log10(fdr)
Log2 fold change
B
Gut: Enterocytes, NAAT1, MAST differentially expressed genes
65
80
-log10(fdr)
Log2 fold change
C
Abdominal pelt: Fat tissue, MAST differentially expressed genes
77
84
-log10(fdr)
Log2 fold change

Figure S16. Sexually differential expressed genes in gut enterocytes and abdominal pelt fat tissue, related to Figures 1 and 3.

(A-C) Volcano plots of sexually differential expressed genes (DEGs) between males and females in the gut enterocytes, "*nhe3*" cell type (A) gut enterocytes, "*NAAT1*" cell type (B), and abdominal pelt fat tissue (C). All significantly upregulated genes in females (indicated in purple) and all significantly upregulated genes in males (indicated in yellow) are |log fold change| > 1 and false discovery rate < 0.05, determined by MAST on normalized expression. Number of upregulated genes in females (purple) and upregulated genes in males (yellow) genes are indicated by the up arrows. For more information on DEGs, see Table S13.

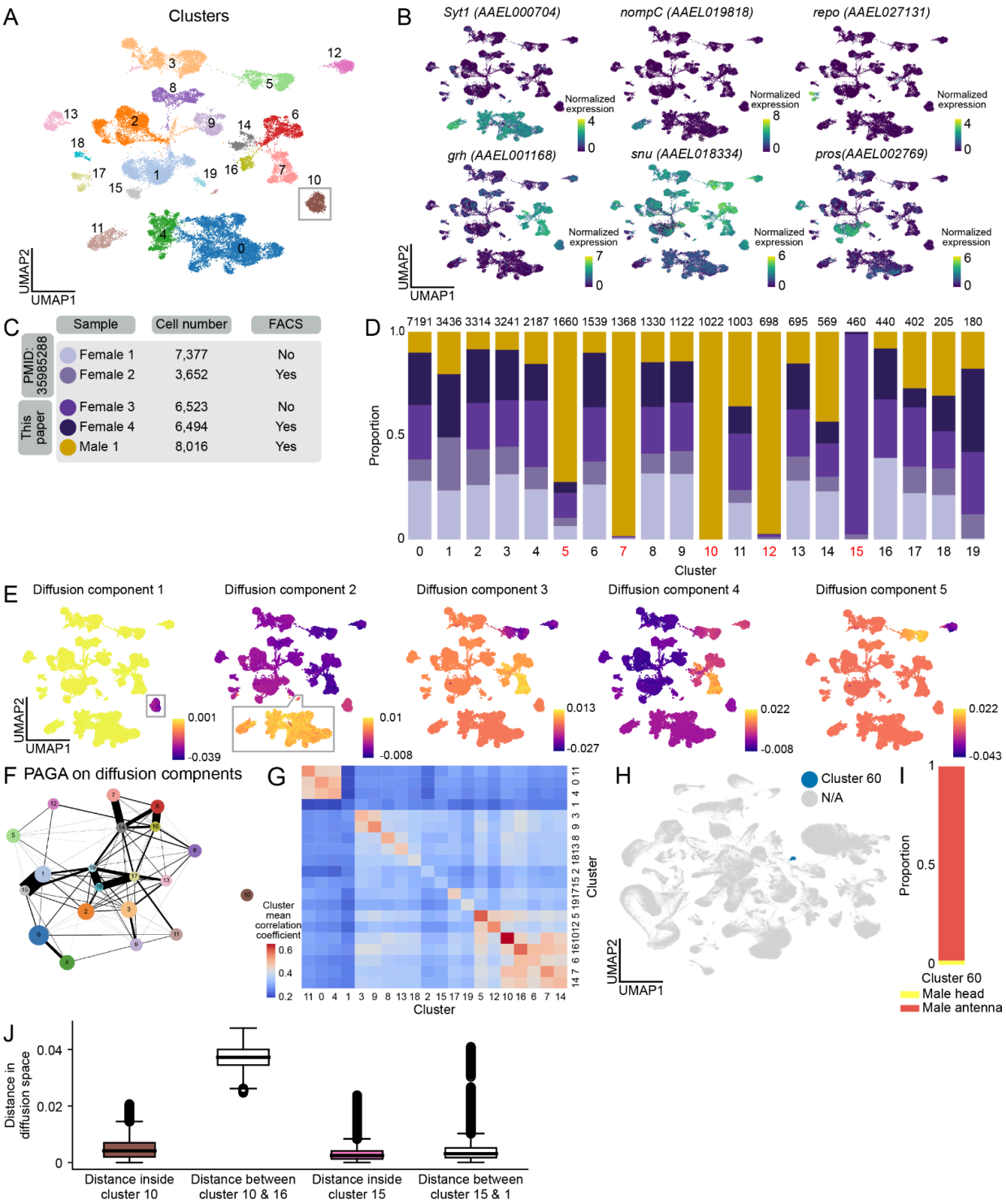
A
Clusters
UMAP2
UMAP1
B
Syt1 (AAEL000704)
nompC (AAEL019818)
repo (AAEL027131)
grh (AAEL001168)
snu (AAEL018334)
pros(AAEL002769)
Normalized expression
C
Sample
Cell number
FACS
PMID: 35985288
Female 1 7,377 No
Female 2 3,652 Yes
This paper
Female 3 6,523 No
Female 4 6,494 Yes
Male 1 8,016 Yes
D
Proportion
Cluster
E
Diffusion component 1
Diffusion component 2
Diffusion component 3
Diffusion component 4
Diffusion component 5
F PAGA on diffusion compnents
G
Cluster mean correlation coefficient
Cluster
H
Cluster 60
N/A
I
Proportion
Cluster 60
Male head
Male antenna
J
Distance in diffusion space
Distance inside cluster 10
Distance between cluster 10 & 16
Distance inside cluster 15
Distance between cluster 15 & 1

Figure S17. Identification of male-specific *ppk317* cell type in *Aedes aegypti* antenna, related to Figure 4.

(A) UMAP of antenna nuclei clustered and numbered using the Leiden algorithm (resolution = 0.1). Cluster 10 (male-specific, *ppk317*-expressing cells) highlighted in grey.

(B) UMAPs of all antenna nuclei colored by normalized expression of *Syt1 (AAEL000704), nompC (AAEL019818), repo (AAEL027131), grh (AAEL001168), snu (AAEL018334),* and *pros (AAEL002769)*. Normalized expression is ln([(raw count/total cell counts)x median total counts across cells]+1).

(C) Number of cells in each sample (female = 4, male = 1), source, and if each sample underwent fluorescence-activated cell sorting.

(D) Bar plot of proportion that each sample makes up each cluster based on numbering from (A). Cluster numbers below bar plot. Clusters for which over 70% originate form a single sample indicated in red. Numbers above each bar indicate the number of cells in that cluster.

(E) UMAPs of diffusion components 1-5. Diffusion component 1 (first panel) maps to cluster 10 (*ppk317*-expressing cells, circled in red), suggesting a robust biological feature. Diffusion component 2 (second panel) maps to neurons, highlighted in grey.

(F) Partition-based graph abstraction (PAGA) calculated on diffusion components in (E). No edge threshold set.

(G) Correlation matrix heatmap, depicting pairwise correlation of gene expression matrices between each cluster (mean Pearson correlation coefficient). Diagonal values (cluster to itself) represents intra-cluster correlation values, which vary based on features such as cell number and gene heterogeneity.

(H) UMAP of integrated *Aedes aegypti* Mosquito Cell Atlas data. Antennal cells expressing *ppk317* belong to cluster 60 (Louvain algorithm, resolution = 0.1).

(I) Stacked bar plot of origin of cells from cluster 60. Cluster 60 (all *ppk317*-expressing cells in the male and female mosquito) come from the male antenna and male head sample.

(J) Pairwise Euclidean distances on diffusion embeddings from (E) to approximate phenotypic distance between and within clusters. Boxes represent first quartile to third quartile, and middle line represents median. Whiskers represent the 1.5x interquartile range of the data, with points outside this range as outliers.

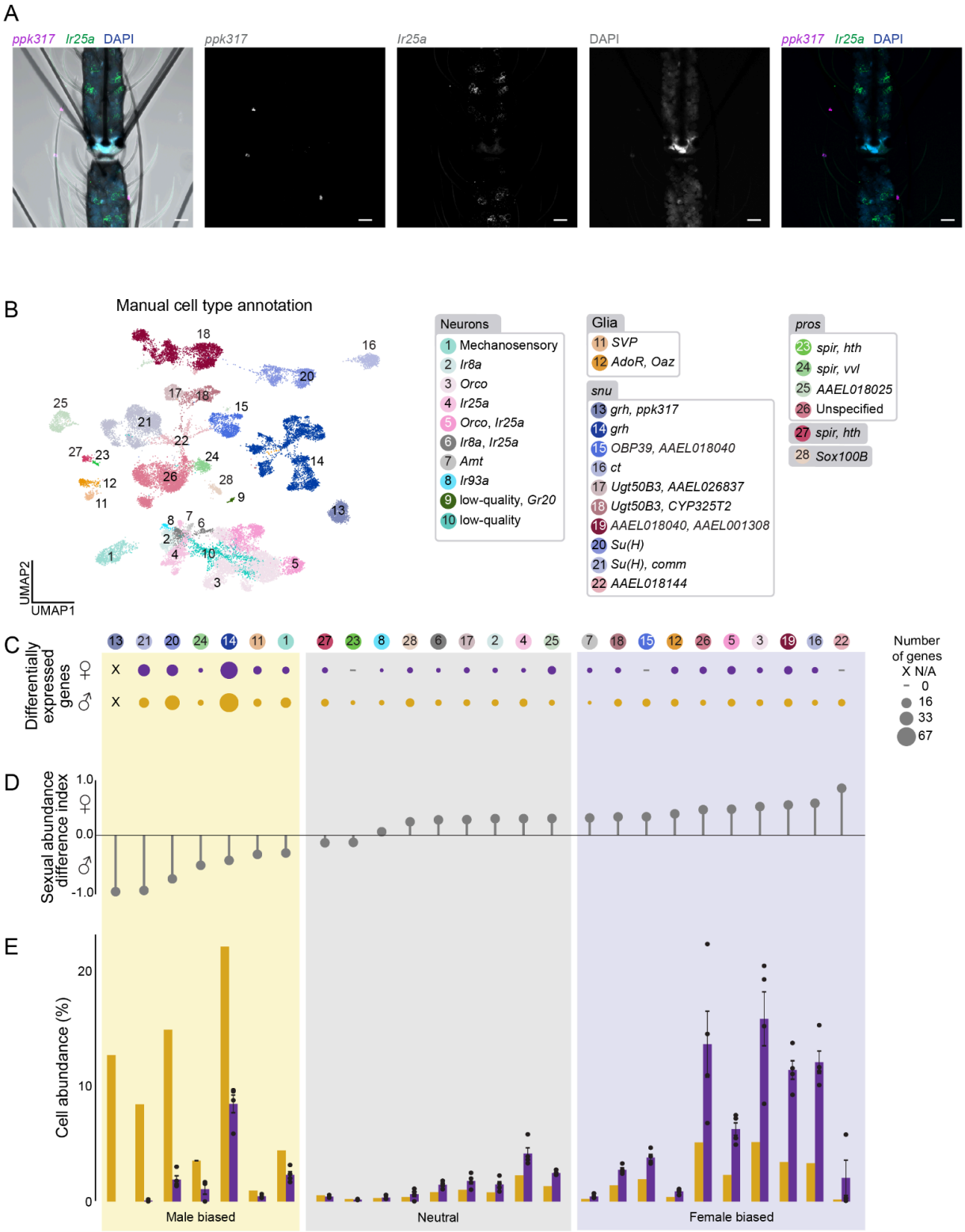
A
ppk317 Ir25a DAPI
ppk317
Ir25a
DAPI
ppk317 Ir25a DAPI
B
Manual cell type annotation
UMAP2
UMAP1
Neurons
1 Mechanosensory
2 Ir8a
3 Orco
4 Ir25a
5 Orco, Ir25a
6 Ir8a, Ir25a
7 Amt
8 Ir93a
9 low-quality, Gr20
10 low-quality
Glia
11 SVP
12 AdoR, Oaz
snu
13 grh, ppk317
14 grh
15 OBP39, AAEL018040
16 ct
17 Ugt50B3, AAEL026837
18 Ugt50B3, CYP325T2
19 AAEL018040, AAEL001308
20 Su(H)
21 Su(H), comm
22 AAEL018144
pros
23 spir, hth
24 spir, vvl
25 AAEL018025
26 Unspecified
27 spir, hth
28 Sox100B
C
Differentially expressed genes
♀
♂
Number of genes
X N/A
0
16
33
67
D
Sexual abundance difference index
1.0
0.0
-1.0
E
Cell abundance (%)
20
10
0
Male biased
Neutral
Female biased

Figure S18. Antennae samples and annotation, related to Figures 1 and 4.
(A) Maximum-intensity projection of whole-mount female antennae with RNA *in situ* hybridization of *ppk317* probe (magenta), *Ir25a* (green) and nuclear staining (DAPI). Scale bar: 10 μm.
(B) UMAP of nuclei from all antennae samples, colored and numbered by manual annotation using selected marker genes as listed in legend at the right of the figure panel. Categorization of cell type annotations represented by shaded gray headers. See Table S3 and Table S4 for gene IDs and thresholds.
(C-E) Quantification of differences between male and female samples. Numbered and colored circles above (C) correspond to annotations in (B).
(C) Dot plot of number of differentially expressed genes between females and males in each cell type. Dots represent relative number of differentially expressed genes upregulated in male or female with a |log fold change| > 1 and false discovery rate < 0.05, determined by MAST on normalized expression and converted to $\log_2$ fold change.
(D) Sexual abundance difference index from data in (G). Each cell type was categorized based on the following index: Female biased (purple) if 0.3 < abundance index; Neutral (grey) if -0.3 ≤ abundance index ≤ 0.3; Male biased (yellow) if abundance index < -0.3.
(E) Bar plot of relative cell abundance, represented as the percent of each cell type of all nuclei collected from each sex for tissue. Separated by female (purple) and male (yellow). Values for each replicate shown as dots, and standard error indicated by black brackets.

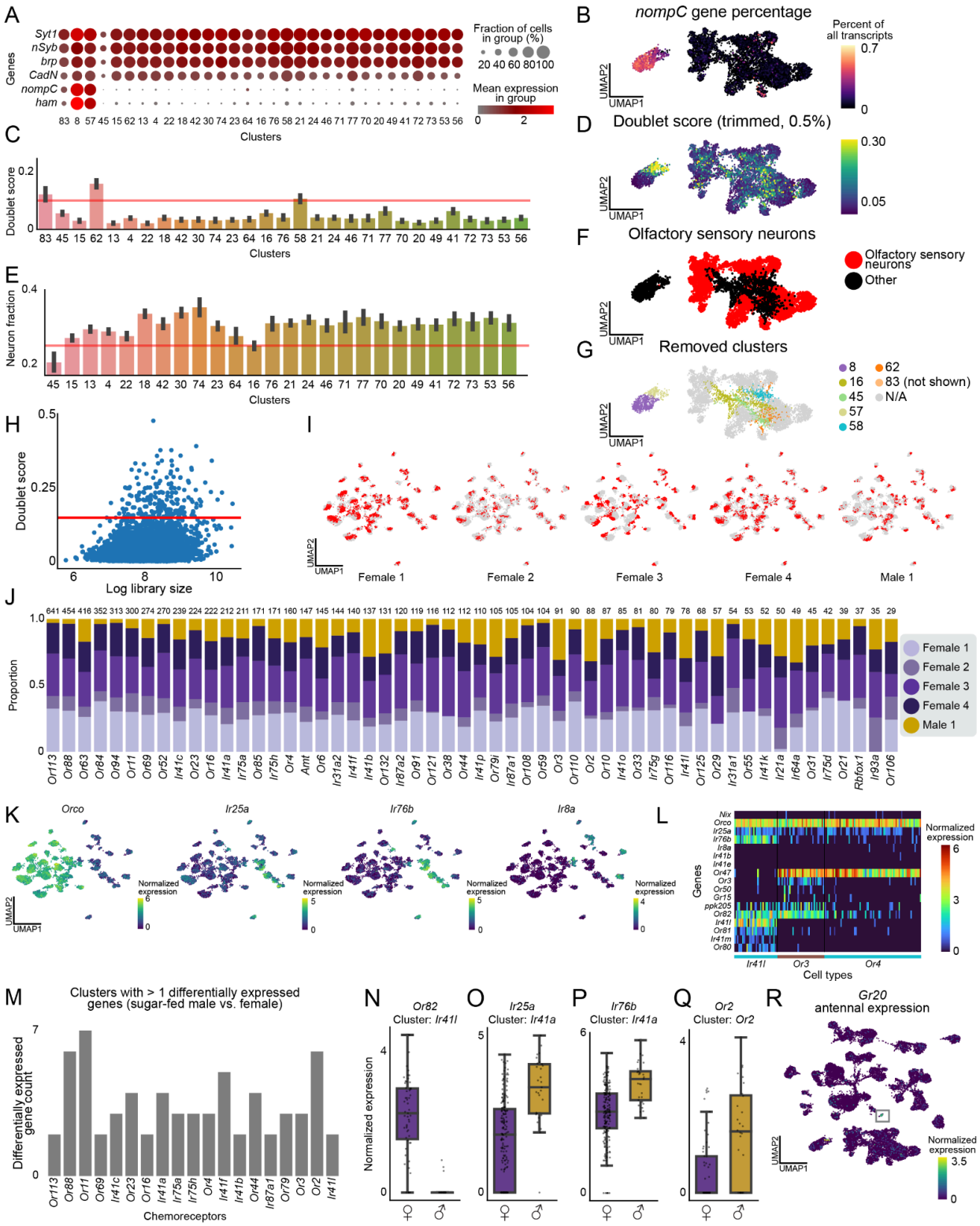

Figure S19. Antenna chemosensory cell type expressing *Orco* and *Ir25a* is sexually dimorphic for *Or82,* related to Figure 5.

(A) Dotplot of neuron marker genes (*Syt1 (AAEL000704), nSyb (AAEL024921), brp (AAEL018153), CadN (AAEL000597), nompC (AAEL019818),* and *ham (AAEL017229)*). Size of dot indicated the percent of cells in each group, color indicated mean expression, see legend in the lower right of the panel.
(B) UMAP of neurons from antenna samples with expression of *nompC* as percent of all transcripts in each cell. UMAPs for (B,D,F,G) in this figure UMAP coordinates of neurons from Figure 5A.
(C) Mean doublet score across cells, with error bars indicating 95% confidence interval calculated from bootstrapping. Generated through scrublet[197]. Clusters with an average score above 0.15 were removed from further analysis (red line).
(D) UMAP of neurons from antenna samples depicting doublet score.
(E) Average percentage of neuronal genes in (A), with error bars indicating 95% confidence interval calculated from bootstrapping. Clusters with an average score below 0.25 were removed from further analysis (red line).
(F) UMAP of neurons from antenna samples, demonstrating which clusters (Leiden, resolution = 5) were kept for downstream analysis (red) or removed based on filtering parameters (black).
(G) UMAP of neurons from antenna samples, demonstrating clusters removed from downstream analysis. UMAP cropped for space, cluster 83 not shown.
(H) Log(library size) versus calculated doublet score for neurons filtered in (A-G). Cells with a score above 0.15 were removed from further analysis (red line).
(I) UMAPs of antenna olfactory sensory neurons (filtered *nompC*-negative sensory neuron population), colored by sample.
(J) Proportion plot for annotated *nompC*-negative sensory neuron population. Bar plot of proportion that each sample makes up each cell type. Numbers above each bar indicate the number of cells in that cluster.
(K) UMAP of normalized gene expression of olfactory co-receptor genes *Orco, Ir25a, Ir76b,* and *Ir8a*. Normalized expression is ln([(raw count/total cell counts)x median total counts across cells]+1).
(L) Heatmap of cells from female samples 3 and 4 (see Figure S17C) from annotated clusters *Ir41l*, *Or3*, and *Or4*. Selected genes are indicated in rows and cells indicated in columns. Cell types indicated below heatmap. Heatmap colors represent normalized expression.
(M) Bar plot of number of differentially expressed genes (DEGs) between females and males in each olfactory sensory neuron cell type. Clusters shown contain at least 1 DEG with a |log fold change| > 1 and false discovery rate < 0.05 (determined by MAST on normalized expression). For more information on DEGs, see Table S5.
(N-Q) Boxplot illustrating distribution of gene expression of differentially expressed olfactory receptor genes across male and female cells in a particular cluster. *Or82* expression in cluster *Ir41l* (N), *Ir25a* in cluster *Ir41a* (O), *Ir76b* in cluster *Ir41a* (P), *Or2* expression in cluster *Or2* (Q). Boxes represent first quartile to third quartile, and middle line represents median. Whiskers represent the 1.5x interquartile range of the data, with points outside this range as outliers.
(R) UMAP of normalized gene expression of *Gr20*. *Gr20* positive antennal cluster highlighted in grey.

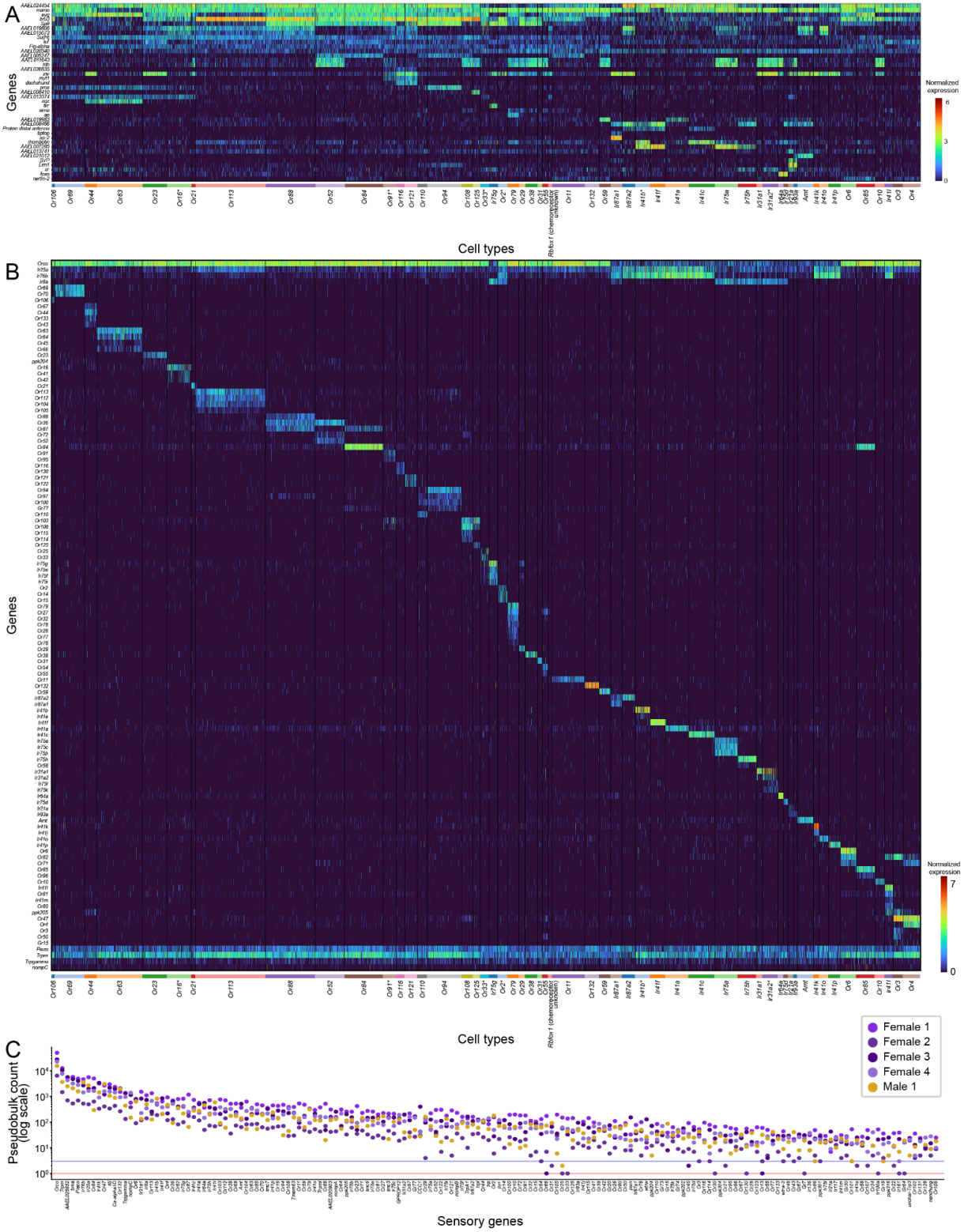
A
Genes
Normalized expression
Cell types
B
Genes
Normalized expression
Cell types
C
Pseudobulk count (log scale)
Female 1
Female 2
Female 3
Female 4
Male 1
Sensory genes

Figure S20. Antenna chemosensory neuron chemoreceptor and putative transcription factor factor expression profiles, related to Figure 5.
(A-B) Heatmap of genes expressed across all antenna olfactory sensory neurons (*nompC*-negative) for putative selected transcription factors (A) and selected sensory genes (B). Selected genes are indicated in rows and cells indicated in columns. Cells are grouped by annotation in Figure 5C and indicated below heatmap. Asterisks (*) on cell type annotation indicates that a group may represent a co-clustering of cells with multiple unique sensory gene expression patterns, as depicted in Figure 5C-5D. Heatmap colors represent normalized expression. Normalized expression is ln([(raw count/total cell counts)x median total counts across cells]+1).
(C) Scatterplot of summed raw counts of sensory genes within all olfactory sensory neurons within each antenna sample. Red line indicates count of 1, blue line is a count of 5. For a complete look up table of gene symbols to gene IDs used in this manuscript, see Table S3. 158 out of 403 putative sensory genes (Table S4) with the highest counts shown for space (full plot available in Zenodo Supplemental Data).

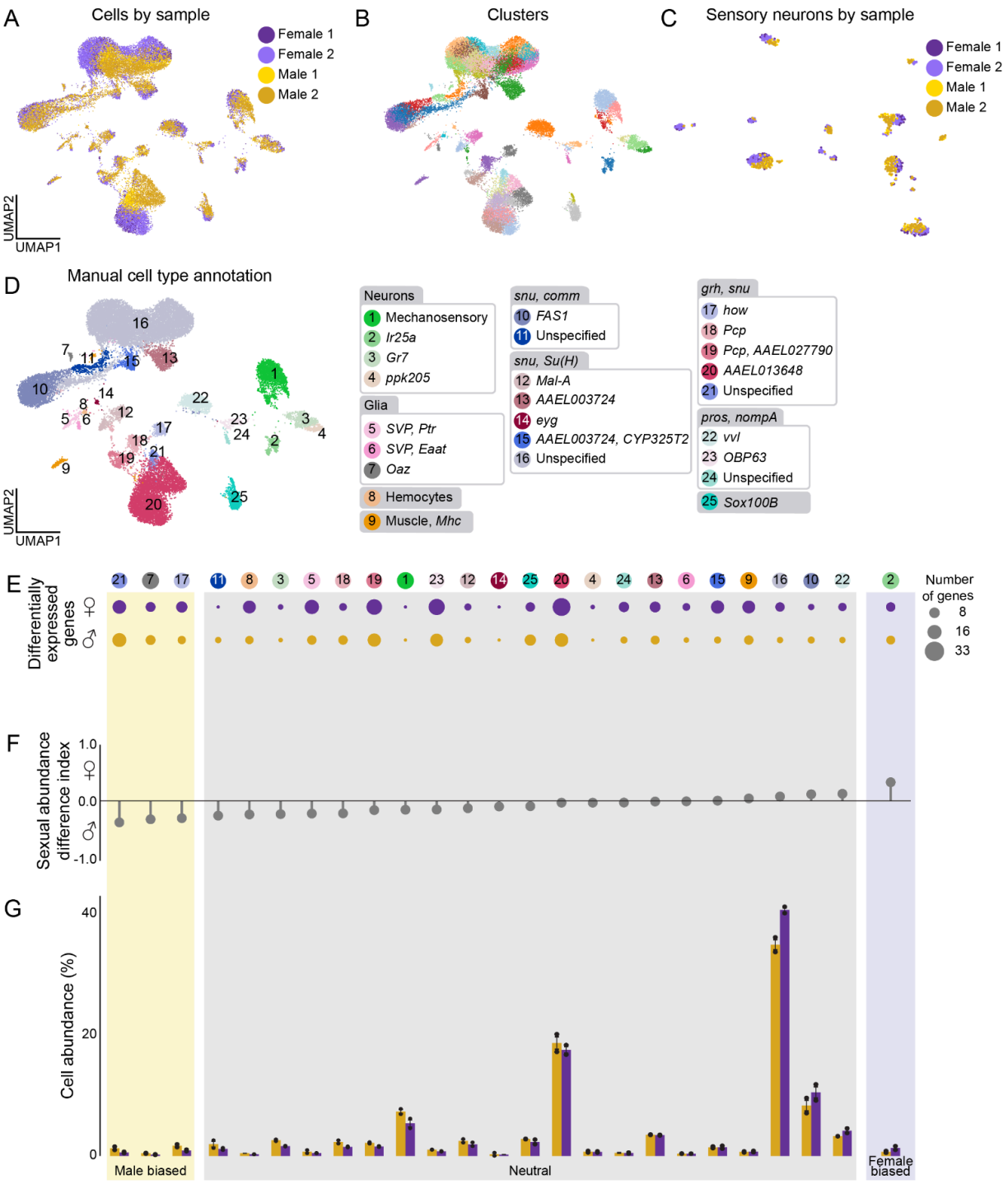
A
Cells by sample
Female 1
Female 2
Male 1
Male 2
UMAP2
UMAP1
B
Clusters
C
Sensory neurons by sample
Female 1
Female 2
Male 1
Male 2
D
Manual cell type annotation
Neurons
1 Mechanosensory
2 Ir25a
3 Gr7
4 ppk205
Glia
5 SVP, Ptr
6 SVP, Eaat
7 Oaz
8 Hemocytes
9 Muscle, Mhc
snu, comm
10 FAS1
11 Unspecified
snu, Su(H)
12 Mal-A
13 AAEL003724
14 eyg
15 AAEL003724, CYP325T2
16 Unspecified
grh, snu
17 how
18 Pcp
19 Pcp, AAEL027790
20 AAEL013648
21 Unspecified
pros, nompA
22 vvl
23 OBP63
24 Unspecified
25 Sox100B
E
Differentially expressed genes
Number of genes
8
16
33
F
Sexual abundance difference index
1.0
0.0
-1.0
G
Cell abundance (%)
40
20
0
Male biased
Neutral
Female biased

Figure S21. Tarsi samples and annotation, related to Figures 1, 5 and 6.
(A) UMAP of tarsi nuclei, colored by sample (female samples = 2, male samples = 2)
(B) UMAP of tarsi nuclei clustered using the Leiden algorithm (resolution = 5).
(C) UMAP of *nompC*-negative tarsi sensory neuron nuclei, colored by sample (female samples = 2, male samples = 2), related to Figure 6C.
(D) UMAP of nuclei from all tarsi samples, colored and numbered by manual annotation using selected marker genes as listed in legend at the right of the figure panel. Categorization of cell type annotations represented by shaded gray headers. See Table S3 and Table S4 for gene IDs and thresholds.
(E-G) Quantification of differences between male and female samples. Numbered and colored circles above (E) correspond to annotations in (D).
(E) Dot plot of number of differentially expressed genes between females and males in each cell type. Dots represent relative number of differentially expressed genes upregulated in male or female with a |log fold change| > 1 and false discovery rate < 0.05, determined by MAST on normalized expression and converted to $\log_2$ fold change.
(F) Sexual abundance difference index from data in (G). Each cell type was categorized based on the following index: Female biased (purple) if 0.3 < abundance index; Neutral (grey) if -0.3 ≤ abundance index ≤ 0.3; Male biased (yellow) if abundance index < -0.3.
(G) Bar plot of relative cell abundance, represented as the percent of each cell type of all nuclei collected from each sex for tissue. Separated by female (purple) and male (yellow). Values for each replicate are shown as dots, and standard error indicated by black brackets.

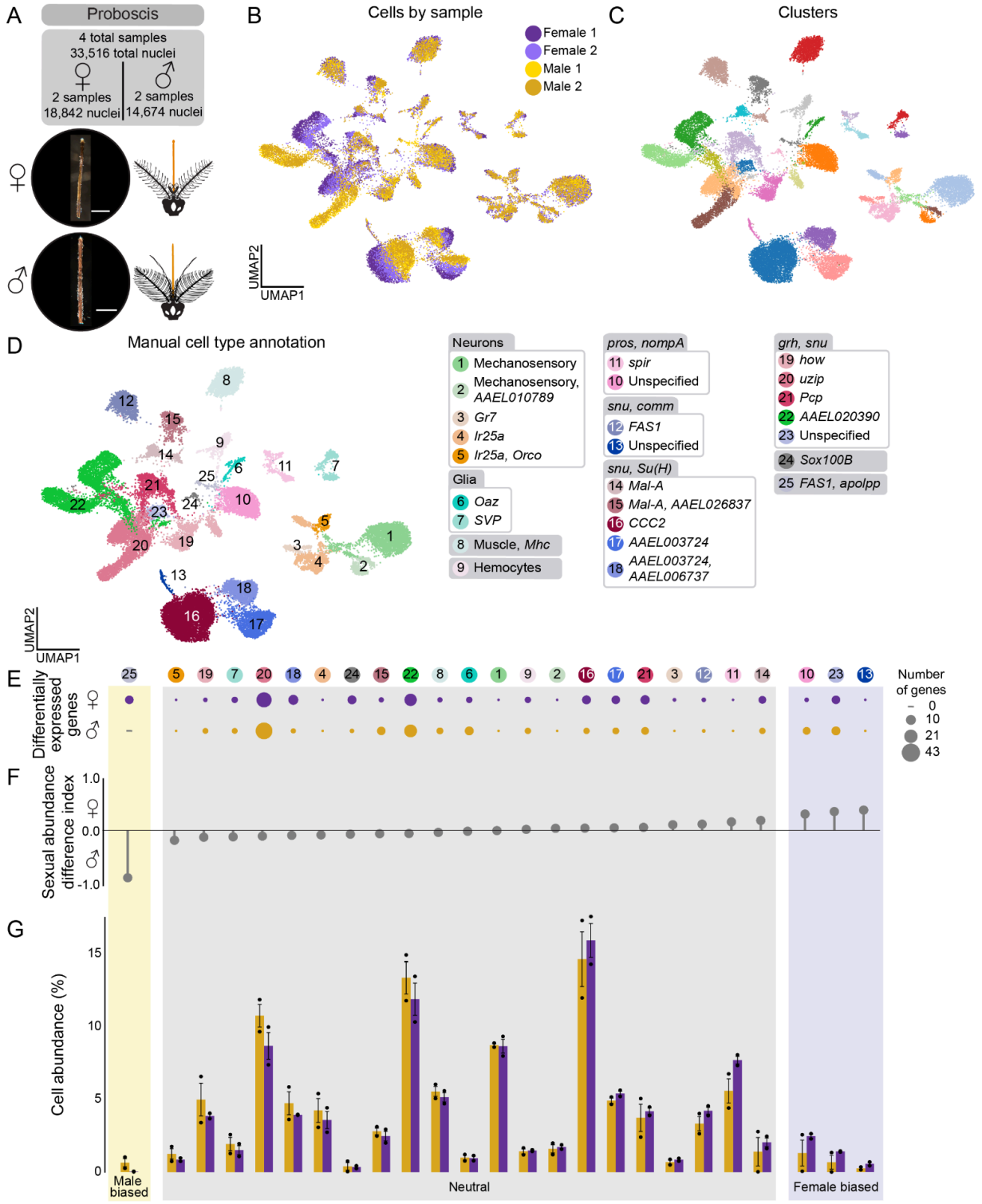
A
Proboscis
4 total samples
33,516 total nuclei
2 samples
18,842 nuclei
2 samples
14,674 nuclei
B
Cells by sample
Female 1
Female 2
Male 1
Male 2
UMAP2
UMAP1
C
Clusters
D
Manual cell type annotation
Neurons
1 Mechanosensory
2 Mechanosensory, AAEL010789
3 Gr7
4 Ir25a
5 Ir25a, Orco
Glia
6 Oaz
7 SVP
8 Muscle, Mhc
9 Hemocytes
pros, nompA
11 spir
10 Unspecified
snu, comm
12 FAS1
13 Unspecified
snu, Su(H)
14 Mal-A
15 Mal-A, AAEL026837
16 CCC2
17 AAEL003724
18 AAEL003724, AAEL006737
grh, snu
19 how
20 uzip
21 Pcp
22 AAEL020390
23 Unspecified
24 Sox100B
25 FAS1, apolpp
E
Differentially expressed genes
Number of genes
0
10
21
43
F
Sexual abundance difference index
1.0
0.0
-1.0
G
Cell abundance (%)
Male biased
Neutral
Female biased

Figure S22. Proboscis samples and annotation, related to Figures 1, 5 and 6.
(A) Representative photo of mated, sugar-fed female (top) and male (bottom) proboscis dissection with anatomical diagram (in orange). Four samples (10x Genomics libraries) yielded 33,516 nuclei from 800 animals, post-quality control filtering. Scale bar: 500 µm.
(B) UMAP of proboscis nuclei, colored by sample (female samples = 2, male samples = 2)
(C) UMAP of proboscis nuclei clustered using the Louvain algorithm (resolution = 1).
(D) UMAP of nuclei from all proboscis samples, colored and numbered by manual annotation using selected marker genes as listed in legend at the right of the figure panel. Categorization of cell type annotations represented by shaded gray headers. See Table S3 and Table S4 for gene IDs and thresholds.
(E-G) Quantification of differences between male and female samples. Numbered and colored circles above (E) correspond to annotations in (D).
(E) Dot plot of number of differentially expressed genes between females and males in each cell type. Dots represent relative number of differentially expressed genes upregulated in male or female with a |log fold change| > 1 and false discovery rate < 0.05, determined by MAST on normalized expression and converted to $\log_2$ fold change.
(F) Sexual abundance difference index from data in (G). Each cell type was categorized based on the following index: Female biased (purple) if 0.3 < abundance index; Neutral (grey) if -0.3 ≤ abundance index ≤ 0.3; Male biased (yellow) if abundance index < -0.3.
(G) Bar plot of relative cell abundance, represented as the percent of each cell type of all nuclei collected from each sex for tissue. Separated by female (purple) and male (yellow). Values for each replicate shown as dots, and standard error indicated by black brackets.

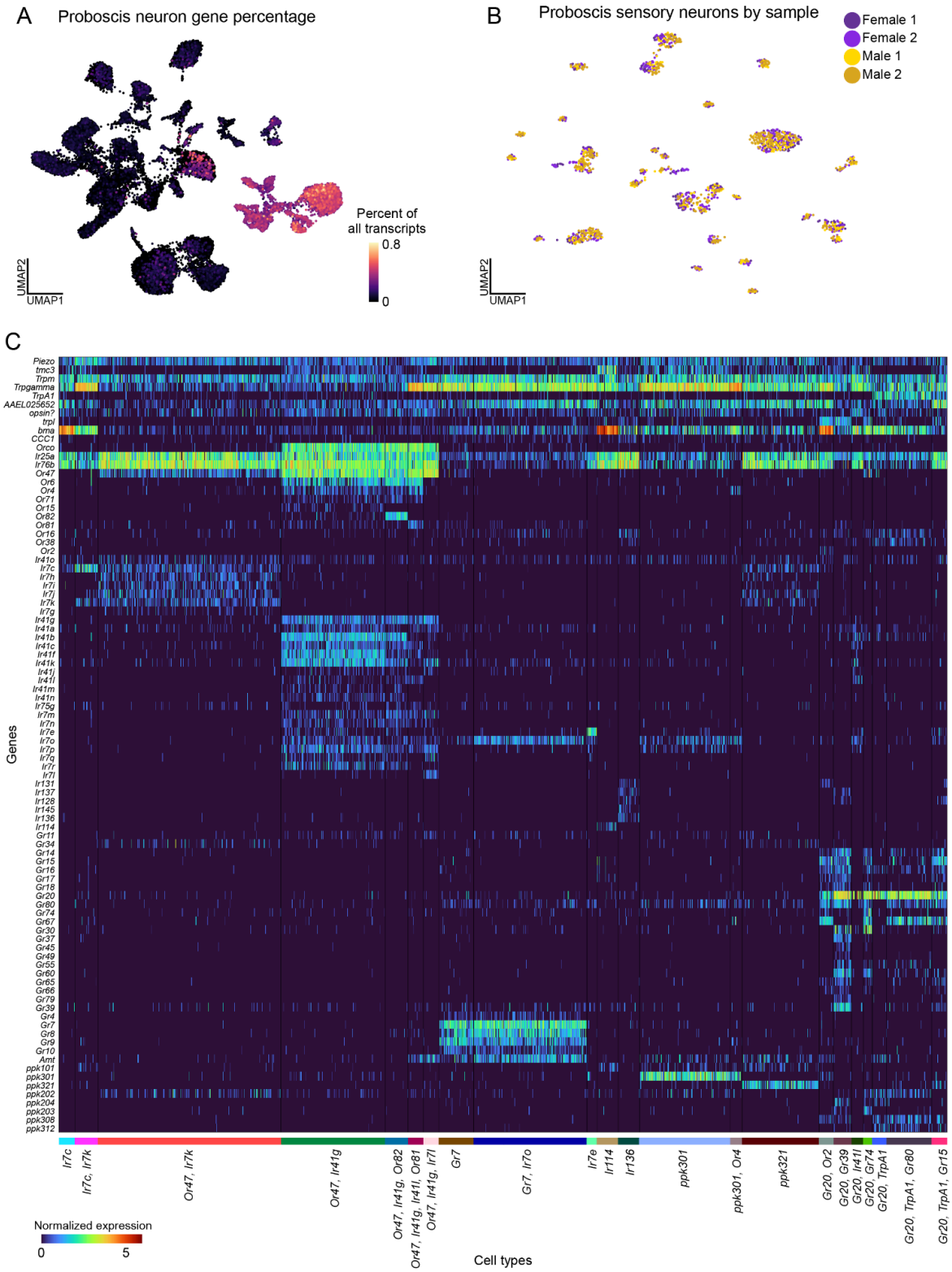
A
Proboscis neuron gene percentage
Percent of all transcripts
0.8
0
UMAP2
UMAP1
B
Proboscis sensory neurons by sample
Female 1
Female 2
Male 1
Male 2
UMAP2
UMAP1
C
Genes
Piezo
tmc3
Trpm
Trpgamma
TrpA1
AAEL025652
opsin7
trpl
brna
CCC1
Orco
Ir25a
Ir76b
Or47
Or6
Or4
Or71
Or15
Or82
Or81
Or16
Or38
Or2
Ir41o
Ir7c
Ir7h
Ir7j
Ir7j
Ir7k
Ir7g
Ir41g
Ir41a
Ir41b
Ir41c
Ir41f
Ir41k
Ir41j
Ir41l
Ir41m
Ir41n
Ir75g
Ir7m
Ir7n
Ir7e
Ir7o
Ir7p
Ir7q
Ir7r
Ir7l
Ir131
Ir137
Ir128
Ir145
Ir136
Ir114
Gr11
Gr34
Gr14
Gr15
Gr16
Gr17
Gr18
Gr20
Gr80
Gr74
Gr67
Gr30
Gr37
Gr45
Gr49
Gr55
Gr60
Gr65
Gr66
Gr79
Gr39
Gr4
Gr7
Gr8
Gr9
Gr10
Amt
ppk101
ppk301
ppk321
ppk202
ppk204
ppk203
ppk308
ppk312
Ir7c
Ir7c, Ir7k
Or47, Ir7k
Or47, Ir41g
Or47, Ir41g, Or82
Or47, Ir41g, Ir41l, Or81
Or47, Ir41g, Ir7l
Gr7
Gr7, Ir7o
Ir7e
Ir114
Ir136
ppk301
ppk301, Or4
ppk321
Gr20, Or2
Gr20, Gr39
Gr20, Ir41l
Gr20, Gr74
Gr20, TrpA1
Gr20, TrpA1, Gr80
Gr20, TrpA1, Gr15
Normalized expression
0
5
Cell types

Figure S23. Proboscis sensory gene analysis, related to Figures 5 and 6.
(A) UMAP of all proboscis cells with expression of neuron marker genes (*Syt1 (AAEL000704), nSyb (AAEL024921), brp (AAEL018153), CadN (AAEL000597)* as percent of all transcripts in each cell. For *nompC* gene percentage, see Figure S24B.
(B) UMAP of reclustered sensory cells colored by sample (female = 2, male = 2).
(C) Heatmap of cells from all annotated clusters. Sensory genes are indicated in rows and cells indicated in columns. Cell types indicated below heatmap and respective sensory function indicated above. Heatmap colors represent normalized expression. Normalized expression is ln([(raw count/total cell counts)x median total counts across cells]+1).

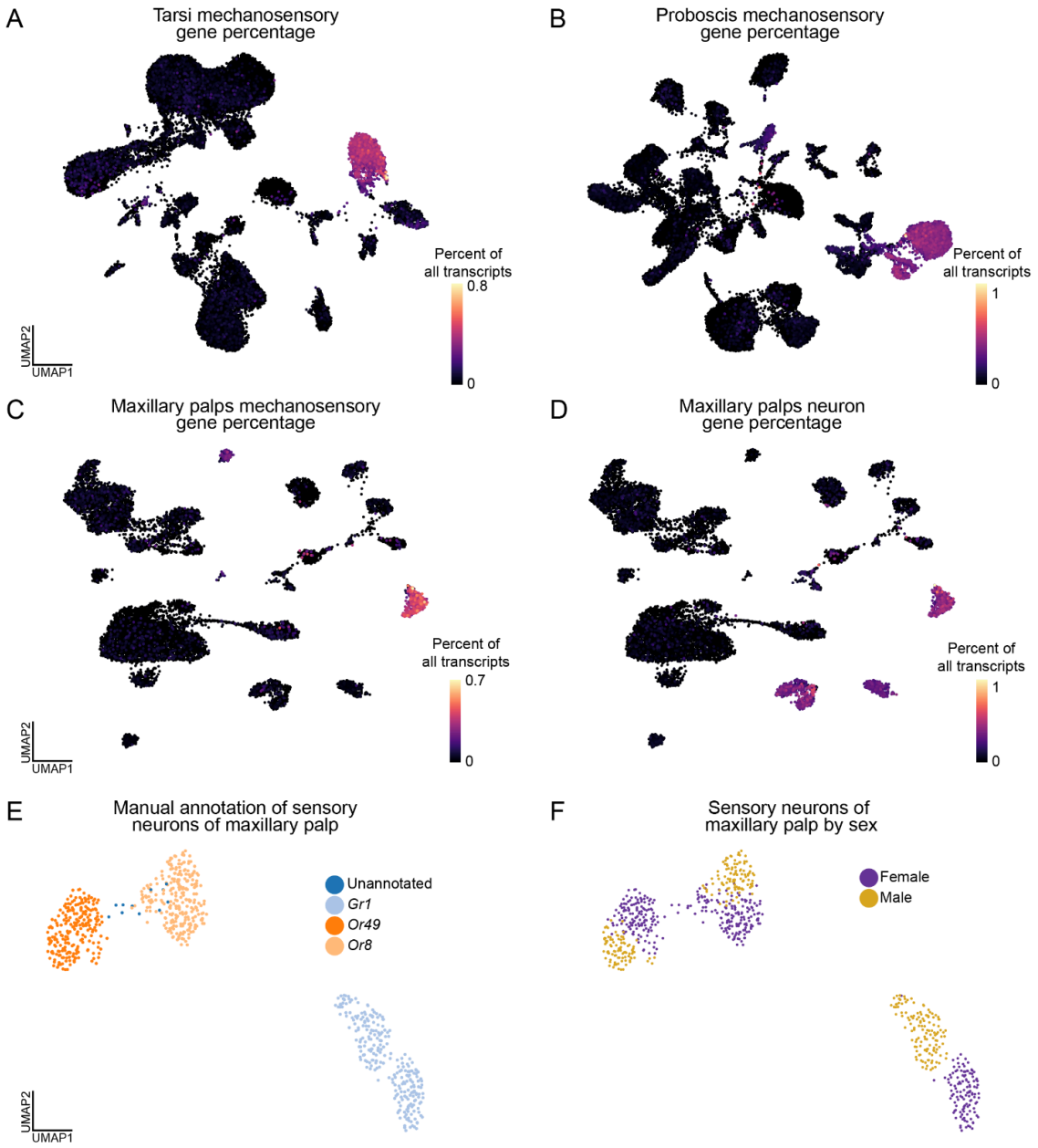

Figure S24. Sensory neuron filtering and analysis, related to Figures 5 and 6.
(A-C) UMAP of neurons from tarsi (A), proboscis (B), and maxillary palps (C) data with expression of *nompC* (*AAEL019818*) as percent of all transcripts in each cell.
(D) UMAP of all maxillary palp cells with expression of neuron marker genes (*Syt1 (AAEL000704), nSyb (AAEL024921), brp (AAEL018153), CadN (AAEL000597)*) as percent of all transcripts in each cell.
(E-F) UMAP of *nompC*-negative sensory neurons from maxillary palps, colored by manual annotation (E) and sample (F) (female = 1, male = 1). Female sample previously published[36].

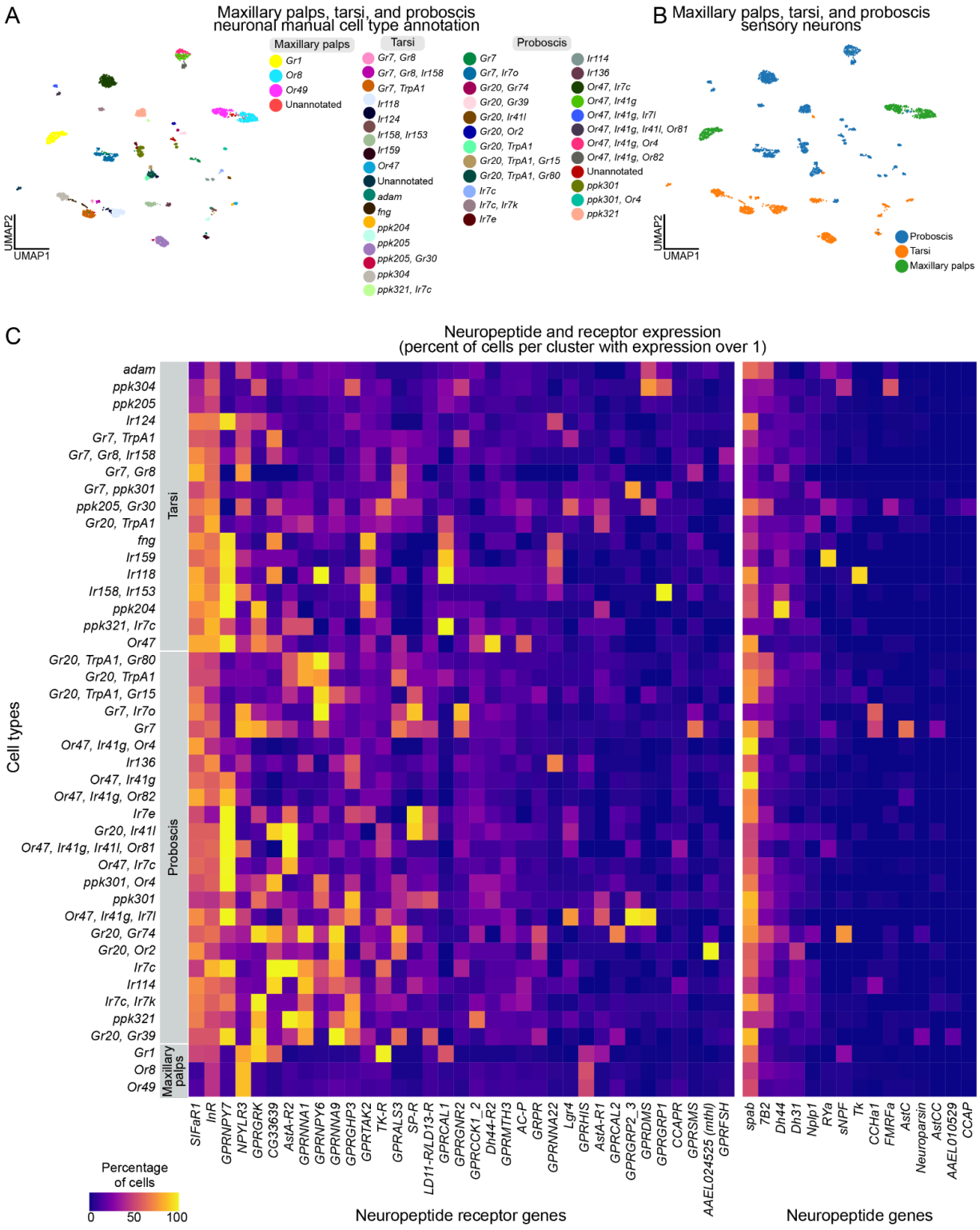
A
Maxillary palps, tarsi, and proboscis neuronal manual cell type annotation
Maxillary palps
Gr1
Or8
Or49
Unannotated
Tarsi
Gr7, Gr8
Gr7, Gr8, Ir158
Gr7, TrpA1
Ir118
Ir124
Ir158, Ir153
Ir159
Or47
Unannotated
adam
fng
ppk204
ppk205
ppk205, Gr30
ppk304
ppk321, Ir7c
Proboscis
Gr7
Gr7, Ir7o
Gr20, Gr74
Gr20, Gr39
Gr20, Ir41l
Gr20, Or2
Gr20, TrpA1
Gr20, TrpA1, Gr15
Gr20, TrpA1, Gr80
Ir7c
Ir7c, Ir7k
Ir7e
Ir114
Ir136
Or47, Ir7c
Or47, Ir41g
Or47, Ir41g, Ir7l
Or47, Ir41g, Ir41l, Or81
Or47, Ir41g, Or4
Or47, Ir41g, Or82
Unannotated
ppk301
ppk301, Or4
ppk321
UMAP2
UMAP1
B Maxillary palps, tarsi, and proboscis sensory neurons
UMAP2
UMAP1
Proboscis
Tarsi
Maxillary palps
C
Neuropeptide and receptor expression
(percent of cells per cluster with expression over 1)
Cell types
Tarsi
Proboscis
Maxillary palps
adam
ppk304
ppk205
Ir124
Gr7, TrpA1
Gr7, Gr8, Ir158
Gr7, Gr8
Gr7, ppk301
ppk205, Gr30
Gr20, TrpA1
fng
Ir159
Ir118
Ir158, Ir153
ppk204
ppk321, Ir7c
Or47
Gr20, TrpA1, Gr80
Gr20, TrpA1
Gr20, TrpA1, Gr15
Gr7, Ir7o
Gr7
Or47, Ir41g, Or4
Ir136
Or47, Ir41g
Or47, Ir41g, Or82
Ir7e
Gr20, Ir41l
Or47, Ir41g, Ir41l, Or81
Or47, Ir7c
ppk301, Or4
ppk301
Or47, Ir41g, Ir7l
Gr20, Gr74
Gr20, Or2
Ir7c
Ir114
Ir7c, Ir7k
ppk321
Gr20, Gr39
Gr1
Or8
Or49
SIFaR1
InR
GPRNPY7
NPYLR3
GPRGRK
CG33639
AstA-R2
GPRNNA1
GPRNPY6
GPRNNA9
GPRGHP3
GPRTAK2
TK-R
GPRALS3
SP-R
LD11-R/LD13-R
GPRCAL1
GPRGNR2
GPRCCK1_2
Dh44-R2
GPRMTH3
AC-P
GRPR
GPRNNA22
Lgr4
GPRHIS
AstA-R1
GPRCAL2
GPRGRP2_3
GPRDMS
GPRGRP1
CCAPR
GPRSMS
AAEL024525 (mthl)
GPRFSH
spab
7B2
Dh44
Dh31
Nplp1
RYa
sNPF
Tk
CCHa1
FMRFa
AstC
Neuroparsin
AstCC
AAEL010529
CCAP
Percentage of cells
0
50
100
Neuropeptide receptor genes
Neuropeptide genes

Figure S25. Neuropeptide receptor and synthesis gene analysis, related to Figures 5 and 6.

(A-B) UMAP of combined *nompC*-negative sensory neurons from maxillary palps, tarsi and proboscis samples, colored by manual cell type annotation as listed in legend at the right of the figure panel **(A)** and original tissue **(B)**.

(C) Heatmap of expression of neuropeptide receptor genes (left) and neuropeptide synthesis genes (right) within manually annotated *nompC*-negative sensory neurons in the maxillary palps, tarsi and proboscis. Color scale indicates percentage of cells expressing a gene above threshold (normalized expression value of 1). Sensory genes are indicated in columns and cell types indicated in rows. Genes were included if they were expressed above threshold in over 20% of cells in at least one cell type. Genes filtered from lists in Table S4. Normalized expression is ln([(raw count/total cell counts)x median total counts across cells]+1).

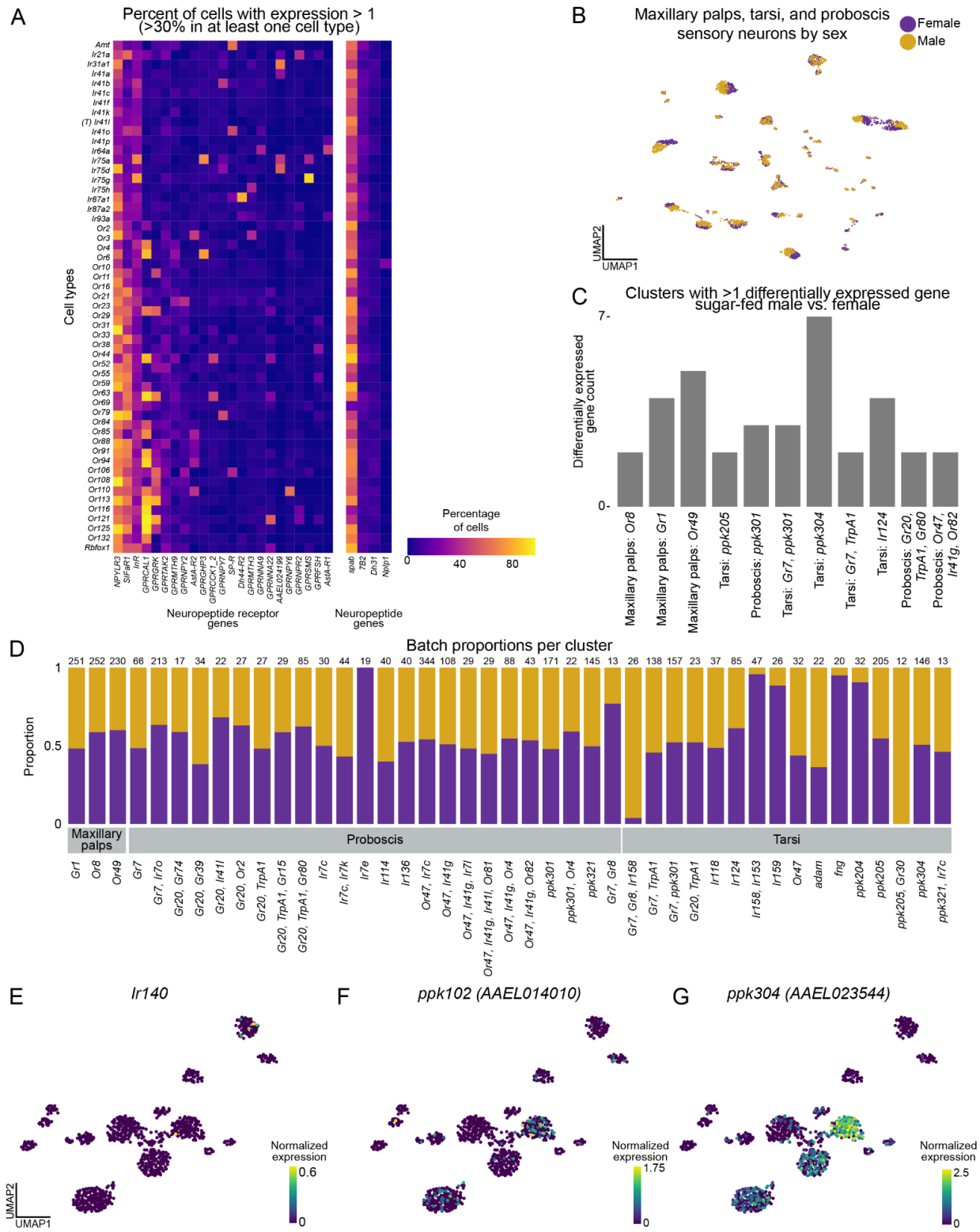
A
Percent of cells with expression > 1
(>30% in at least one cell type)
Cell types
Neuropeptide receptor genes
Neuropeptide genes
Percentage of cells
0
40
80
B
Maxillary palps, tarsi, and proboscis sensory neurons by sex
Female
Male
UMAP2
UMAP1
C
Clusters with >1 differentially expressed gene
sugar-fed male vs. female
Differentially expressed gene count
7
0
Maxillary palps: Or8
Maxillary palps: Gr1
Maxillary palps: Or49
Tarsi: ppk205
Proboscis: ppk301
Tarsi: Gr7, ppk301
Tarsi: ppk304
Tarsi: Gr7, TrpA1
Tarsi: Ir124
Proboscis: Gr20, TrpA1, Gr80
Proboscis: Or47, Ir41g, Or82
D
Batch proportions per cluster
Proportion
1
0.5
0
Maxillary palps
Proboscis
Tarsi
E
Ir140
Normalized expression
0.6
0
F
ppk102 (AAEL014010)
Normalized expression
1.75
0
G
ppk304 (AAEL023544)
Normalized expression
2.5
0

Figure S26. Neuropeptide receptor and synthesis gene analysis, related to Figures 5 and 6.

(A) Heatmap of expression of neuropeptide receptor genes (left) and neuropeptide synthesis genes (right) within manually annotated olfactory sensory neurons (*nompC*-negative) in the antenna. Color scale indicates percentage of cells expressing a gene above threshold (normalized expression value of 1). Sensory genes are indicated in columns and cell types indicated in rows. Genes were included if they were expressed above threshold in over 20% of cells in at least one cell type. Genes filtered from lists in Table S2. Normalized expression is ln([(raw count/total cell counts)x median total counts across cells]+1).

(B) UMAP of combined *nompC*-negative sensory neurons from maxillary palps, tarsi and proboscis samples, colored by sex.

(C) Bar plot of number of differentially expressed genes (DEGs) between females and males in each olfactory sensory neuron cell type. Clusters shown contain at least 1 DEG with a |log fold change| > 1 and false discovery rate < 0.05 (determined by MAST on normalized expression). For more information on DEGs, see Table S6.

(D) Proportion plot for annotated *nompC*-negative sensory neurons from maxillary palps, tarsi and proboscis. Bar plot of proportion cells from each sex that makes up each cell type. Numbers above each bar indicate the number of cells in that cluster. Cell types that are more than 70% from a single sex indicated in red.

(E-G) In tarsi *nompC*-negative sensory neurons, UMAP of normalized gene expression of *Ir140* (E), *ppk102 (AAEL014010)* (F), and *ppk304 (AAEL023544)* (G). Each end of color bar trimmed 0.1% for visibility.

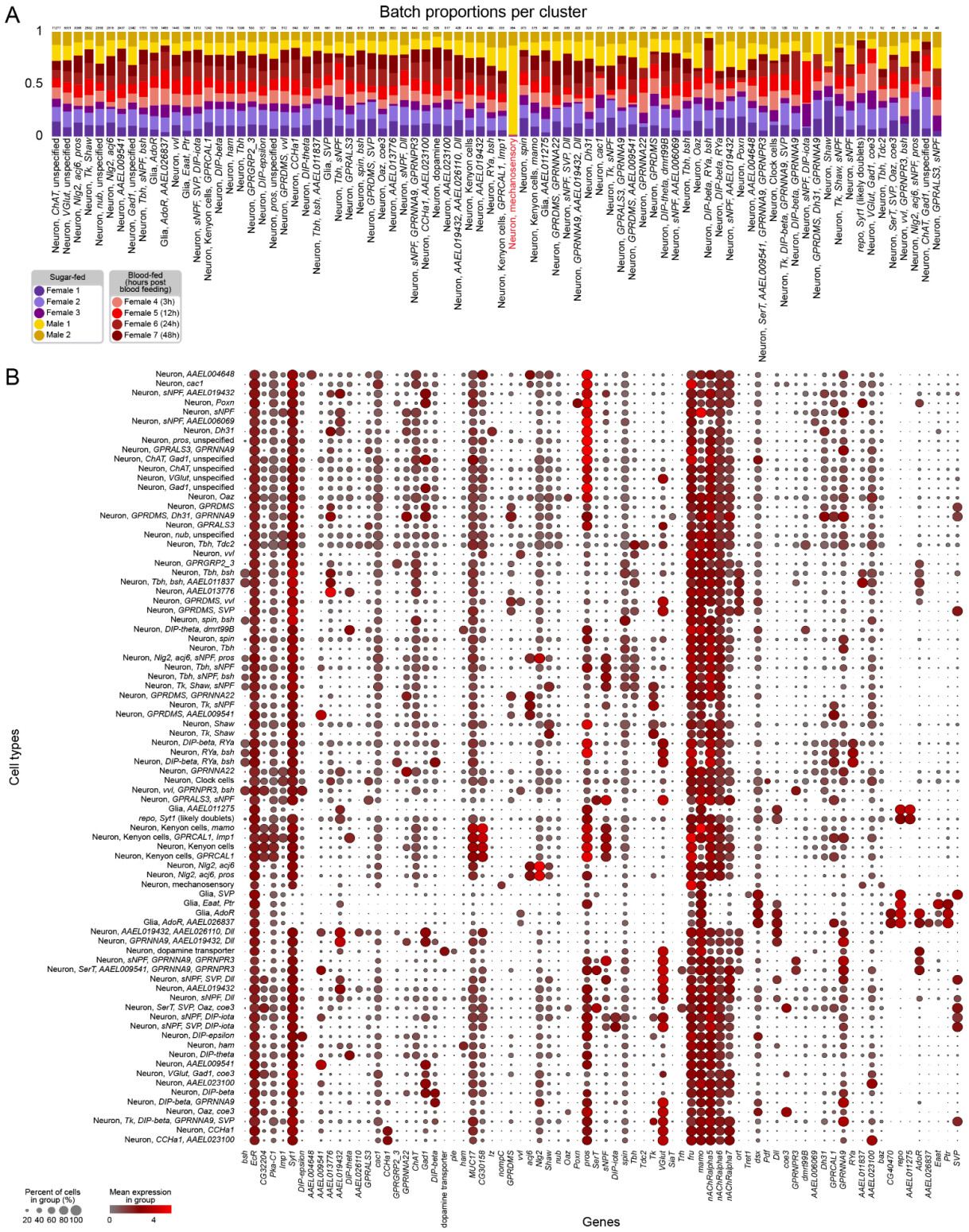
A
Batch proportions per cluster
1
0.5
0
Sugar-fed
Female 1
Female 2
Female 3
Male 1
Male 2
Blood-fed (hours post blood feeding)
Female 4 (3h)
Female 5 (12h)
Female 6 (24h)
Female 7 (48h)
B
Cell types
Genes
Percent of cells in group (%)
20 40 60 80 100
Mean expression in group
0
4

Figure S27. Brain Cell types, related to Figures 7 and 8.
(A) Proportion plot for annotated brain nuclei. Bar plot of proportion that each sample makes up each cell type. Numbers above each bar indicate the number of cells in that cluster. Cell types that are more than 70% from a single sample indicated in red.
(B) Dotplot of brain nuclei annotations and gene markers. Color scale indicates mean normalized expression of gene within cell type, size of dot indicates percent of cells expressing gene within the group. See Table S3 and Table S4 for gene IDs and thresholds.

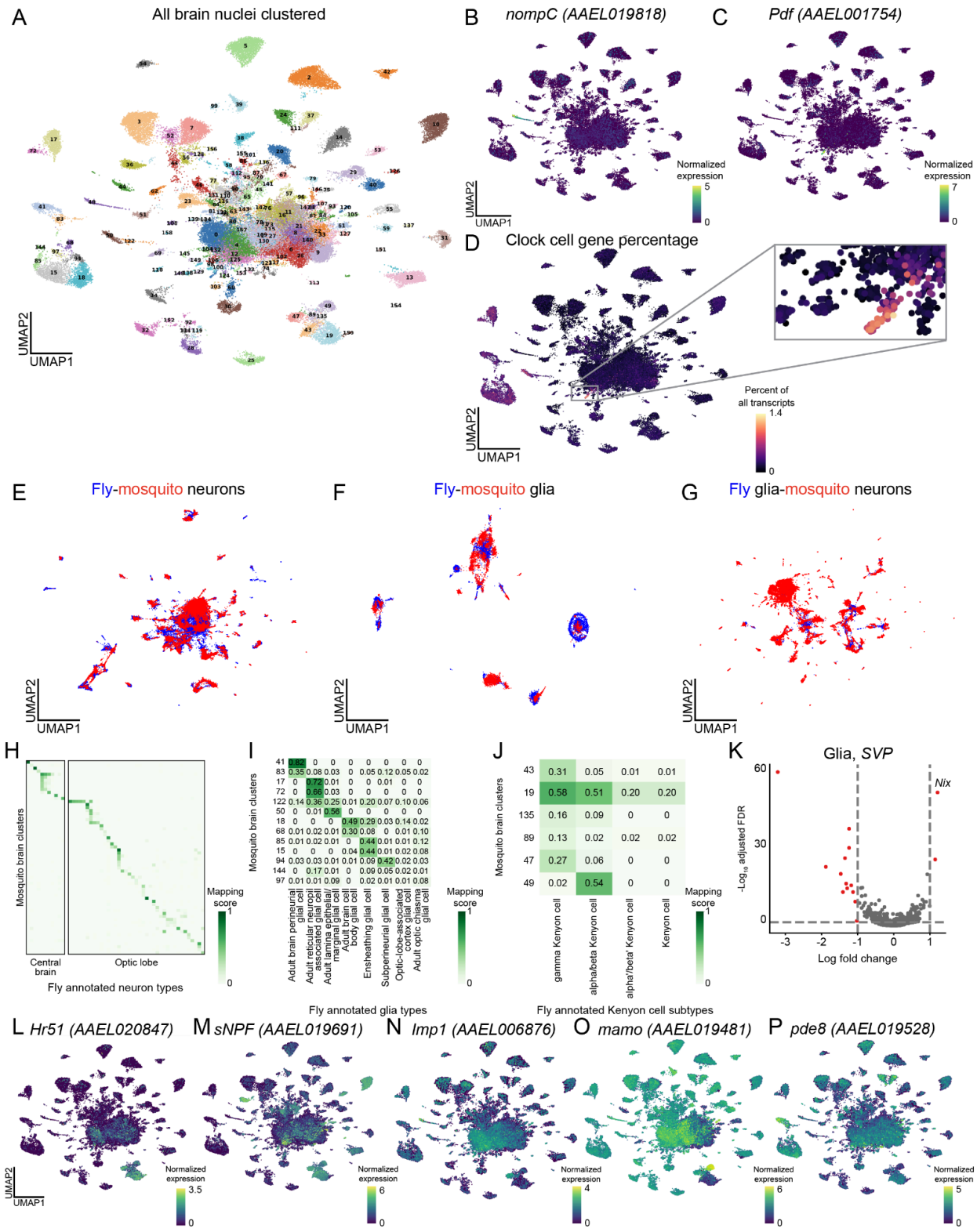
A
All brain nuclei clustered
UMAP2
UMAP1
B
nompC (AAEL019818)
Normalized expression
5
0
C
Pdf (AAEL001754)
Normalized expression
7
0
D
Clock cell gene percentage
Percent of all transcripts
1.4
0
E
Fly-mosquito neurons
F
Fly-mosquito glia
G
Fly glia-mosquito neurons
H
Mosquito brain clusters
Central brain
Optic lobe
Fly annotated neuron types
Mapping score
I
Mosquito brain clusters
Adult brain perineurial glial cell
Adult reticular neuropil associated glial cell
Adult lamina epithelial/ marginal glial cell
Adult brain cell body glial cell
Ensheathing glial cell
Subperineurial glial cell
Optic-lobe-associated cortex glial cell
Adult optic chiasm glial cell
Fly annotated glia types
J
Mosquito brain clusters
gamma Kenyon cell
alpha/beta Kenyon cell
alpha'/beta' Kenyon cell
Kenyon cell
Fly annotated Kenyon cell subtypes
K
Glia, SVP
Nix
-Log10 adjusted FDR
Log fold change
L Hr51 (AAEL020847)
M sNPF (AAEL019691)
N Imp1 (AAEL006876)
O mamo (AAEL019481)
P pde8 (AAEL019528)
Normalized expression
3.5
6
4
6
5

Figure S28. SAMap analysis and identification of clock cells and kenyon cells, related to Figure 7.

(A) UMAP of brain nuclei clustered using the Leiden algorithm (resolution = 5).

(B-C) Normalized gene expression UMAP of *nompC (AAEL019818)* (B) and *Pdf (AAEL001754)* (C) in all brain nuclei. Normalized expression is ln([(raw count/total cell counts)x median total counts across cells]+1).

(D) Normalized expression UMAP of gene set of 10 putative clock cell gene markers (Table S4). Expression of gene set shown as a fraction of total transcripts in each cell. Cluster with high expression highlighted in grey box, enlarged in inset.

(E-G) UMAP of manifold integration of snRNA-seq data from *Aedes aegypti* mosquito brain with published *Drosophila melanogaster* fly head[24]. Plots show integration of fly neurons with mosquito neurons (E), fly glia with mosquito glia (F), and as a control, fly glia with mosquito neuron (G). Alignment scores are 0.64, 0.64 and 0.47, respectively.

(H-J) Correlation matrices of mapping scores between *Drosophila melanogaster* head annotations and *Aedes aegypti* of clusters (Leiden, resolution = 5) for neuronal cell types **(H)**, glial cell types (I), and Kenyon cell subtypes (J). Calculated by SAMap. For numerical values, see Tables S8-S9.

(K) Volcano plot of differentially expressed genes in female and male cells in the "*SVP*" glia cluster. All significant genes (indicated in red) a |log fold change| > 1 and false discovery rate < 0.05, determined by MAST on normalized expression. Male biased genes on right, as indicated by *Nix* (*AAEL022912*).

(L-P) Normalized gene expression UMAP of *Hr51 (AAEL020847)* (L), *sNPF (AAEL019691)* (M), *Imp1 (AAEL006876)* (N), *mamo (AAEL019481)* (O)*, Pde8 (AAEL019528)* (P) in all brain nuclei.

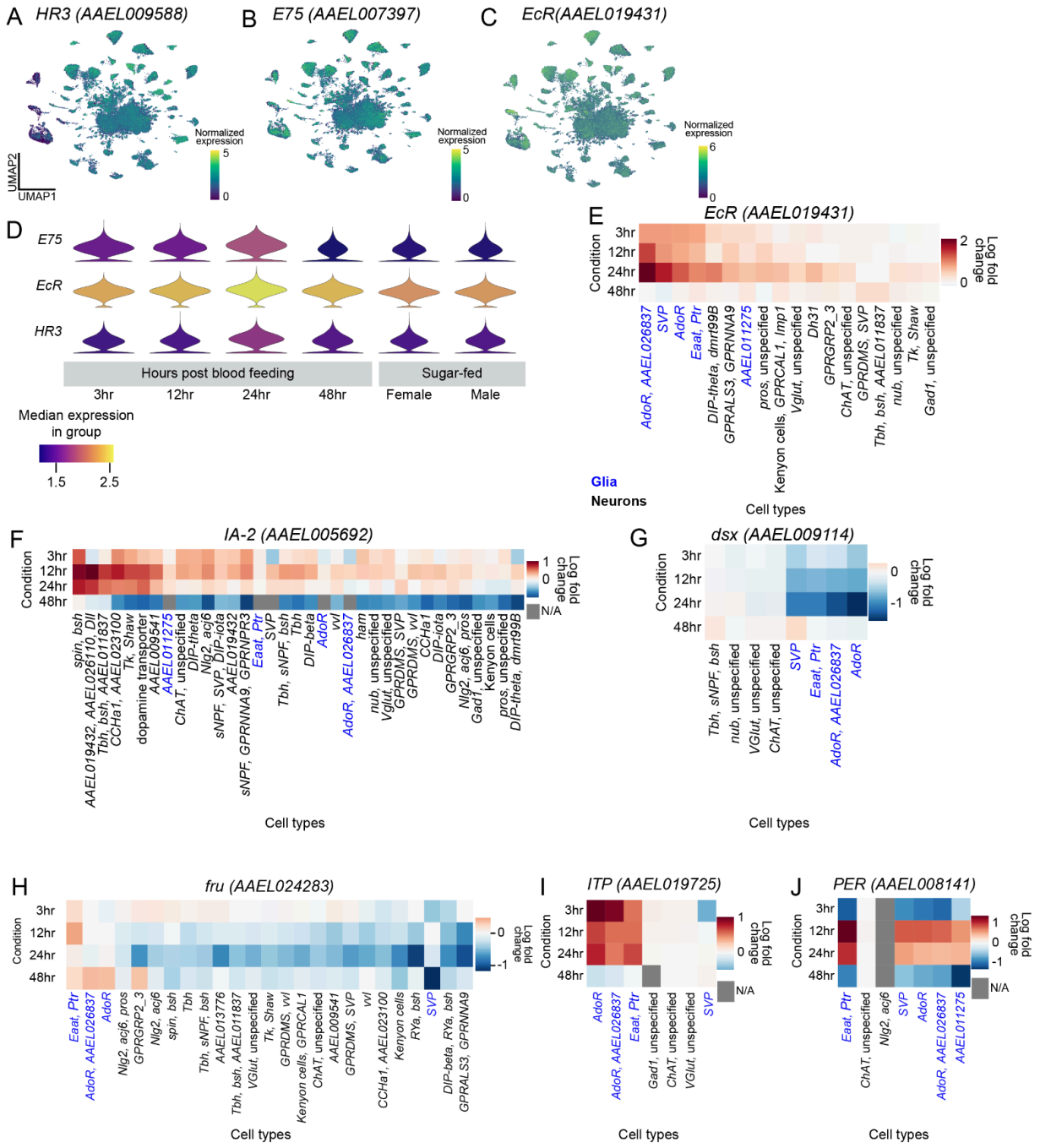
A HR3 (AAEL009588)
B E75 (AAEL007397)
C EcR(AAEL019431)
Normalized expression
UMAP2
UMAP1
D
E75
EcR
HR3
Hours post blood feeding
Sugar-fed
3hr
12hr
24hr
48hr
Female
Male
Median expression in group
1.5
2.5
E EcR (AAEL019431)
Condition
Log fold change
Glia
Neurons
Cell types
F IA-2 (AAEL005692)
N/A
G dsx (AAEL009114)
H fru (AAEL024283)
I ITP (AAEL019725)
J PER (AAEL008141)

Figure S29. Blood feeding changes in brain, related to Figure 8.
(A-C) Normalized gene expression UMAP of *E75* (*AAEL007397*) (A), *EcR* (*AAEL019431*) (B) and *HR3* (*AAEL009588*) (C) in all brain nuclei. Normalized expression is ln([(raw count/total cell counts)x median total counts across cells]+1).
(D) Violin plot of gene expression of *E75*, *EcR* and *HR3* across all brain nuclei in each timepoint.
(E-J) Heatmaps of log fold change genes across blood feeding conditions compared to sugar-fed female brain by cell type. Genes shown: *EcR (AAEL019431)* (E), *IA-2 (AAEL005692)* (F), *dsx* (*AAEL009114*) (G), *fru* (*AAEL024283*) (H), *ITP* (*AAEL019725*) (I), and *PER* (*AAEL008141*) (J). Log fold change is determined by MAST on normalized expression. Cell types are sorted by the total log fold change across all timepoints and colored as glia (blue) or neurons (black). Cell types included have over 10 cells in each timepoint, and at least one timepoint where change from sugar-fed condition had a false discovery rate < 0.05. Grey boxes indicate log fold change data is not available, due to zero expression within cell type in either sugar-fed or blood-fed condition. Normalized expression is ln([(raw count/total cell counts)x median total counts across cells]+1).

Supplemental table legends

Table S1. Dissection and sample processing information by sample.
Sample information including number of mosquitoes dissected, FASTQ prefixes, number of cells, number and percent of cells filtered, whether FACS was used, sample processing parameters, Cell Ranger statistics, CellBender parameters, quality control filtering thresholds and percent of cells removed, final cell count, and additional notes.

Table S2. Processed data objects on UCSC Cell Browser and Zenodo Supplemental Data.
Information on processed data files for each tissue and filtered sensory neuron population. Includes number of samples per tissue, number of cells, annotation and visualization parameters, clustering resolution and algorithm used for cell type annotations were assigned, and filtering parameters for sensory neuron data objects (if applicable).

Table S3. Gene identifiers, symbols, descriptions and *Drosophila melanogaster* orthology.
Look up table of all genes used in this manuscript. Includes gene symbol used within this manuscript, and corresponding VectorBase gene ID (AAEL)[58], NCBI gene symbol (LOC)[223], descriptions, references, and *Drosophila melanogaster* homology information from BioMart (Ensembl Genomes release 56[56]).

Table S4. Annotation thresholds and gene lists.
Gene lists for salivary gland secreted proteins, antimicrobial peptides, Kenyon Cell markers, clock cell markers, sensory proteins, neuropeptides and neuropeptide receptors. Also includes genes used to annotate all cell types of each tissue, including

gene thresholds.

Table S5. Thresholded differentially expressed genes for antenna olfactory sensory neurons, between male and female cells across each cell type, related to Figure S19.
Differentially expressed genes between females and males for each antenna olfactory sensory neuron cell type. Filtered for genes with |log fold change| > 1 and false discovery rate < 0.05 (determined by MAST on normalized expression).

Table S6. Thresholded differentially expressed genes for *nompC*-negative sensory neurons in maxillary palps, proboscis, and tarsi, between male and female cells across each cell type, related to Figure S26.
Differentially expressed genes between females and males for each *nompC*-negative sensory neuron cell type in maxillary palps, proboscis, and tarsi. Filtered for genes with |log fold change| > 1 and false discovery rate < 0.05 (determined by MAST on normalized expression).

Table S7. Manifold integration mapping scores of neurons from *Aedes aegypti* brain and *Drosophila melanogaster* head, related to Figure S28.
Correlation matrices of mapping scores between neurons using annotated *Drosophila melanogaster* head cell types and *Aedes aegypti* brain clusters (Leiden, resolution = 5). Includes corresponding annotations from this paper.

Table S8. Manifold integration mapping scores of glia from *Aedes aegypti* brain and *Drosophila melanogaster* head, related to Figure S28.
Correlation matrices of mapping scores between glia using annotated *Drosophila melanogaster* head cell types and *Aedes aegypti* brain clusters (Leiden, resolution = 5). Includes corresponding annotations from this paper.

Table S9. Thresholded differentially expressed genes for annotated brain cell types, between male and female cells across each cell type, related to Figure 7.
Differentially expressed genes between females and males for each annotated brain cell type. Filtered for genes with |log fold change| > 1 and false discovery rate < 0.05 (determined by MAST on normalized expression).

Table S10. Thresholded differentially expressed genes for annotated brain cell types, between post-blood-feeding timepoints compared to sugar-fed female cells across each cell type, related to Figure 8.
Differentially expressed genes between each post-blood-feeding timepoint compared to sugar-fed female cells for each annotated brain cell type. Filtered for genes with |log fold change| > 1 and false discovery rate < 0.05 (determined by MAST on normalized expression).

Table S11. RNA *in situ* hybridization probe information.
Table includes targeted gene names, HCR Amplifier, probe sequences and probe lot numbers for ordering.

Table S12. Dissection tube Information.
Dissection information associated with *Aedes aegypti* Mosquito Cell Atlas sample numbers (Table S1). Information includes dissection tube ID, tissue dissector, lab of dissector, tissue, tissue sex, date and time of dissection, animal hatch date, number of animals used, volume of Schneider's Medium used, and if RNase Inhibitor was added.

Table S13. Thresholded differentially expressed genes for annotated abdominal pelt fat tissue and gut enterocyte cell types, between male and female cells across each cell type, related to Figure S16.
Differentially expressed genes between females and males for each annotated abdominal pelt fat tissue and gut enterocyte cell types. Filtered for genes with |log fold change| > 1 and false discovery rate < 0.05 (determined by MAST on normalized expression).